1986

A method for determining material damping from driving point measurements

Jonathan Dean Rogers
Iowa State University

INFORMATION TO USERS

This reproduction was made from a copy of a manuscript sent to us for publication and microfilming. While the most advanced technology has been used to photograph and reproduce this manuscript, the quality of the reproduction is heavily dependent upon the quality of the material submitted. Pages in any manuscript may have indistinct print. In all cases the best available copy has been filmed.

The following explanation of techniques is provided to help clarify notations which may appear on this reproduction.

1. Manuscripts may not always be complete. When it is not possible to obtain missing pages, a note appears to indicate this.

2. When copyrighted materials are removed from the manuscript, a note appears to indicate this.

3. Oversize materials (maps, drawings, and charts) are photographed by sectioning the original, beginning at the upper left hand corner and continuing from left to right in equal sections with small overlaps. Each oversize page is also filmed as one exposure and is available, for an additional charge, as a standard 35mm slide or in black and white paper format.*

4. Most photographs reproduce acceptably on positive microfilm or microfiche but lack clarity on xerographic copies made from the microfilm. For an additional charge, all photographs are available in black and white standard 35mm slide format.*

***For more information about black and white slides or enlarged paper reproductions, please contact the Dissertations Customer Services Department.**

U·M·I Dissertation Information Service

University Microfilms International
A Bell & Howell Information Company
300 N. Zeeb Road, Ann Arbor, Michigan 48106

Rogers, Jonathan Dean

A METHOD FOR DETERMINING MATERIAL DAMPING FROM DRIVING POINT MEASUREMENTS

Iowa State University PH.D. 1986

A method for determining material damping from driving point measurements

by

Jonathan Dean Rogers

A Dissertation Submitted to the
Graduate Faculty in Partial Fulfillment of the
Requirements for the Degree of
DOCTOR OF PHILOSOPHY

Department: Engineering Science and Mechanics
Major: Engineering Mechanics

Approved:

Members of the Committee:

Signature was redacted for privacy.
In charge of Major Work

Signature was redacted for privacy.
For the Major Department

Signature was redacted for privacy.

Signature was redacted for privacy.
For the Graduate College

Iowa State University
Ames, Iowa

1986

TABLE OF CONTENTS

CHAPTER I. INTRODUCTION

Material damping characteristics are important to physicists, metallurgists, and engineers. The physicists and metallurgists are primarily interested because of the insight into microstructural material characteristics that material damping provides. Engineers, however, are most interested in the effect damping has on the vibration response of structures.

In any vibrating structure, many forms of damping or energy loss may be occurring. Typically, the vibrational energy may be lost to friction in joints and connections, to drag or sound radiation losses to the surrounding fluid, and to material damping. In many cases the damping within the material is insignificant when compared to the other damping occurring in the system. However, for welded structures or for space structures where there is no surrounding fluid, the contribution of material damping to the system damping may be quite significant. In other cases materials with very high damping have been developed for application to existing structures for vibration control. These examples reveal the importance of material damping and justify the study of material damping characteristics.

Many material damping mechanisms have been identified as noted by Crandall [1], Bert [2], and Rogers [3]. A variety of

testing methods have been developed to measure the damping associated with these mechanisms. The testing methods attempt to isolate the material damping from any outside damping sources which may be present in the system. Ideally, then, the test results accurately describe the material damping occurring within the specimen.

The current work presents a method for determining material damping from beam specimens. Each beam specimen is driven at its midpoint with an electrodynamic vibration exciter. The driving force and driving point acceleration are measured and are related to the damping in terms of the energy loss factor of the material. Using the new method, the loss factor was obtained for 2024-T351 aluminum and Model-Tech FR-20 (Measurements Group, Inc.), an aluminum particle filled epoxy.

Two approaches to the data acquisition were performed during the testing. The first approach was a "quick and dirty" method in which the driving force and driving point acceleration signals were measured with true RMS voltmeters. This method gave quick results; however, the signals contained significant frequency components which were not related to material damping so additional signal analysis was required to extract the material damping contribution.

The second approach was a more rigorous method in which frequency analysis of the signals was performed. The contribution of each frequency component was then available for investigation. Thus, the contribution of material damping to

the response signal could be better isolated from other phenomena.

For tests run using the frequency analysis method, the beams were tested in ambient air and at reduced pressure. Thus, the effect of air pressure on thin vibrating beams was observed.

The material loss factor for the aluminum, as determined using the new test method, was compared to previously obtained values from another test method as well as the values predicted by the Zener Thermal Relaxation Theory. The Zener Theory is known to be quite accurate in predicting the damping of aluminum, and this theoretical basis is the primary reason that aluminum was chosen for testing. Aluminum also has very low damping and, therefore, acts as a good check on the sensitivity of the test method by establishing its lower threshold of measurement.

The Model-Tech has much higher damping than aluminum. It was chosen because it was available and provided the wide difference in damping compared to aluminum. In addition, results from previous tests on Model-Tech were available for comparison.

CHAPTER II. MATERIAL DAMPING

Significance of Damping

In all vibrating systems some energy loss is inherent. This energy loss is generally referred to as damping. The sources of vibration damping may be internal to the vibrating system, such as material damping, or may be external to the vibrating system, such as air damping. In either case, the damping is a measure of the energy lost from the vibrating system. A convenient measure of damping is the loss factor, which is proportional to the ratio of the energy lost per cycle to the maximum potential energy stored in the system during that cycle. The loss factor, η, is thus defined by

$$\eta = \frac{D}{2\pi U} \tag{1}$$

where

D = the energy lost per cycle,

U = the maximum potential energy stored per cycle.

The loss factor is the measure of damping which will be used in this work; however, there are several other measures of damping which are often found in the literature. These measures are related by rather simple expressions provided that the damping is fairly small; i.e., the loss factor is less than about 0.3. Since for most vibrating systems the damping is less than this value, the simple relationships given in Table 1 are generally true.

Table 1. Relationships between the various measures of damping

	η	Q	ζ	δ
Loss factor, η =	η	$\frac{1}{Q}$	2ζ	$\frac{\delta}{\pi}$
Quality factor, Q =	$\frac{1}{\eta}$	Q	$\frac{1}{2\zeta}$	$\frac{\pi}{\delta}$
Damping ratio, ζ =	$\frac{\eta}{2}$	$\frac{1}{2Q}$	ζ	$\frac{\delta}{2\pi}$
Logarithmic decrement, δ =	$\pi\eta$	$\frac{\pi}{Q}$	$2\pi\zeta$	δ

Damping indicates its presence in two ways: reduction in the resonant frequency and control of the resonant amplitude. The effect of damping on the resonant frequency of the single-degree-of-freedom (SDOF) oscillator shown in Fig. 1 is given by Thomson [4] as

$$\omega_d = \omega_n\sqrt{1 - (\eta/2)^2} \qquad (2)$$

where

ω_d = the damped natural frequency,

ω_n = the undamped natural frequency,

η = the loss factor.

The effect of damping on the resonant amplitude of the SDOF oscillator is shown in Fig. 2. It is clear that the resonant response amplitude is very strongly dependent on the damping.

The magnification factor plotted in Fig. 2 is given by Thomson [4] as

$$\frac{x}{F/k} = \frac{1}{\sqrt{[1 - (\omega/\omega_n)^2]^2 + [\eta(\omega/\omega_n)]^2}} \qquad (3)$$

Thus, from Eqs. (2) and (3) and Fig. 2 it is clear that the effect of damping on a SDOF oscillator is most evident in the magnitude of the resonant response.

Since damping plays such an important role in the resonant response of a vibrating system, it must be included in the dynamic analysis of a structure. It is often desirable to incorporate damping into the stress-strain constitutive relationship for a material. The damping is then treated as a material property and arises naturally in the equations of motion of a structure. One well known method for including damping is the complex modulus approach. In this method the static modulus of elasticity, or storage modulus, is replaced by

$$E^* = E(1 + j\eta) \qquad (4)$$

where

E^* = the complex modulus of elasticity,

E = the storage modulus,

$j = \sqrt{-1}$.

In recent years a great deal of effort has been expended attempting to develop more accurate material constitutive

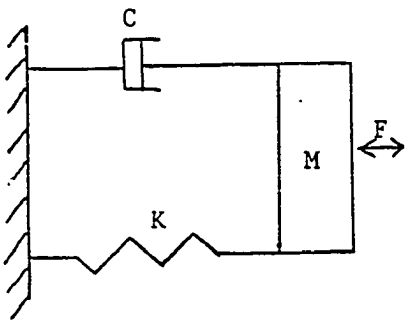

Fig. 1. Single degree of freedom oscillator

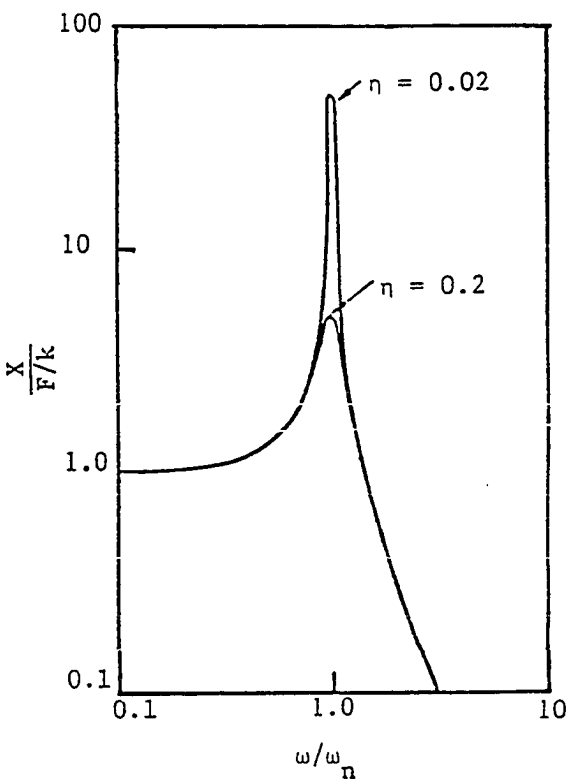

Fig. 2. Effect of loss factor on the response of a single degree of freedom model

relationships. Significant work has been done by Rogers [5,6], Bagley and Torvik [7,8], Koeller [9], and Jones [10] on constitutive laws relating stress to fractional time derivatives of strain. It has been shown [8] that fractional order derivatives arise naturally in real physical systems; e.g., certain motion of a Newtonian fluid. Thus, the appearance of fractional order derivatives in the behavior of real systems is not without precedent. The main allure of the fractional calculus model lies in the small number of parameters required to obtain good agreement between the theory and the frequency-dependent physical response of the structure. Bagley and Torvik [8] showed that good results could be obtained for the frequency response of a structure with a three-parameter model where one of the parameters was the order of the derivative. Thus, although the fractional calculus modeling of materials appears to be somewhat esoteric, it seems to provide a good model of the frequency dependence of the elastic and damping properties of certain materials.

In this work the complex modulus approach was used. It has been shown by Rogers [5] that the complex modulus approach is completely compatible with the fractional calculus constitutive model so long as no frequency-dependent restrictions are placed on the storage modulus, E, or the loss factor, η. The derivations used in the current work place no such restrictions on the loss factor; however, the storage modulus is assumed to be constant with frequency. Therefore, the

current results are not entirely general but are acceptable to the level of the constant storage modulus assumption.

Damping Mechanisms

The study of material damping mechanisms has a long history as noted by Lazan [11]. The first recorded efforts were those by Coulomb in his Memoir on Torsion in 1784. Since that time, a great many investigators have presented work on material damping mechanisms. Several mechanisms have been proposed to describe material damping. These mechanisms are generally broken into two general groups: linear and non-linear.

Linear materials exhibit damping characteristics which may be modeled by classical linear components. Therefore, in examining linear material damping, it is useful to begin by considering classical linear damping. The classical damping component is the linear dashpot. The linear dashpot exerts a force, $F_D = cv$, in opposition to the relative velocity, v, across the dashpot. The constant, c, is called the dashpot parameter. The presence of a force proportional to, but in opposite direction to, the velocity has led to the term "viscous damping" being attached to this type of model. Thus, linear material damping is sometimes referred to as internal viscous damping. The simplest material model with this type of damping is the Kelvin-Voigt model shown in Fig. 3 which predicts that the material will behave like a spring and a

dashpot in parallel. Although this model has been proven to be unsatisfactory for most materials, it is useful to examine this model closely since it is the easiest to use mathematically.

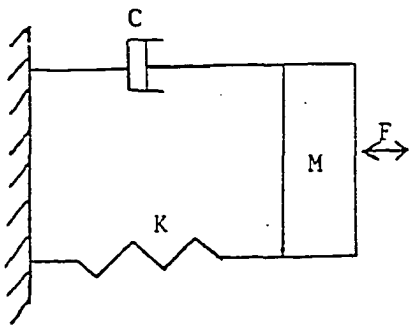

Fig. 3. Single degree of freedom model--Kelvin-Voigt solid

For the case shown in Fig. 3, the energy dissipated per cycle, D, for harmonic motion $x = X_o \cos(\omega t + \phi)$, is given by

$$D = \oint c\dot{x}dx = \int_o^{2\pi/\omega} c\dot{x}^2 dt = \pi c \omega X_o^2 \qquad (5)$$

where the dots indicate time derivatives.

The maximum potential energy stored in the system during a cycle, U, is given by

$$U = \frac{1}{2} k X_o^2 \ . \qquad (6)$$

The loss factor, η, for the Kelvin-Voigt model is given from Eq. (1) as

$$\eta = \frac{D}{2\pi U} = \frac{c\omega}{k} . \qquad (7)$$

It is of interest to note that the loss factor for the Kelvin-Voigt model, as given in Eq. (7), is a linear function of frequency and is independent of the amplitude of vibration. This type of behavior is typical of linear material models; i.e., the loss factor is dependent on frequency but independent of amplitude.

The Kelvin-Voigt model is quite useful as a step in understanding the behavior of a material. As is noted by Lazan [11], a great deal of work has been done on more elaborate models for material behavior; however, the more elaborate models usually contain Kelvin-Voigt units.

Several linear damping mechanisms are discussed by Zener [12] and are considered in the model of a "standard linear solid." This improved linear model has been shown to be quite accurate for many metals at fairly low stress levels [11]. The stress-strain constitutive law for this material model is given by

$$\sigma + \tau_\varepsilon \dot{\sigma} = E(\varepsilon + \tau_\sigma \dot{\varepsilon}) \qquad (8)$$

where

σ = normal stress,

E = elastic modulus,

ε = normal strain,

τ_ε = relaxation time for stress under constant strain,

τ_σ = relaxation time for strain under constant stress,

Dots indicate time derivatives.

The model for the standard linear solid is shown in Fig. 4. This model is seen to be a Kelvin-Voigt unit with an added spring in series with the dashpot.

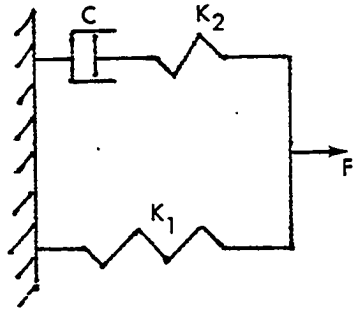

Fig. 4. Standard linear solid model

The standard linear solid described by Eq. (8) assumes that all energy lost within the material is associated with various relaxation mechanisms. There are many such relaxation mechanisms, with each mechanism being dominant at certain frequencies and/or temperatures as indicated by Zener [12], Lazan

[11], and Lee [13]. As is pointed out by Baker, Woolam, and Young [14] and by Gibson and Plunkett [15], of the linear damping mechanisms, only the transverse thermal current mechanism is likely to be significant at frequencies of interest. The transverse thermal current theory, commonly referred to as the Zener Thermal Relaxation Theory, assumes that the energy lost in each cycle is dissipated as heat. To illustrate this concept, the case of a thin flat beam undergoing transverse vibration may be considered. The fibers on one side of the beam are stretched and, therefore, tend to cool. The fibers on the other side are compressed and, therefore, tend to heat. This process gives a temperature gradient across the beam so some heat flow occurs. Associated with the heat flow is a loss of energy, which is the damping.

Following from Zener [12] and Crandall [16], the loss factor for a thin flat beam undergoing simple harmonic bending is given as

$$\eta = \frac{\alpha^2 E T}{c} \frac{\omega\tau}{(1 + \omega^2\tau^2)} \tag{9}$$

where

α = coefficient of linear thermal expansion,

E = modulus of elasticity,

T = absolute temperature,

c = specific heat per unit volume,

ω = angular frequency of simple harmonic motion,

τ = relaxation time for temperature equalization across the beam by transverse thermal currents.

The relaxation time, τ, is given by

$$\tau = \frac{t^2 c}{\pi^2 k} \tag{10}$$

where

t = beam thickness,

k = thermal conductivity.

It is important to note that two characteristics of the damping mechanism are described by Eq. (9). First, the loss factor is dependent on the frequency of vibration. The loss factor is a maximum at $\omega = 1/\tau$ and falls off gradually to zero as frequency increases or decreases. Second, the loss factor is independent of amplitude of beam vibration and, therefore, independent of mode shape. This result, though not obvious on first inspection, can be deduced from Zener's derivation as follows.

The motion of each point in the beam is assumed to be harmonic. Therefore, at each point the stresses, strains, and temperature may be written as an amplitude multiplied by a sine or cosine term. These sinusoidal functions are then substituted into the governing stress-strain and heat transfer equations for a linear material. Zener then shows that by integrating these governing equations over the volume of the beam and taking a time average, the amplitude terms fall out.

Thus, the damping is independent of the amplitude. The amplitudes, however, were defined for each point in the beam; and the mode shape is determined by the manner in which these amplitudes are distributed. Therefore, since the damping is independent of amplitude, it must also be independent of mode shape. The practical consequence of this characteristic is that a single specimen may be used to obtain data for several different frequencies by simply exciting different modes of vibration.

By following the steps of Eqs. (5) - (7), an equation identical in form to Eq. (9) can be developed for the mechanical model shown in Fig. 4. Thus, the model faithfully reproduces the damping characteristics predicted by the Zener Theory.

Before leaving the topic of linear material damping, it is instructive to consider the stress-strain hysteresis loop of a linear solid as shown in Fig. 5. The elliptic shape is a consequence of the linearity of the material model and does not occur for nonlinear materials. The hysteresis loop is a useful concept since the energy lost per cycle is related to the area enclosed by the hysteresis loop. This concept will be quite useful when nonlinear damping mechanisms are considered since classical linear components will no longer be sufficient to describe the phenomena.

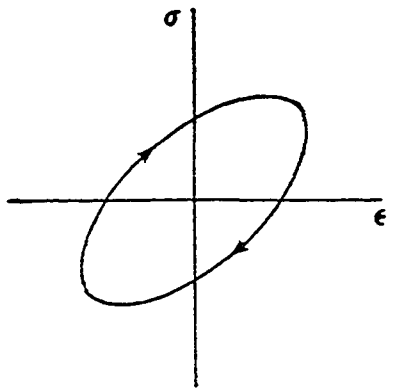

Fig. 5. Hysteresis loop for a linear solid

Nonlinear damping arises from several mechanisms as reported by Lazan [11]. Among the more important nonlinear mechanisms is "plastic strain" damping. This mechanism does not require general plastic strain throughout the specimen, but it is assumed that the plastic strain occurs on a microscopic scale due to inhomogeneities within the crystal.

Several authors have offered analytical theories of plastic strain damping. Dawson [17], Whiteman [18], and Whaley [19,20] have developed different plastic strain-based theories for material damping and material constitutive laws. These theories include a constitutive law which assumes that the plastic strain rate is dependent on stress and stress rate [17], a mathematical model for the hysteresis loop based on a large number of elastoplastic elements [18], and a

mathematical damping model based on local random yielding [19,20]. Since there appears to be no consensus of opinion on precisely what plastic strain mechanism is operating on a microscopic scale, a somewhat more macroscopic view may be considered which still provides some insight into the mechanism.

Consider the typical stress-strain hysteresis loop for a nonlinear material shown in Fig. 6. The energy lost per cycle, D, is proportional to the area enclosed by the hysteresis loop. For plastic strain damping, the energy absorbed per cycle may be written as

$$D = J\sigma_a^{\,n} \tag{11}$$

where

J and n are material constants,

J = damping energy at stress amplitude of unity,

n = damping exponent.

Substituting Eq. (11) into Eq. (1) and making use of elementary strain energy concepts yields

$$\eta = \frac{EJ\ \sigma_a^{\,m}}{\pi} \tag{12}$$

where $m = n - 2$.

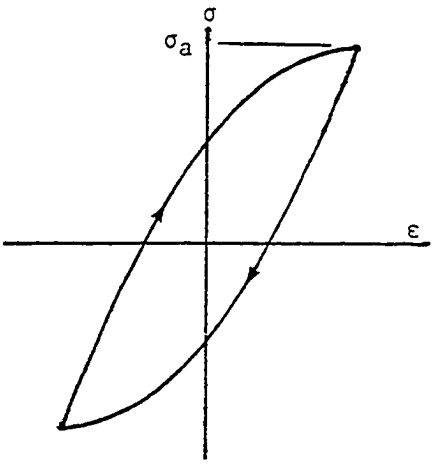

Fig. 6. Typical hysteresis loop for a nonlinear solid

It is of interest to note that for a linear material, n = 2, and the elliptic hysteresis loop seen in Fig. 5 is obtained. The corresponding loss factor as obtained from Eq. (12) is seen to be independent of amplitude as predicted by Zener [12].

For plastic strain damping, however, the loss factor is proportional to the cyclic stress amplitude raised to some power, m = n - 2. The value of m is a material property; however, this property is dependent on the stress amplitude and the material's stress history. Crandall [16] shows that m is small, between zero and one, for stress amplitudes less than the fatigue strength but may be twenty or greater for stresses above the fatigue strength, depending on the stress history.

The stress amplitude appears to be important only in cases where the amplitude of the previous stresses are greater than about 80% of the fatigue limit of the material. It is believed that stress levels below this value do not contribute a significant amount of fatigue damage to the material and, thus, do not add a significant number of new sites for local plastic strain to occur. If the material has been highly stressed, the stress history may play a significant role in the dependence of damping on stress amplitude. In mild steel, for example, a stress history of 300 cycles at 108% of the fatigue limit increases the loss factor by a factor of 20 over that of an unstressed specimen.

Thus, plastic strain damping is dependent on the stress amplitude and, therefore, dependent on the amplitude of vibration. It is also important to note that plastic strain damping is independent of frequency since no relaxation mechanisms are considered.

Another nonlinear mechanism which may lead to a significant energy loss from a vibrating member is magnetoelastic damping observed in ferromagnetic metals. A ferromagnetic material is made up of a large number of small regions or domains, each of which is individually magnetized and randomly oriented. Due to the magnetostrictive effect, the application of a strong magnetic field induces a strain field in the material as the domain vectors rotate and domain walls move to align with the magnetic field. Conversely, a strain field can

produce domain vector rotation and domain wall movement. Thus, a cyclic stress induces not only a cyclic strain, but also a cyclic magnetic domain reorientation. This process requires an input of energy which is identified as the damping.

Motogi [21] noted that above a certain threshold strain level, the stress-strain curve for certain ferromagnetic materials becomes linear and hysteresis disappears. Thus, above the threshold strain level, domain rotation and wall movement no longer increase; and the loss factor decreases sharply as noted by Lazan [11] and Adams [22]. This occurrence is quite reasonable since the domain vectors should rotate toward alignment with the strain field fairly quickly and, once that has occurred, increasing the strain will only cause Poisson's Ratio type movements in the domain walls.

Adams [22] showed that magnetoelastic damping is the primary damping mechanism operating in ferromagnetic materials at moderate stress levels. By applying a saturating magnetic field to the specimen so that the domains were aligned prior to testing, the damping was reduced to about that predicted by the Zener Theory. Thus, the primary source of nonlinear damping in ferromagnetic materials at moderate stress levels is magnetoelastic damping.

A great deal of effort has been placed into the characterization, both static and dynamic, of fiber reinforced composite materials as noted by Gibson and Plunkett [23] and

Gibson [24]. Bert [25] states that the damping in such materials is primarily due to damping within the matrix material and to slip at the fiber-matrix interface. The matrix material is often an epoxy which has been shown by Gibson and Plunkett [15,26] to exhibit viscoelastic damping, similar to that predicted by the Kelvin-Voigt model. The interfacial slip introduces nonlinear Coulomb friction damping which is discussed by Den Hartog [27] and Plunkett [28]. Gibson, Yau, and Riegner [29] and Gibson, Chaturvedi, and Sun [30] have investigated the interaction between the matrix and interface characteristics in chopped fiber composites and have concluded that the damping is most strongly affected by the matrix characteristics. Thus, fiber reinforced epoxies exhibit primarily linear material damping characteristics at sufficiently low stress levels for interfacial slip to be insignificant.

As the preceding discussion illustrated, the issue of material damping is clouded by many possible mechanisms which may be acting in concert. These different mechanisms may have different regions in which each is dominant. An example of this is the damping of mild steel. Mild steel exhibits linear damping, following the Zener Theory, for stress amplitudes less than 300 psi. For stress amplitudes in the range from 300 psi to 29,000 psi, the loss factor increases in a manner roughly proportional to the increase in stress amplitude with no dependence on stress history. This region is probably

controlled by a low stress, locally plastic, strain mechanism. Above 29,000 psi, the loss factor increases dramatically with stress amplitude and is strongly dependent on stress history, indicating that a high stress plastic strain mechanism is dominant.

Applications of Material Damping

Material damping is of practical interest for three basic reasons: fundamental understanding of material behavior, vibration control, and damage assessment. Consider first the field of material behavior, in which the main effort is expended in attempting to obtain a more complete understanding of the damping mechanisms. The improved understanding has led to the fractional calculus constitutive model development as was noted previously.

The role of material damping in vibration control has recently become a popular field for research and analysis. The inclusion of material damping in finite element formulation has been proposed by Golla and Hughes [31] to provide more accurate dynamic analyses than were possible with previous methods. Misra and Modi [32] included material damping in their Lagrangian development of the equations of motion for a satellite with flexible members since material damping was essentially the only damping existing on the space structure.

The practice of adding high damping, viscoelastic materials to structures for vibration and sound radiation control

has become very popular. The increased usage of these materials has led to an increased understanding of viscoelastic damping as noted by Jones [10], Mead [33], and Nashif, Jones, and Henderson [34].

Nondestructive evaluation of mechanical components and structures for flaws and fatigue damage has become a very popular and important field of study. Many nondestructive testing techniques have been developed, ranging from X-ray imaging to ultrasonic inspection. Vibration studies have been used in two different ways for damage assessment. The first use of vibration for damage assessment is through the reduction in the resonant frequency of a specimen due to the decreased stiffness of the specimen resulting from the damage. This approach has been used with moderate success by Adams, Cawley, Pye, and Stone [35], Haisty and Springer [36], and Reznicek and Springer [37].

The second application of vibration analysis to damage assessment is the measurement of material damping as an indication of damage level. The damping is monitored periodically with increased damping corresponding to increased damage. This approach has been used for damage assessment and fatigue monitoring of fiber reinforced epoxy composites by DiBenedetto, Gauchel, Thomas, and Barlow [38] and Mantena, Place, and Gibson [39]. This methodology is not limited to composite materials or just fatigue monitoring. It has been shown by Whaley, Chen, and Smith [40] and Whaley [20] that

damping can be used to identify crack nucleation since the plastic strain field and, therefore, damping, changes significantly when a crack is nucleated. The monitoring of damping has also been used to indicate fatigue crack growth as reported by Jones and Warren [41]. Thus, vibration studies, and in particular material damping studies, have found wide application to the field of nondestructive evaluation and damage assessment.

Measurement of Material Damping

A great number of techniques have been used to measure material damping. Some of the more popular methods include free vibration decay, bandwidth, and resonant dwell. A brief review of these techniques follows, beginning with free vibration decay methods.

Several authors have used free vibration decay methods, including Lee and McConnell [42], Baker, Woolam, and Young [14], Sierakowski, Hemp, and Hokstad [43], and Stephens and Scavullo [44]. The free vibration decay methods usually utilize the logarithmic decrement as the measure of material damping. A typical test technique entails exciting the specimen in some manner, often an impulse load, then observing the decay in the response after the excitation is removed. The amplitude of the response decays exponentially with time, and the ratio of amplitudes for successive response peaks gives an indication of the damping. Once the logarithmic decrement has

been established, the loss factor may be determined as shown in Table 1.

Bandwidth methods for measuring damping have been popular for some time. Such methods entail exciting a specimen near its resonant frequency for a given mode and determining the resonant frequency as well as the frequencies for the half-power points of the response. This technique is sometimes called a "3-dB down" method since the half-power points are 3-dB down from the maximum response. Assuming small damping, the loss factor is given by $\eta = (f_2 - f_1)/f_n$ where f_1 and f_2 are the frequencies at the half-power points, and f_n is the resonant frequency. Investigators such as Lee and McConnell [42], Sierakowski, Hemp, and Hokstad [43], and Sorensen and Tarnow [45] have used bandwidth methods by sweeping a constant level input excitation through a frequency range to locate the maximum and half-power responses. With the recent development of high speed digital signal processing equipment, bandwidth methods utilizing the frequency response function and an impulse excitation have become popular because of the speed of making measurements. Such methods have been used by Hanson and Hampel [46], Mantena, Place, and Gibson [39], and Suarez, Gibson, and Deobald [47].

Resonant dwell methods have been presented by several investigators. In principal, a resonant dwell method entails exciting a specimen at some resonant frequency, taking measurements on some characteristics of this resonant response,

and, through some analysis, relating these measurements to material damping. The techniques vary in the types of specimens and excitation methods, quantities measured, and subsequent analysis performed.

Several investigators have performed resonant dwell tests on rod shaped specimens. Wegel and Walther [48] excited several materials in torsional vibration modes to obtain damping information. Longitudinal vibration of cylindrical rods has also been used. Laird and Kingsbury [49] and Norris and Young [50] used the transmissibility of axially driven rods to obtain the material damping. Adams [22] presents a method in which rod-like metal specimens were vibrated in their fundamental free-free axial mode at constant amplitude with a test frequency of 11,625 Hz. The damping was determined from the temperature rise at different locations along the specimen where the stress amplitude was known. The temperature rise was measured by thermocouples pressed against the specimens at various locations.

Hooker [51] excited hollow cylindrical specimens in torsional-flexural modes of vibration utilizing an inertia bar with an offset mass and permanent magnet/moving coil vibration generators. The generators also served as motion measurement devices. The material damping was determined by measuring the energy input to the system, equating it to the energy dissipated by damping, and relating it to the maximum strain energy

calculated from the motion of the inertia bar. The resonant frequencies for this work were in the vicinity of 35 Hz.

Basavanhally and Marangoni [52] investigated the damping of small square plates. The plates were simply supported along all edges and excited by a sinusoidal force applied at the center of the plate. The input force and resulting plate center response were measured using piezoelectric transducers. The damping was obtained from the phase lag between the input force and the plate center deflection.

The most popular resonant dwell techniques have used beam specimens. Crandall [16] discusses a technique in which cantilever beams of varying lengths were driven by an electrodynamic vibration exciter at their fundamental resonant frequency, and the resulting beam tip amplitude was measured using a microscope. A relationship between the base acceleration and beam tip amplitude was used to determine material damping. The tests were run over a frequency range of 50 to 500 Hz using thin metal specimens.

A large number of investigators have used double-cantilever beam specimens in conjunction with an electrodynamic shaker to determine material damping. The technique entails exciting a beam specimen at its midpoint with a vibration exciter giving, in essence, two cantilever beams of equal length. This arrangement is advantageous since the specimen causes no tipping imbalance of the exciter head. The specimen is then excited at a frequency corresponding to resonance of

each cantilever beam, leading to maximum beam tip deflections. A variety of techniques have been used to measure the beam tip deflection, with an appropriate relationship used to obtain the damping from the base and beam tip deflections. Strain gages placed near the base have been used by Gibson and Plunkett [15,26], Plunkett and Sax [53], Whaley and Chen [54], and Jones and Warren [41]. Whaley, Chen, and Smith [40] placed an accelerometer at the beam tip to obtain amplitudes. Direct measurement of the beam tip motion has been performed by Granick and Stern [55] using optical targets, and by Gibson, Yau, and Riegner [56] and Rogers [57] using noncontacting eddy current proximity transducers.

It is clear that there are a wide variety of methods for experimentally determined material damping. When evaluating the various methods, the advantages of each method must be considered. Among the more important characteristics of any test method are: speed of data gathering and analysis, sensitivity of the test method, and the ability to control the vibration amplitude. The bandwidth methods using impulsive loading tend to be the fastest due to the currently available digital signal processors. However, the sensitivity of bandwidth methods is compromised by the discrete nature of the digital signal processors since each line displayed by the processor represents a bandwidth and not a discrete frequency. Thus, significant error may be introduced into the loss factor calculation since the resonant and half-power amplitudes are

not precisely determined. The amplitude control capability of impulse loaded bandwidth methods is limited by the response characteristics of the test system. For example, the impulsive force required to obtain a desired amplitude at one point in the structure might cause a nonlinear response in the vicinity of the load application, thus, invalidating the test results.

The free vibration decay methods tend to be fairly fast and have reasonably good sensitivity. However, since they look for the reduction in vibration amplitude for successive cycles, usually averaged over several cycles, amplitude dependent damping is difficult to measure.

Resonant dwell methods tend to be the slowest methods since an excitation force must be applied at precisely the resonant frequency. However, these methods generally give good sensitivity and the best control of vibration amplitude. Thus, the different methods have merits which an investigator must consider before selecting a test method.

CHAPTER III. THE PROPOSED METHOD

Motivation for the Proposed Method

The technique described in the current work is a modification of resonant dwell approach developed by Gibson, Yau, and Riegner [56]. The method of Gibson et al. [56], hereafter called Gibson's method, was used by Rogers [57] to determine the damping characteristics of several materials. During these tests, measurement difficulties were encountered as a result of the test condition employed. An understanding of these testing difficulties requires a brief review of Gibson's method.

In Gibson's technique, a beam specimen was driven at its center by an electrodynamic vibration exciter as shown in Fig. 7. This arrangement is equivalent to two cantilever beams excited by base motion. The base motion was measured by an accelerometer mounted in the exciter head while the beam motion near its free ends was measured by noncontacting eddy current proximity transducers. The specimen loss factor was obtained from

$$\eta = \frac{\left(\frac{\ddot{y}_o}{\omega_r^2}\right) C_r \phi_r(x_o)}{\phi_r(L) y(x_o)} \qquad (13)$$

where

η = the loss factor,

$\ddot{y}_o$ = the base acceleration amplitude,

ω_r = the angular natural frequency of the rth mode,

$\phi_r(x_o)$, $\phi_r(L)$ = mode shape constants tabulated in Bishop and Johnson [58],

C_r = a constant for each mode,

$y(x_o)$ = the displacement amplitude at the probe location.

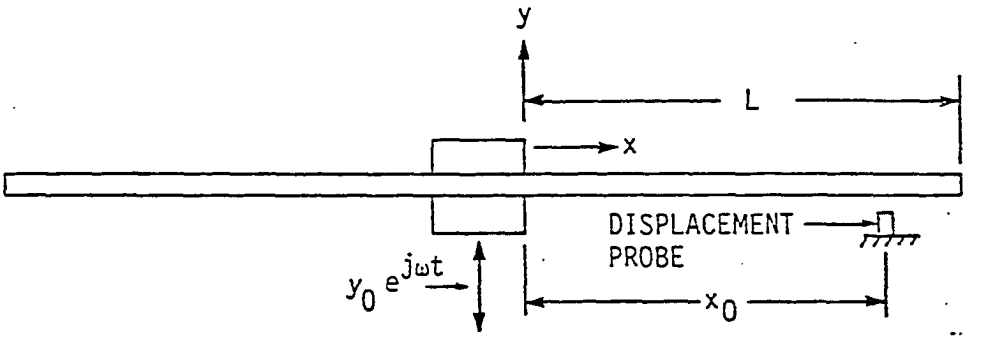

Fig. 7. Experimental set up for tests using Gibson's method

In order for Eq. (13) to be valid, the specimen must be excited at the cantilever beam resonance condition. In this test condition, the cantilever beams act as a dynamic absorber for the exciter head and attachment mass, causing the cantilever base to be nearly motionless. If the test is run with

constant base acceleration amplitude in the feedback control, the driving force requirements increase dramatically near the cantilever test condition as can be seen from the driving force relationship

$$\left|F_o(\omega)\right| = \ddot{y}_o \left| 2m_{base}\omega^2(1 + \cos\beta_r L\cosh\beta_r L) + 4EI\beta_r{}^3(\cos\beta_r L\sinh\beta_r L + \sin\beta_r L\cosh\beta_r L)\right| \frac{1}{2\omega^2(1+\cos\beta_r L\cosh\beta_r L)} \qquad (14)$$

where β_r = the system eigenvalue.

The maximum beam tip displacement occurs at the cantilever beam resonant condition which corresponds to antiresonance of the beam and base mass system. The cantilever beam resonance requires that

$$1 + \cos\beta_r L\cosh\beta_r L = 0 \qquad (15)$$

For the test condition defined by Eq. (15), it is clear that the driving force must be quite large. Rogers [57] reported that distortion of the base acceleration signal occurred for this test condition. The base motion distortion is believed to be due to the large driving force requirements placed on the electrodynamic exciter. Since the sinusoidal base motion was assumed in the derivation of Eq. (13), the distortion of the base acceleration jeopardizes the validity of this approach.

In addition to the distortion problem, Gibson's method requires the measurement of the beam deflection near a free end of the beam. The deflection is measured using a non-contacting eddy current proximity transducer. There are several problems or uncertainties associated with using these transducers. The probe itself has a significant measurement area, about a one-fourth inch diameter circle, so the exact location of the probe deflection measurement contains some uncertainty. Also, the deflection measurement assumes that the probe is fixed. Due to the transmission of energy from the exciter into the supporting structure, and other building vibration sources, it is difficult to obtain complete fixity of the proximity probe. Therefore, the output signal from the proximity probe is actually due to the relative motion between the beam and the probe which introduces additional and unknown measurement error.

The proposed method is appealing for several reasons. A significant improvement over Gibson's method is the test condition of system resonance. The system resonance condition leads to a very small driving force since only damping must be overcome. The small driving force requirement allows the exciter to maintain the sinusoidal base motion which is assumed in the derivation, giving no base motion distortion errors.

An additional advantage of the proposed method is that only driving point measurements are required. The problems

associated with measurements along the length of the vibrating beam, such as vibration isolation of the measurement device or contamination of the test system by the measurement device, are avoided.

The measurement of the resonant driving force is required by the proposed method and must be carefully considered. At resonance the linear elastic and inertial forces cancel each other with only system damping and nonlinear force contributions remaining. Typically, these force contributions result from material damping, air damping, friction damping in the clamp, and nonlinear characteristics of the beam and exciter suspension. Therefore, filtering or frequency analysis of the force signal is necessary to isolate the material damping force from the other force contributions.

The force measurement problem is made more difficult by the low level of the force signal. The accurate measurement of the small resonant driving force is difficult due to the noise floor of the measurement system. Thus, measurements are valid only to a certain level, below which the measurement error is unacceptably large.

Measuring the driving force is quite attractive since it allows a direct measurement of damping via the damping force. By using frequency analysis of the force signal, the response of each of the previously mentioned force components to changing system parameters may be investigated. It is clear that the proposed method offers a potential for improved

fundamental understanding of material damping, air damping, and system nonlinear response.

Derivation

The theoretical development of the proposed technique follows the traditional method of first solving the undamped forced vibration problem and, then, incorporating damping into the solution by introducing the complex elastic modulus. The general equation for free lateral vibration of the right half of the double cantilever beam shown in Fig. 8, assuming that shear effects and rotary inertia are negligible, is given by Thomson [4] as

$$EI \frac{\partial^4 y}{\partial x^4} + \rho A \frac{\partial^2 y}{\partial t^2} = 0 \tag{16}$$

where

EI = flexural stiffness of the beam,

ρA = mass per unit length of the beam,

A = cross-sectional area of the beam.

A separation of variables solution for steady-state motion yields

$$y(x,t) = RE[(A_1 \sin\beta x + A_2 \cos\beta x + A_3 \sinh\beta x + A_4 \cosh\beta x) e^{j\omega t}] \tag{17}$$

where

$$\beta^4 = \frac{\omega^2 \rho A}{EI} . \tag{18}$$

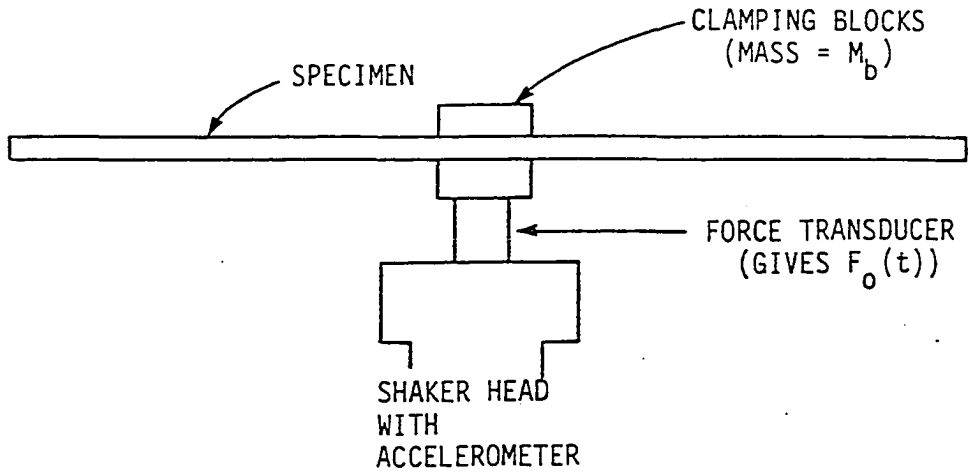

Fig. 8. Experimental set up for new method tests

The appropriate boundary conditions are

1. $\frac{\partial y(0,t)}{\partial x} = 0$, slope at the base is zero.

2. $EI \frac{\partial^2 y(L,t)}{\partial x^2} = 0$, moment at the free end is zero.

3. $EI \frac{\partial^3 y(L,t)}{\partial x^3} = 0$, shear at the free end is zero.

4. $y(0,t)$, is the motion of the shaker head.

Since Eq. (17) has four arbitrary constants, $A_1 - A_4$, imposing the four boundary condition will specify the values for these constants to within one arbitrary constant. The solution will then exist for certain values of the eigenvalue, β, which identifies each mode of vibration and which results from the boundary conditions.

Addressing these boundary conditions, respectively,

$$1.\quad \frac{\partial y(0,t)}{\partial x} = 0 = RE[\beta(A_1\cos\beta(0)-A_2\sin\beta(0)+A_3\cosh\beta(0) + A_4\sinh\beta(0))e^{j\omega t}]$$

$$\therefore A_1 + A_3 = 0 \qquad (19)$$

$$2.\quad EI\frac{\partial^2 y(L,t)}{\partial x^2} = 0 = RE[EI\beta^2(-A_1\sin\beta L-A_2\cos\beta L+A_3\sinh\beta L + A_4\cosh\beta L)e^{j\omega t}]$$

$$\therefore -A_1\sin\beta L-A_2\cos\beta L+A_3\sinh\beta L+A_4\cosh\beta L = 0 \qquad (20)$$

$$3.\quad EI\frac{\partial^3 y(L,t)}{\partial x^3} = 0 = RE[EI\beta^3(-A_1\cos\beta L+A_2\sin\beta L+A_3\cosh\beta L + A_4\sinh\beta L)e^{j\omega t}]$$

$$\therefore -A_1\cos\beta L+A_2\sin\beta L+A_3\cosh\beta L+A_4\sinh\beta L = 0 \qquad (21)$$

4. $y(0,t)$ is the motion of the shaker head.

Evaluation of the fourth boundary condition requires performing a force balance on the driven section of the beam; i.e., the section within the base clamping blocks as shown in Fig. 9. Inspecting the free body diagram of this section and performing the force balance yields

$$m_b\frac{\partial^2 y(0,t)}{\partial t^2} = RE[F_o(\omega)e^{j\omega t}] - 2V(0,t) \qquad (22)$$

where V(0,t) is the shear force at the edge of the clamping blocks.

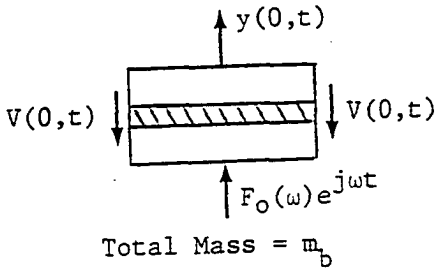

Fig. 9. Free-body diagram of specimen base

From Eq. (17) with x = 0

$$y(0,t) = RE[(A_2 + A_4)e^{j\omega t}] .$$

Differentiating twice with respect to time gives

$$\frac{\partial^2 y(0,t)}{\partial t^2} = RE[-\omega^2(A_2 + A_4)e^{j\omega t}] .$$

The shear may be written as

$$V(0,t) = EI \frac{\partial^3 y(0,t)}{\partial x^3} .$$

So Eq. (17) may be differentiated three times with respect to x to give

$$V(0,t) = RE[EI\beta^3(-A_1 + A_3)e^{j\omega t}] .$$

Substituting these relationships back into Eq. (22) gives

$$RE[m_b(-\omega^2)(A_2 + A_4)e^{j\omega t}] = RE[F_o(\omega)e^{j\omega t} - 2EI\beta^3(-A_1 + A_3)e^{j\omega t}] \quad (23)$$

which reduces to

$$-m_b\,\omega^2(A_2 + A_4) + 2EI\beta^3(A_3 - A_1) = F_o(\omega)\ . \quad (24)$$

The boundary conditions from Eqs. (19), (20), (21), and (24) may be written in matrix form as a 4 x 4 system. However, since Eq. (19) shows that $A_1 = -A_3$, this 4 x 4 system can be easily reduced to a more manageable 3 x 3 system given by

$$\begin{bmatrix} -\cos\beta L & \sin\beta L + \sinh\beta L & \cosh\beta L \\ \sin\beta L & \cos\beta L + \cosh\beta L & \sinh\beta L \\ -m_b\omega^2 & 4EI\beta^3 & -m_b\omega^2 \end{bmatrix} \begin{Bmatrix} A_2 \\ A_3 \\ A_4 \end{Bmatrix} = \begin{Bmatrix} 0 \\ 0 \\ Fo(\omega) \end{Bmatrix} \quad (25)$$

Solving Eq. (25) and remembering that $A_1 = -A_3$ gives values for the coefficients in Eq. (17) in terms of the magnitude of the driving force, $F_o(\omega)$. The system of equations may be solved using Cramer's Rule by first obtaining the determinant of the coefficient matrix which is given by

$$D = 2m_b\omega^2(1 + \cos\beta L\cosh\beta L) + \frac{4m\omega^2}{\beta L}(\cos\beta L\sinh\beta L + \sin\beta L\cosh\beta L) \quad (26)$$

where $m = \rho AL$, is the mass of one half of the beam.

This is also known as the characteristic frequency equation for the system and will be returned to later.

The solution to Eq. (25) is given by

$$A_2 = \frac{F_o(\omega)(\sin\beta L\sinh\beta L - \cos\beta L\cosh\beta L - 1)}{D} \quad (27)$$

$$A_3 = -A_1 = \frac{Fo(\omega)(\cos\beta L\sinh\beta L + \sin\beta L\cosh\beta L)}{D} \quad (28)$$

$$A_4 = \frac{-F_o(\omega)(1 + \cos\beta L\cosh\beta L + \sin\beta L\sinh\beta L)}{D} \quad (29)$$

By substituting Eqs. (27) - (29) into Eq. (17), a solution to the problem is obtained with all arbitrary constants determined. The displacement of the base is given from Eq. (17) by

$$y(0,t) = RE[\frac{-2F_o(\omega)}{D}(1 + \cos\beta L\cosh\beta L)e^{j\omega t}] \quad (30)$$

However, the base motion is measured by an accelerometer in the shaker head and is controlled as a sinusoid of known amplitude, $\ddot{y}_o$. This base acceleration is obtained by differentiating Eq. (30) twice with respect to time giving

$$\frac{\partial^2 y(0,t)}{\partial t^2} = RE[\frac{2\omega^2 F_o(\omega)}{D}(1 + \cos\beta L\cosh\beta L)e^{j\omega t}]$$

$$= RE[\ddot{y}_o e^{j\omega t}] \quad (31)$$

The driving force amplitude, $F_o(\omega)$, may be solved for in terms of the base acceleration amplitude, $\ddot{y}_o$, as

$$F_o(\omega) = \frac{\ddot{y}_o D}{2\omega^2(1 + \cos\beta L \cosh\beta L)} \tag{32}$$

The driving force for the undamped system is seen to be proportional to the base acceleration amplitude and the value of the characteristic frequency equation, D, from Eq. (26). For the case of system resonance, the value of D is zero; and, therefore, the required driving force is zero. It is of interest to note that the denominator of Eq. (32) contains the characteristic frequency equation for a cantilever beam of length L. Thus, the force required to drive the system at the cantilever beam resonant condition becomes infinite which corresponds to the condition of system antiresonance used previously in Gibson's method.

Now it is appropriate to incorporate damping into Eq. (32) and solve for the damping in terms of measurable characteristics of the vibrating beam system. The damping may be incorporated in terms of the complex modulus of elasticity, $E^* = E(1 + j\eta)$. The complex beam stiffness, EI^* is given by

$$EI^* = EI(1 + j\eta) \tag{33}$$

Substituting Eq. (33) into Eq. (18), the complex eigenvalue is given by

$$\beta^* = \left[\frac{\omega^2 \rho A}{EI(1 + j\eta)}\right]^{1/4} \tag{34}$$

or

$$\beta^* = \left[\frac{\omega^2 \rho A}{EI(1 + \eta^2)}\right]^{1/4} (1 - j\eta)^{1/4} \tag{35}$$

then for small damping ($\eta << 1$) it follows that

$$(1 + \eta^2)^{1/4} \approx 1 \ . \tag{36}$$

This assumption introduces 1% error for $\eta = 0.2$. For the current work, the largest damping encountered gave values for η less than 0.02; thus, the assumption is reasonable. With similar justification it may be stated that

$$(1 - j\eta)^{1/4} \approx \left(1 - j\,\frac{\eta}{4}\right). \tag{37}$$

Thus, the complex eigenvalue, β^*, may be rewritten using Eqs. (35) - (37) as

$$\beta^* = \left[\frac{\omega^2 \rho A}{EI}\right]^{1/4} \left(1 - j\,\frac{\eta}{4}\right)$$

which reduces to

$$\beta^* = \beta\left(1 - j\,\frac{\eta}{4}\right) \tag{38}$$

Substituting Eq. (38) into Eq. (26) gives the complex characteristic equation

$$D^* = 2m_b\omega^2(1 + \cos\beta^*L\cosh\beta^*L) = \frac{4m\omega^2}{\beta L}(1 + j\frac{\eta}{4})$$

$$(\cos\beta^*L\sinh\beta^*L + \sin\beta^*L\cosh\beta^*L) \qquad (39)$$

The driving force with damping included is obtained by substituting Eq. (39) into Eq. (32), yielding

$$F_o^*(\omega) = \frac{\ddot{y}_o D^*}{2\omega^2(1 + \cos\beta^*L\cosh\beta^*L)} \qquad (40)$$

$$= \frac{\ddot{y}_o}{2\omega^2}[2m_b\omega^2(1+\cos\beta^*L\cosh\beta^*L) + \frac{4m\omega^2}{\beta L}(1 + j\frac{\eta}{4})$$

$$(\cos\beta^*L\sinh\beta^*L + \sin\beta^*L\cosh\beta^*L)]$$

$$\frac{1}{(1 + \cos\beta^*L\cosh\beta^*L)} \qquad (41)$$

Substituting Eq. (38) into Eq. (41) gives

$$F_o(\omega) = \frac{P^*}{Q^*}\frac{\ddot{y}_G}{2} \qquad (42)$$

where

$$P^* = 2m_b[1 + \cos\beta L(1 - j\frac{\eta}{4})\cosh\beta L(1 - j\frac{\eta}{4})] +$$

$$\frac{4m}{\beta L}(1 + j\frac{\eta}{4})[\cos\beta L(1 - j\frac{\eta}{4})\sinh\beta L(1 - j\frac{\eta}{4}) +$$

$$\sin\beta L(1 - j\frac{\eta}{4})\cos\beta L(1 - j\frac{\eta}{4}] \qquad (43)$$

and

$$Q^* = 1 + \cos\beta L(1 - j\frac{\eta}{4})\cosh\beta L(1 - j\frac{\eta}{4}) \qquad (44)$$

Equation (42) can be simplified by expanding the numerator and denominator, Eqs. (43) and (44), separately and utilizing the identities

$$\left.\begin{aligned}
\sin(\theta \pm j\phi) &= \sin\theta\cosh\phi \pm j\cos\theta\sinh\phi \\
\cos(\theta \pm j\phi) &= \cos\theta\cosh\phi \mp j\sin\theta\sinh\phi \\
\sinh(\theta \pm j\phi) &= \sinh\theta\cos\phi \pm j\cosh\theta\sin\phi \\
\cosh(\theta \pm j\phi) &= \cosh\theta\cos\phi \pm j\sinh\theta\sin\phi
\end{aligned}\right\} \qquad (24)$$

Consider first the numerator, P*, which may be written as

$$P^* = 2m_b[1 + (\cos\beta L\cosh\eta\frac{\beta L}{4} + j\sin\beta L\sinh\eta\frac{\beta L}{4}) \cdot$$

$$(\cosh\beta L\cos\eta\frac{\beta L}{4} - j\sinh\beta L\sin\eta\frac{\beta L}{4})] + \frac{4m}{\beta L}(1 + j\frac{\eta}{4}) \cdot$$

$$[(\cos\beta L\cosh\eta\frac{\beta L}{4} + j\sin\beta L\sinh\eta\frac{\beta L}{4})(\sinh\beta L\cos\eta\frac{\beta L}{4} -$$

$$j\cosh\beta L\sin\left(\eta\frac{\beta L}{4}\right) + \left(\sin\beta L\cosh\left(\eta\frac{\beta L}{4}\right) - j\cos\beta L\sinh\left(\eta\frac{\beta L}{4}\right)\right)\cdot$$

$$\left(\cosh\beta L\cos\left(\eta\frac{\beta L}{4}\right) - j\sinh\beta L\sin\left(\eta\frac{\beta L}{4}\right)\right)] \qquad (46)$$

For all cases considered in this work, the product $\eta\beta L/4$ was always less than 0.1. Thus, with a maximum error of 0.5% it could be assumed that

$$\left.\begin{aligned}\sinh\left(\eta\frac{\beta L}{4}\right) &= \sin\left(\eta\frac{\beta L}{4}\right) = \eta\frac{\beta L}{4}\\ \cosh\left(\eta\frac{\beta L}{4}\right) &= \cos\left(\eta\frac{\beta L}{4}\right) = 1\end{aligned}\right\} \qquad (47)$$

Making this substitution, it can be shown that Eq. (46) simplifies to

$$P^* = [2m_b(1 + \cos\beta L\cosh\beta L) + \frac{4m}{\beta L}(\cos\beta L\sinh\beta L +$$

$$\sin\beta L\cosh\beta L)] + \eta^2\left(\frac{\beta L}{4}\right)^2\{2m_b\sin\beta L\sinh\beta L +$$

$$[(\sin\beta L\cosh\beta L - \cos\beta L\sinh\beta L) + \frac{1}{\beta L}(2\cos\beta L\cosh\beta L)]\frac{4m}{\beta L}\}$$

$$+ j\{\eta\frac{\beta L}{4}[2m_b(\sin\beta L\cosh\beta L - \cos\beta L\sinh\beta L) + \frac{4m}{\beta L}$$

$$[\frac{1}{\beta L}(\cos\beta L\sinh\beta L + \sin\beta L\cosh\beta L) - (2\cos\beta L\cosh\beta L)]] +$$

$$\eta^3\left(\frac{m\beta L}{16}\right)(\sin\beta L\cosh\beta L - \cos\beta L\sinh\beta L)\} \; . \qquad (48)$$

Now consider the denominator, Q*, which may be written as

$$Q^* = 1 + (\cos\beta L\cosh \eta \frac{\beta L}{4} + j\sin\beta L\sinh \eta \frac{\beta L}{4}) \cdot$$

$$(\cosh\beta L\cos \eta \frac{\beta L}{4} - j\sinh\beta L\sin \eta \frac{\beta L}{4}) \ . \qquad (49)$$

As before, Eq. (47) may be substituted into Eq. (49) yielding

$$Q^* = 1 + \cos\beta L\cosh\beta L + \eta^2(\frac{\beta L}{4})^2 \sin\beta L\sinh\beta L +$$

$$j \frac{\eta\beta L}{4} (\sin\beta L\cosh\beta L - \cos\beta L\sinh\beta L) \ . \qquad (50)$$

For small damping, higher order terms in the loss factor may be neglected. Then Eqs. (48) and (50) reduce to

$$P^* = [2m_b(1 + \cos\beta L\cosh\beta L) + \frac{4m}{\beta L} (\cos\beta L\sinh\beta L +$$

$$\sin\beta L\cosh\beta L)] + j \eta \frac{\beta L}{4} \{2m_b(\sin\beta L\cosh\beta L -$$

$$\cos\beta L\sinh\beta L) + \frac{4m}{\beta L} [\frac{1}{\beta L}(\cos\beta L\sinh\beta L +$$

$$\sin\beta L\cosh\beta L) - 2\cos\beta L\cosh\beta L]\} \qquad (51)$$

and

$$Q^* = 1 + \cos\beta L\cosh\beta L + j \eta \frac{\beta L}{4} (\sin\beta L\cosh\beta L -$$

$$\cos\beta L\sinh\beta L) \ . \qquad (52)$$

The error associated with neglecting these terms is dependent on the loss factor, the mass ratio, and the resonant mode number. For the cases tested in this work, the error was always less than 0.5%. Thus, the simplified equations (51) and (52) are acceptable.

Consider now the first bracketed term of Eq. (51). Comparing this to Eq. (26), it is clear that the bracketed term is just D/ω^2. Since the test condition of system resonance is achieved when $D = 0$, Eq. (51) reduces to

$$P^* = j\,\eta\,\frac{\beta L}{4}\{2m_b(\sin\beta L\cosh\beta L - \cos\beta L\sinh\beta L) + \frac{4m}{\beta L}\left[\frac{1}{\beta L}(\cos\beta L\sinh\beta L + \sin\beta L\cosh\beta L) - 2\cos\beta L\cosh\beta L\right]\}. \tag{53}$$

In order to evaluate the ratio P^*/Q^* it is necessary to obtain the magnitude of each term. The magnitude of P^* is given by Eq. (53) with the complex j removed. The magnitude of Q^* is not so easily obtained since Eq. (52) contains both real and imaginary parts. However, the loss factor appears only in the imaginary part of Eq. (52) and, since the loss factor is small, the magnitude of Q^* may be approximated by the real part of Eq. (52).

As with previous approximations, neglecting the imaginary part of Eq. (52) introduces some error. The error is dependent on the loss factor, the mode number and the mass ratio. For the current work, the error introduced by this

approximation was always less than 2%. Thus, for the cases tested in this work, the approximation is acceptable.

The magnitude of the driving force is given by Eq. (42) as

$$\left|F_o^*(\omega)\right| = \frac{\left|P^*\right|}{\left|Q^*\right|}\frac{\ddot{y}_o}{2} . \tag{54}$$

The loss factor is given explicitly by rewriting Eq. (54) and substituting for $|P^*|$ and $|Q^*|$ yielding

$$\eta = \frac{\left|F_o^*(\omega)\right| C_1}{\ddot{y}_o(\frac{m}{2})\left|(\frac{m_b}{2m})C_2 + C_3\right|} \tag{55}$$

where

$$C_1 = \left|\beta L(1 + \cos\beta L\cosh\beta L)\right|,$$

$$C_2 = (\beta L)^2(\sin\beta L\cosh\beta L - \cos\beta L\sinh\beta L),$$

$$C_3 = (\cos\beta L\sinh\beta L + \sin\beta L\cosh\beta L) - 2\beta L\cos\beta L\cosh\beta L,$$

$$m = \rho AL = \text{mass of 1/2 of the beam.}$$

Thus, the loss factor is obtained from the amplitudes of the driving force and base acceleration for known mode numbers and system masses. It is important to note that the base mass, m_b, includes the mass of the clamping blocks and screws, the mass of the beam between the block surfaces, and the seismic mass of the force transducer.

The validity of Eq. (55) was based on the validity of several assumptions involving the loss factor, the mode

number, and the mass ratio. For the current work these assumptions were sufficiently good to use Eq. (55). However, the errors associated with the assumptions becomes unacceptably large for loss factors greater than 0.05 tested in the third mode of vibration with the errors increasing for higher modes and larger mass ratios. If tests are run under these circumstances, Eq. (55) is no longer valid. A correct solution may be obtained for these cases by obtaining the magnitudes of P* and Q* from Eqs. (48) and (50), substituting them into Eq. (54) and iterating on values of the loss factor until convergence. This method, although inconvenient, will result in accurate values of the loss factor for a large range of system parameters.

Measurement Sensitivity to System Parameters

It is important to understand how the system parameters can affect the measurement of damping. Typically, a sensitivity analysis is performed on the measurement equation to determine these effects. Following from Dally, Riley, and McConnell [59], the sensitivity of the loss factor to the measured variables is given from Eq. (55) as

$$\frac{d\eta}{\eta} = \left[\left(\frac{dF_o^*(\omega)}{F_o^*}\right)^2 + \left(\frac{d\ddot{y}_o}{\ddot{y}_o}\right)^2 + \left(\frac{\partial\eta}{\partial m}\frac{dm}{\eta}\right)^2 + \left(\frac{\partial\eta}{\partial m_b}\frac{dm_b}{\eta}\right)^2 + \left(\frac{\partial\eta}{\partial\omega}\frac{d\omega}{\eta}\right)^2\right]^{1/2} \tag{56}$$

The effect of the uncertainties in the half-beam mass, m; the base mass, m_b; and the driving frequency, ω, is difficult to determine. The difficulty arises due to the complicated manner in which these terms enter into the loss factor equation. Specifically, the mass terms are important in the characteristic equation, Eq. (26). Small errors in the mass measurements can lead to errors in the beam parameter as determined by setting Eq. (26) equal to zero. These errors, in turn, lead to errors in the C's in Eq. (55). The magnitude of the resulting error in the loss factor is dependent on the mass ratio ($m_b/2m$) and the resonant mode number.

The error associated with the driving frequency is the error introduced by missing the test condition defined by setting Eq. (26) equal to zero. The resulting error in the loss factor is dependent on the mass ratio and the resonant mode number. Thus, it is difficult to extract useful sensitivity information from Eq. (56).

A more informative measure of the sensitivity may be obtained by investigating the effect of the loss factor on the driving force. This may be done by first rewriting the driving force from Eq. (40) in the form

$$F_o^*(\omega) = \frac{2m\,\ddot{y}_o(A + j\eta B)}{(a + j\eta b)} \qquad (57)$$

where

$$A = (m_b/2m)(1 + \cos\beta L\cosh\beta L) + (\cos\beta L\sinh\beta L + \sin\beta L\cosh\beta L)/(\beta L)$$

$$B = (m_b/2m)(\beta L/4)(\sin\beta L\cosh\beta L - \cos\beta L\sinh\beta L) + (\cos\beta L\sinh\beta L + \sin\beta L\cosh\beta L)/(4\beta L) - (\cos\beta L\cosh\beta L)/2$$

$$a = 1 + \cos\beta L\cosh\beta L$$

$$b = (\beta L/4)(\sin\beta L\cosh\beta L - \cos\beta L\sinh\beta L) .$$

It is of interest to obtain the sensitivity of the driving force to the loss factor for various values of the mass ratio for each natural frequency. The sensitivity may be described by the partial derivative $\partial F_o^*(\omega)/\partial\eta$ normalized by the ratio $F_o^*(\omega)/\eta$. Before performing the differentiation it should be noted that for the test condition of system resonance the term A from Eq. (57) equals zero, which is identical to setting Eq. (26) equal to zero. Differentiating Eq. (57) gives the sensitivity as

$$\frac{\partial F_o^*(\omega)/\partial\eta}{F_o^*(\omega)/\eta} = \frac{1}{\sqrt{1 + (b\eta/a)^2}} . \qquad (58)$$

Clearly, the sensitivity has a maximum value of 1 and is dependent on the value of the loss factor and on the beam parameter, βL. However, the beam parameter is dependent on the mass ratio through Eq. (26). To obtain an understanding of the effect of the mass ratio on the sensitivity, the sensitivity is plotted against the mass ratio for the first three resonant modes and two values of the loss factor in Fig. 10.

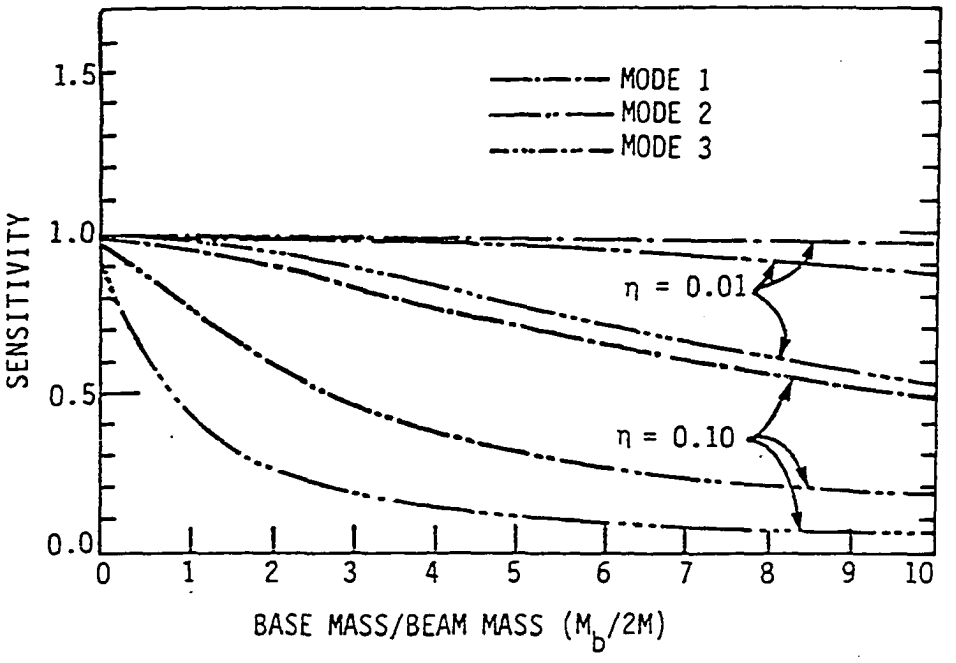

Fig. 10. Effect of mass ratio on the sensitivity ratio

It is clear from Fig. 10 that the sensitivity is dependent on the mass ratio, loss factor, and resonant mode number, with the sensitivity decreasing for an increase in the value of any of these parameters. The damping seems to have the strongest effect on the sensitivity since the curves for a loss factor of 0.1 lie below the curves for a loss factor of 0.01. For the higher damping case, the effects of mode number and mass ratio are also accentuated. Thus, for large damping, good sensitivity may only be obtained for very low mass ratios and low mode numbers. For the case of small damping, however, good sensitivity may be obtained for a wider range of mass ratios and mode numbers.

Another way to investigate the effects of the parameters on Eq. (58) is to examine the (b/a) ratio as a function of the mass ratio for the first three resonant modes. The sensitivity decreases for increasing values of the (b/a) ratio; thus, investigating this relationship may give some insight into the effects of mass ratio and mode number on the sensitivity. The (b/a) ratio is shown, in Fig. 11, as a function of mass ratio for mass ratios from zero to ten and for the first three resonant modes. The figure shows that the mode number has a strong influence on the (b/a) ratio, with the (b/a) ratio increasing dramatically with increasing mode number. A similar relationship exists between the (b/a) ratio and the mass ratio, with the (b/a) ratio increasing with increasing mass ratio for all mode numbers considered.

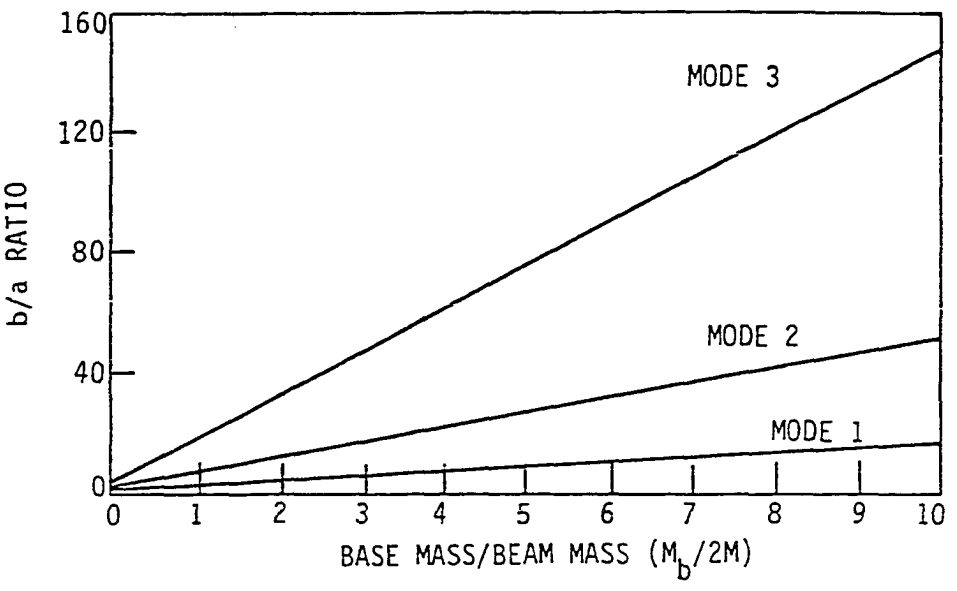

Fig. 11. Effect of mass ratio on the b/a ratio

In searching for an explanation for these trends, it was decided to calculate the driving point apparent mass (defined as the ratio of the driving force to the driving point acceleration, $F_0^*(\omega)/\ddot{y}_0$) for the lightly damped case where $\eta = 0.001$. This was done for mass ratios of nearly zero (0.001) and ten, and both cases are plotted against frequency in Fig. 12. When the apparent mass is large, the vibrating system is in a condition of antiresonance where the vibrating mass (i.e., the beam) is trying to hold the driving point at zero motion like a dynamic absorber. When the apparent mass is small, the system is at resonance where the driving force must overcome only the damping forces in the system. When the mass ratio is small, the system behaves like a free-free beam of length 2L at resonance, and a pair of cantilever beams of length L at antiresonance. This behavior gives maxima and minima (antiresonances and resonances) that are widely separated in frequency as shown in Fig. 12a.

When the mass ratio is large; e.g., 10, the resonant and antiresonant frequencies become nearly the same since the large base mass causes the free-free beam resonant condition to approach that of the cantilever beam. This case is shown in Fig. 12b. It is instructive to consider the reason for this behavior and some of its implications. The shifting of the resonant response from the free-free to the cantilever behavior can be seen by inspecting the characteristic frequency equation, Eq. (26), or the term A in Eq. (57) since they are

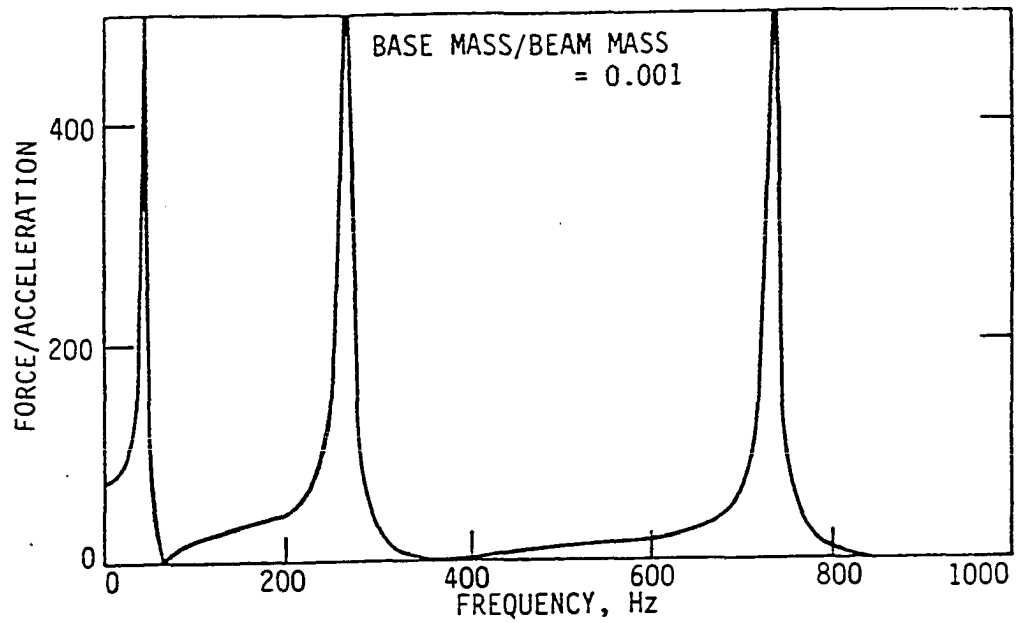

(a)

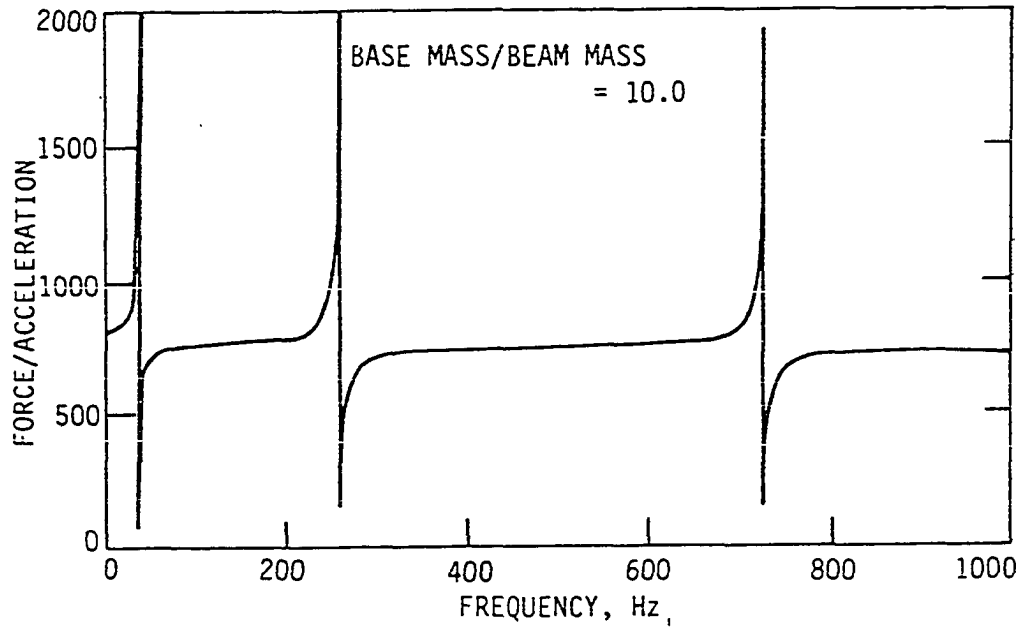

(b)

Fig. 12. Apparent mass vs frequency for mass ratios of (a) 0.001; (b) 10.0

equivalent expressions. Consider the term A in Eq. (57) where the mass ratio appears explicitly. For a very small mass ratio, the characteristic frequency equation tends toward

$$\cos\beta L \sinh\beta L + \sin\beta L \cosh\beta L = 0 \qquad (59)$$

which has been shown by Snowdon [60] to be the characteristic equation for a free-free beam of length 2L. As the mass ratio becomes large, the first term of the system characteristic equation becomes dominant, giving a limiting characteristic equation of

$$1 + \cos\beta L \cosh\beta L = 0 \qquad (60)$$

which is shown by Snowdon [60] to be the characteristic equation for a cantilever beam of length L. Thus, the behavior shown in Fig. 12 should not be unexpected.

A practical consideration based on the behavior shown in Fig. 12 is that of selecting a mass ratio for optimal testing conditions. It is evident from Fig. 12 that large changes in the driving force occur for very small changes in frequency when the mass ratio is large. This makes it difficult to separate out the damping forces from the other forces that are rapidly changing with frequency.

Based on the preceding discussion, it is clear that for optimal sensitivity and measurement ease the mass ratio should be as small as possible.

An additional area of interest which is important to the identification of system parameters, although not directly related to sensitivity, is the method of establishing the resonant test condition. There are two basic pieces of information needed to detect the presence of a resonant condition. The first is the phase shift between the input force and the resulting base acceleration. This relationship is shown in Fig. 13 for a loss factor of $\eta = 0.001$ and mass ratios of 0.001 and 10. It is evident that the phase shift is near -90 degrees ($-\pi/2$ radians) at both the antiresonant and resonant frequencies for a lightly damped system. An examination of Eq. (57) suggests that the phase angle will not be -90 degrees for a heavily damped system since the denominator would then introduce a significant phase shift. It is also interesting to note that the range of frequencies over which the phase angle is minus 180 degrees is reduced for the higher mass ratio since the resonant frequencies are approaching the corresponding antiresonant frequencies.

The second piece of information is the magnitude of the force required to drive the system when the phase angle is near -90 degrees. The antiresonance is characterized by a very large driving force for this phase condition while resonance is characterized by a minimum driving force. Thus, the test condition of system resonance can be obtained by adjusting the driving frequency so that the phase shift is near -90 degrees and the driving force is a minimum.

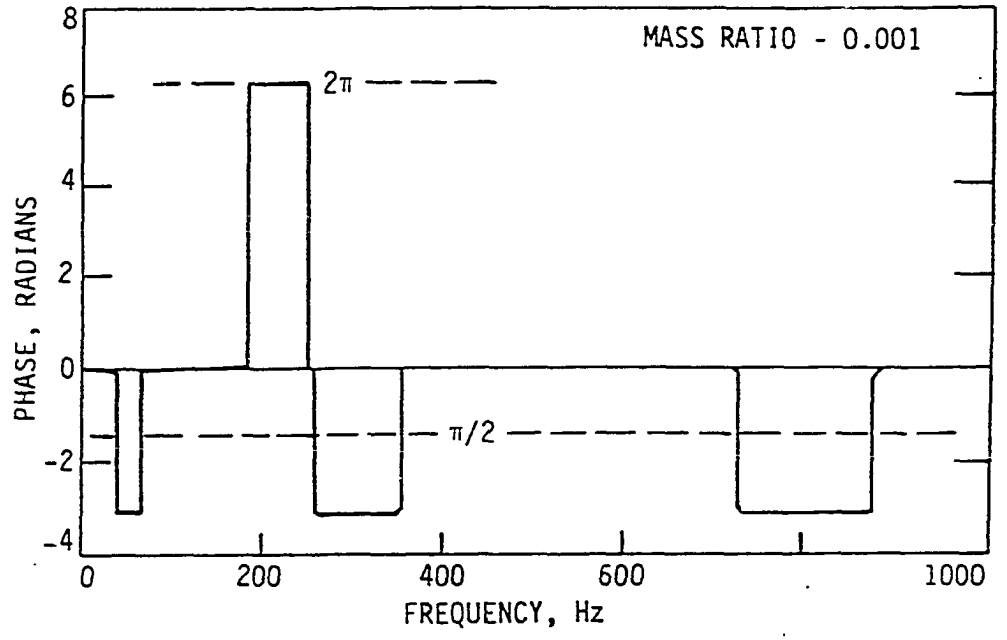

(a)

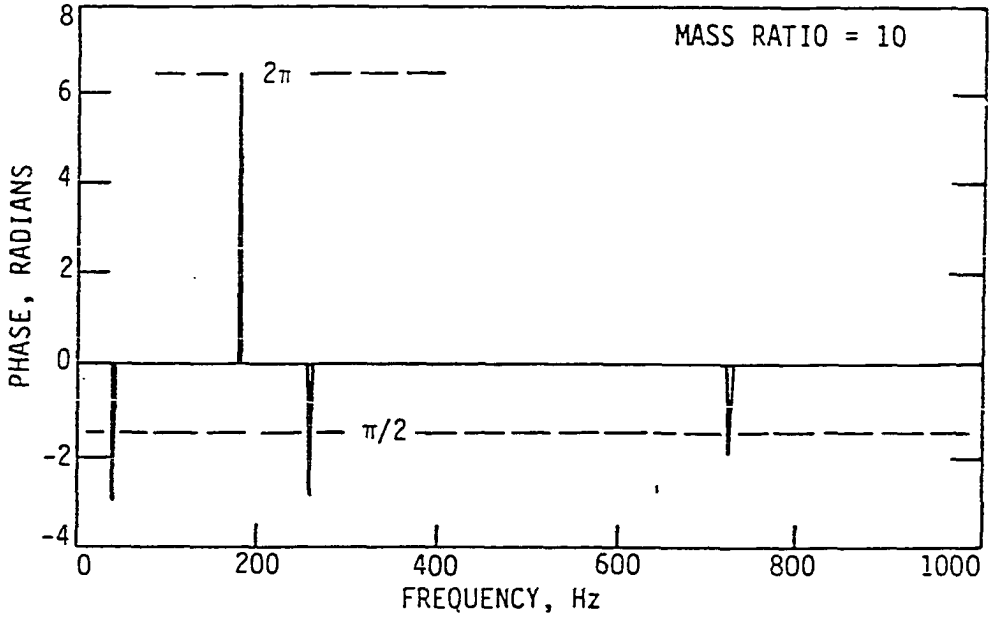

(b)

Fig. 13. Phase angle vs frequency for mass ratios of (a) 0.001; (b) 10.0

CHAPTER IV. TEST PROCEDURES AND RESULTS

Tests were performed using the new test method with two data acquisition techniques. The first was a "quick and dirty" approach which was used to determine if the new method was a viable method. Once it was shown that the new method had promise, a more sophisticated data acquisition technique was developed and employed. Most of the data were gathered using the more sophisticated technique so it will be discussed in detail. However, a brief review of the "quick and dirty" method is instructive and will be discussed first.

The RMS Method

Preliminary tests using the new method were run on a beam specimen of 2024-T351 aluminum. These tests were run to determine the viability of the new test method. The aluminum specimen was chosen because it is known to be a linear material with damping accurately predicted by the Zener Thermal Relaxation Theory, and its low damping establishes the threshold of the measurement technique.

Instrumentation

The instrumentation used for the RMS method was selected for its availability, sensitivity, and speed of data acquisition. In general, availability was of the greatest concern since the RMS tests were performed only to check the test method viability.

The primary quantities to be measured during the testing were the driving force and the driving point acceleration. The acceleration was measured conveniently using a piezoelectric accelerometer internally mounted to the exciter head. The driving force was measured by a Kistler model 912 piezoelectric force transducer. The output of each transducer was fed, through a charge amplifier, to a Keithley model 179 true RMS digital voltmeter. The instrumentation for the RMS tests is shown in Fig. 14.

Careful transducer calibration was required to obtain accurate results. The accelerometer was dynamically calibrated by comparing its output for sinusoidal motion to the output for an attached calibration standard accelerometer, traceable to the National Bureau of Standards. Once the shaker-mounted accelerometer had been calibrated, it could be used to calibrate the force transducer.

The force transducer was calibrated in the manner recommended by Dally, Riley, and McConnell [59] which determines both the sensitivity and the seismic mass of the force transducer. In this method, the force transducer is axially attached to the shaker and excited by sinusoidal motion of the vibration exciter. A series of small masses are attached to the force transducer and excited. Since the acceleration is known from the accelerometer in the shaker head, the actual force measured by the force transducer may be determined from Newton's second law where the mass is the sum of the added

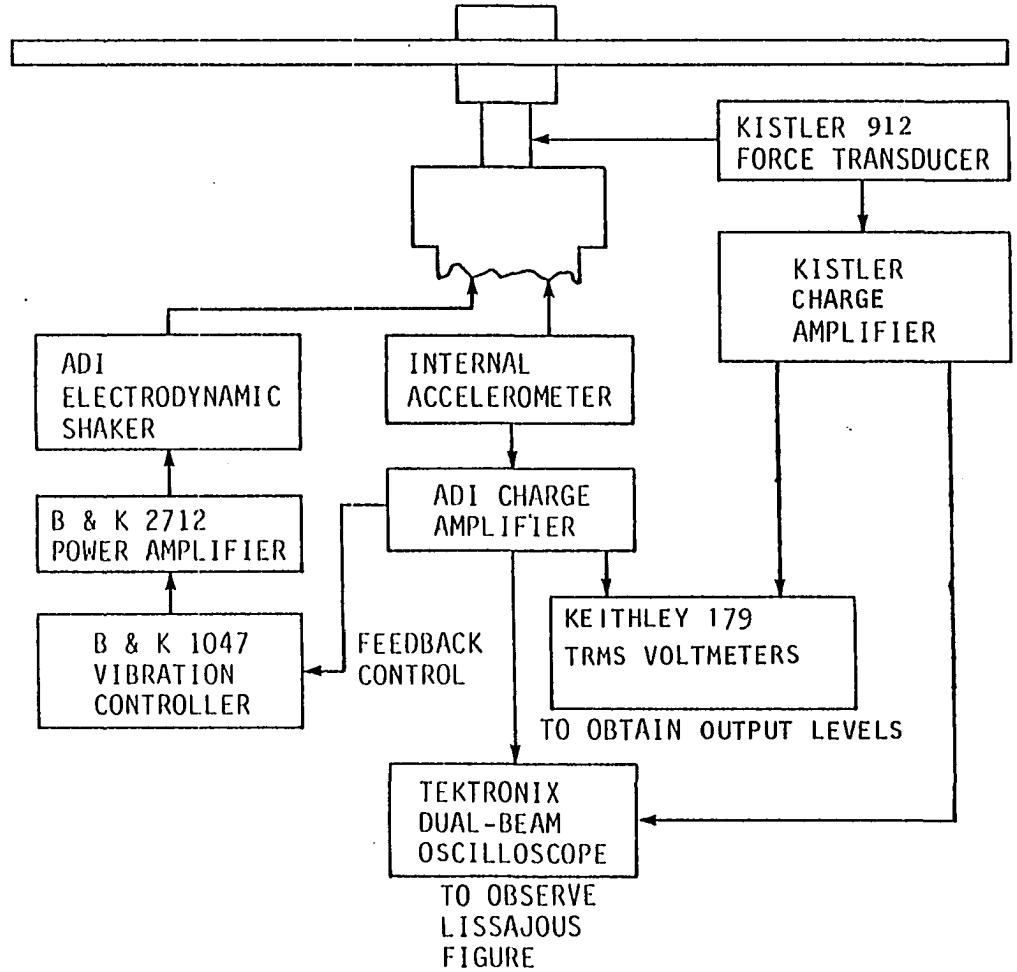

Fig. 14. Block diagram of instrumentation for tests using the RMS method

mass and the transducer seismic mass. The sensitivity and seismic mass are easily extracted by plotting the weight of the added mass versus the ratio of output voltages between the force transducer and the accelerometer. The data should plot as a straight line with the y-axis intercept at minus the weight of the seismic mass and the slope equal to the ratio of the acceleration sensitivity to the force sensitivity. This procedure produces a quick and accurate calibration of the force transducer.

The seismic mass of the force transducer was added to the masses of the clamping blocks, screws, and the beam portion contained between the blocks to give the base mass of the test specimen. All masses other than the transducer seismic mass were determined using a Mettler analytical balance accurate to 0.01 gram. These masses were then used in the characteristic and loss factor equations, Eqs. (26) and (55).

Procedure

The tests were run on the aluminum specimen, held in place with aluminum clamping blocks and steel screws. The aluminum blocks were chosen due to their light weight, which has already been shown to improve the sensitivity of the test method.

The tests were run for the first two resonant modes of the test system. The resonant condition was determined by observing the lissajous figure of the force and acceleration

signals as the phase shift between the signals went to 90^{o}. When the phase shift was approximately 90^{o}, the force signal was closely monitored with the test condition being set when the force signal was a minimum. In practice, it was difficult to observe the phase shift due to the measurement noise and frequency components at other than the driving frequency in the force signal. Thus, the primary method for setting the test condition was the minimization of the force signal.

For each resonant mode, tests were run at a series of amplitudes. For each amplitude, once resonance was established, the driving force and driving point acceleration were measured and used in Eq. (55) to determine the loss factor. Since aluminum is known to be a linear material, the material damping loss factor was constant with amplitude; and any amplitude dependence was due to external damping or system nonlinearities. The test specimen was a long thin beam, with dimensions given in Table 2, and was tested in ambient air. Therefore, air damping was expected to be significant.

Table 2. Specimen dimensions for RMS method tests

Material	Length, in.	Width, in.	Thickness, in.	Beam Mass, $lb\text{-}s^2/in.$	Base Mass, $lb\text{-}s^2/in.$
Aluminum 2024-T351	9.83	0.698	0.1225	$4.222(10^{-4})$	$1.290(10^{-4})$

Results

Data were gathered for a variety of amplitudes at the first two resonant modes of the test system. A typical plot of the loss factor versus acceleration amplitude is shown in Fig. 15. The nature of the data shown in this figure brings up some issues which must be addressed. The analysis of the data may be explained in the following matter.

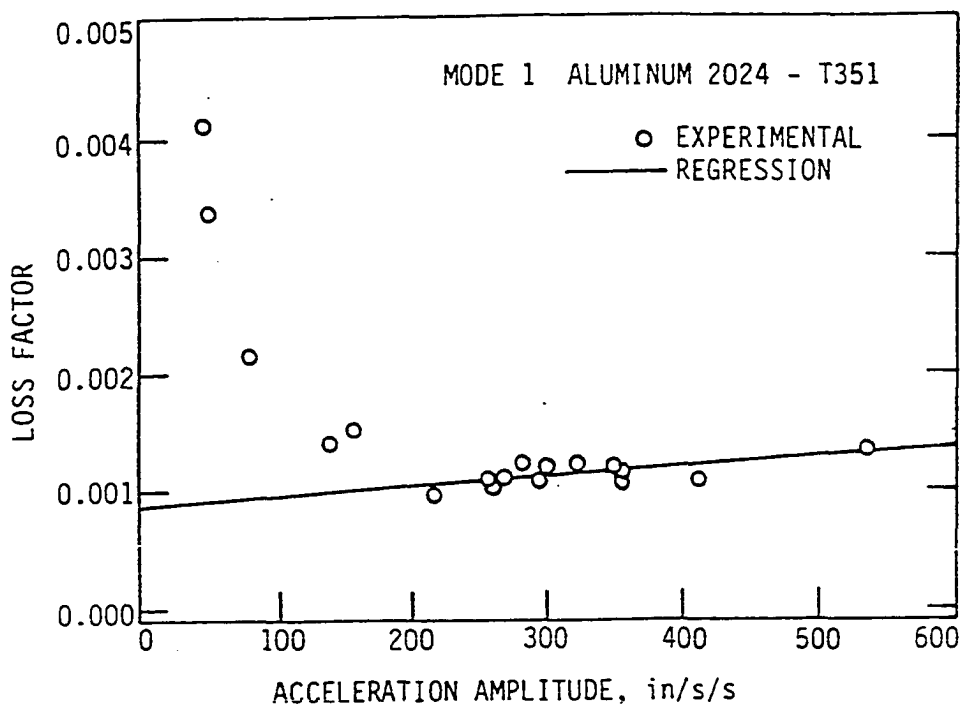

Fig. 15. Typical loss factor vs acceleration amplitude curve with extrapolation to zero amplitude to eliminate air damping

The data are seen to decrease linearly with amplitude until a threshold level is reached. Below this level the data

increase in a manner approximately inverse to the acceleration amplitude. These two effects may be explained by considering two different aspects of the vibrating system.

Consider first the inverse relationship between the loss factor and the acceleration amplitude seen at low amplitudes. From Eq. (55) it can be seen that the loss factor is directly proportional to the driving force amplitude and inversely proportional to the acceleration amplitude. The Kistler 912 force transducer had a listed threshold of 0.002 pounds force. As the acceleration amplitude decreased, the force signal decreased until it reached the noise floor of the force transducer-charge amplifier system. However, the acceleration signal was still well above its noise floor so its amplitude was accurately determined. Thus, as the acceleration was decreased to below the force transducer noise threshold, the decreasing acceleration was accurately tracked while the force signal remained nearly constant, owing to the noise level. Therefore, the dramatic increase in the loss factor with decreasing acceleration amplitude is merely the effect of noise in the measurement system combined with the need to make very low level measurements.

Next, consider the linear increase in the loss factor with increasing acceleration amplitude for amplitudes above the threshold. Baker et al. [14] and Rogers [57] have shown that the air damping loss factor generally shows a linear increase with amplitude. Since the tests were run in ambient

air, it seemed reasonable to assume that the linear increase with amplitude was due to air damping. Thus, a least squares linear regression was performed on the data above the threshold level and was extrapolated to zero amplitude to remove the effects of air from the material damping.

The loss factors obtained from the extrapolations to zero amplitude for the first two resonant modes were compared to the loss factors predicted by the Zener theory. A comparison of these is shown in Fig. 16. It is clear that the results from the RMS procedure of the new test method fall quite close to the predicted values. Thus, the new method was seen to provide sufficient promise to be pursued further.

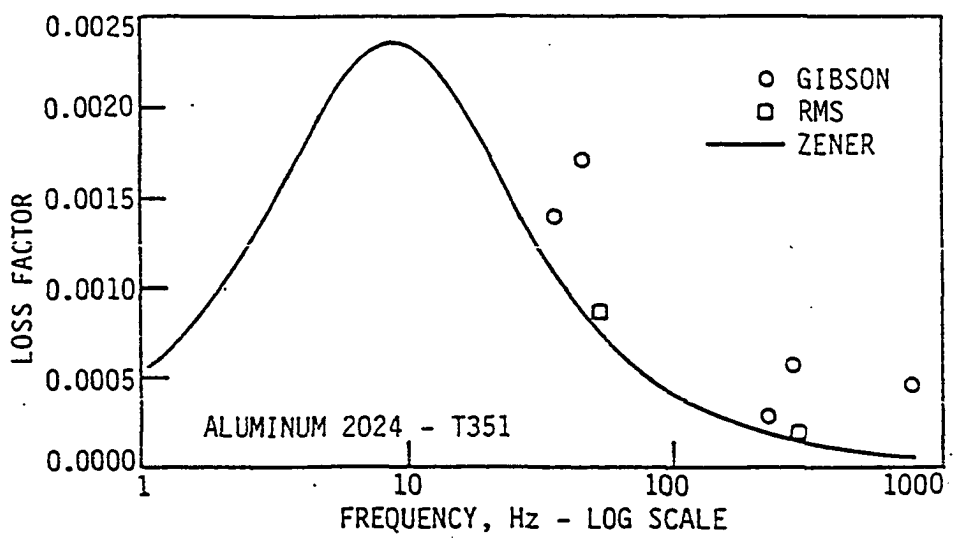

Fig. 16. Comparison of RMS method results with Zener Theory

The Frequency Analysis Method

The preliminary results from the new test method were encouraging so a more sophisticated data acquisition and analysis method was devised. The primary goals of the improvements were to improve the sensitivity of the force measurement and to investigate the frequency components present. Thus, changes in the test instrumentation and procedure were required.

Instrumentation

Several changes in the test instrumentation were made to improve the sensitivity of the force measurement. To improve the transducer sensitivity, a new force transducer was obtained. The new transducer, a Kistler model 9712A5 Piezotron, offered an order of magnitude increase in sensitivity with a listed threshold of 0.0002 pounds. In addition to the improved sensitivity, the piezotron style piezoelectric transducers contain an internal voltage amplifier. This characteristic significantly reduces the noise generated due to the cables used to connect the transducer to the remainder of the measurement system. The fact that an external charge amplifier is not required allows battery powered voltage amplifiers to be used. Thus, with no line voltage powered amplifiers, the power line noise problems commonly encountered in measurements are eliminated.

The new force transducer was calibrated using the previously described calibration method to yield its sensitivity and seismic mass. The exciter head internal accelerometer was again used and was calibrated with the calibration standard accelerometer.

To further amplify the force signal and to allow a more accurate determination of the -90^{o} phase shift at resonance, a battery powered amplifier and bandpass filter were designed using the methods of Hilburn and Johnson [61]. The amplifier, shown in Fig. 17, was designed to be battery powered and to have a voltage gain of about 10. The output of the amplifier was directed into the bandpass filter shown in Fig. 18. The resistors R1, R2, and R3 were replaced with potentiometers so that the filter characteristics could be varied as needed. The capacitors were placed on a plug-in board so they could be easily changed, thus allowing for an almost unlimited adjustment of the filter's center frequency. The center frequency, filter gain, and amplifier gain were set using a pure sinusoid of known amplitude at the resonant frequency of each mode just prior to testing at that mode.

The last major improvement to the test system instrumentation was the use of a Norland 3001 Digital Processing Oscilloscope to perform the frequency analysis of the force and acceleration signals. This addition allowed the investigation of the various frequency components contained within the output signals. The acceleration signal was fed from a charge

amplifier to the Norland while the force signal was amplified first in the battery powered amplifier and then sent to the Norland. The output from the filter was used only to give a clearer lissajous pattern and help establish the resonant condition. The instrumentation used for the frequency analysis tests is shown in Fig. 19.

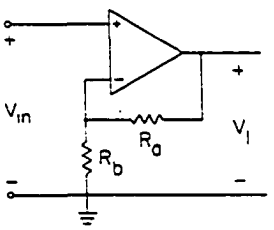

Fig. 17. Schematic of a voltage-controlled voltage source type amplifier (from Hilburn and Johnson [61])

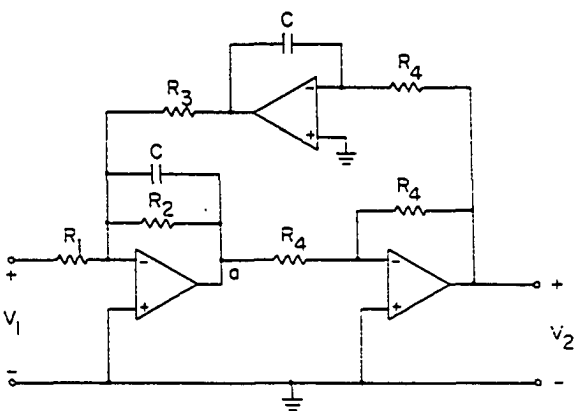

Fig. 18. Schematic of a second-order biquad band-pass filter (from Hilburn and Johnson [61])

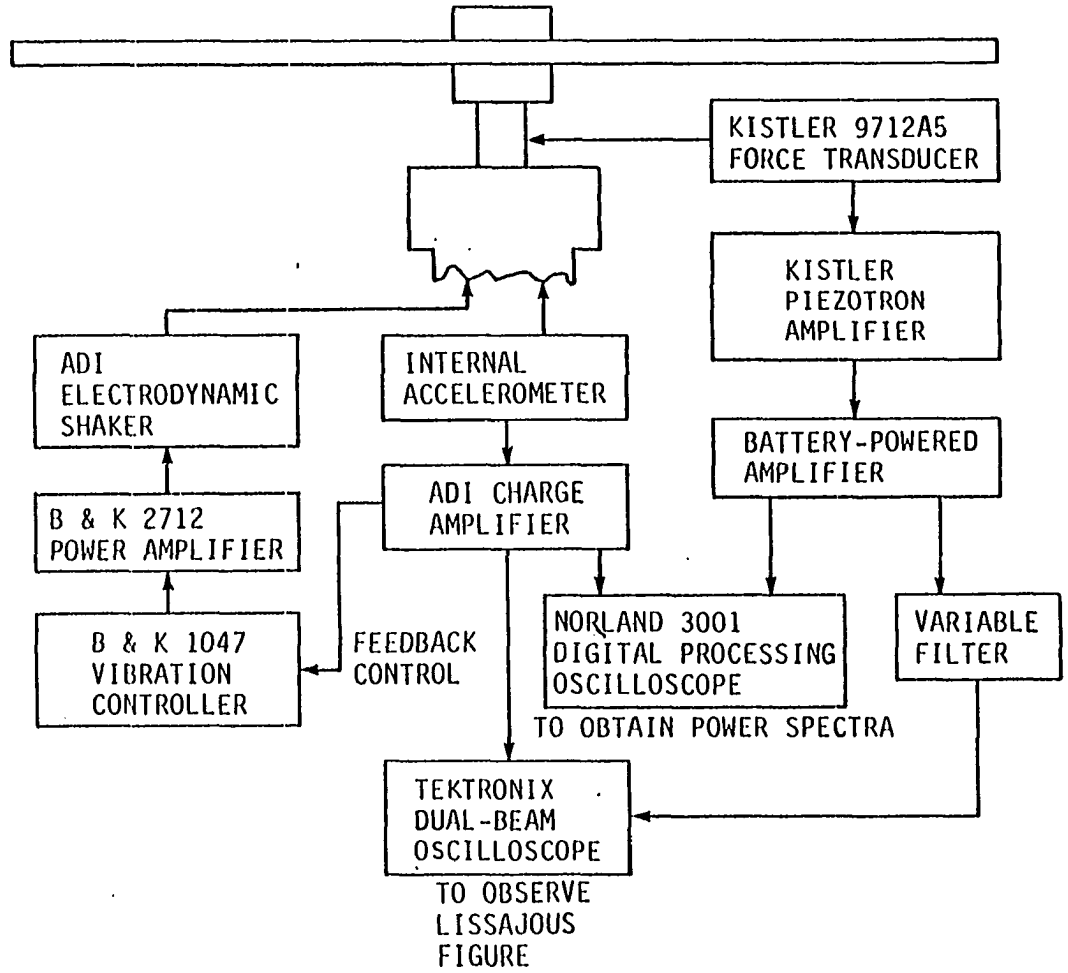

Fig. 19. Block diagram of instrumentation for tests using the frequency analysis method

Procedure

The tests were performed on aluminum and Model-Tech specimens, excited in their first three resonant modes. The dimensions of the test specimens are given in Table 3. For the aluminum specimen, clamping blocks of aluminum and steel were used to investigate the effect of clamp stiffness on the damping measurements. This caused the mass ratio for the aluminum beam tests to range from 0.3 to 0.6. The Model-Tech specimen was tested with aluminum clamping blocks, giving a mass ratio of 0.7. The tests were run at a series of amplitudes in ambient air and at reduced pressure. The reduced pressure tests were conducted in a chamber constructed from 12 inch PVC water main pipes donated by the City of Ames, Public Works Department. The construction of the chamber was performed by the Iowa State University Engineering Research Institute Machine Shop. The barometric pressure was measured, and a U-tube mercury manometer was used to determine the pressure inside the chamber. The vacuum pump used to evacuate the chamber was shut off except for tests below 100 mm Hg where the pump ran continuously.

As in the RMS tests, the test condition was set by getting near resonance with the lissajous technique and then adjusting the frequency until a minimum in the driving force was located. In this case the lissajous technique provided a much faster approach to resonance than before, due to the filtering of the force signal.

Table 3. Dimensions and frequencies for tests using the frequency analysis method

Material	Length (in.)	Width (in.)	Thickness (in.)	Frequency, Hz Mode 1	Mode 1	Mode 3
Aluminum	9.83	0.698	0.1225	50.9	291	753
Model-Tech	9.83	0.705	0.124	18.3	106.5	286.8

Once a resonant condition was obtained, the data acquisition was performed by the Norland oscilloscope. A program, listed in Appendix A, was run which gathered and analyzed the data. The program first acquired and stored a lengthy record of the force and acceleration signals. Shorter segments of these records were then analyzed.

The analysis consisted of, first, obtaining the power spectra of the force and acceleration signals. These power spectra showed spikes for the discrete frequency components making up the signals. An integration algorithm provided the area under each peak which has been shown by Bendat and Piersol [62] to be the mean square of the signal for that frequency component. The RMS values of the frequency components were determined by taking the square root of these mean square values. The RMS values obtained in this manner were

averaged for four data segments to help reduce noise and random error.

Aluminum test results

Consider first the results obtained from the tests of the aluminum specimen. A typical power spectrum for the acceleration signal from a test run in ambient air, p = 727 mm Hg, is shown in Fig. 20. This shows that the acceleration was essentially a pure sinusoid at the resonant driving frequency. The corresponding force power spectrum shown in Fig. 21, however, shows strong contributions from the driving frequency component (the first frequency component) and from several higher harmonic frequencies (the second, third, and fifth frequency components). These frequency components are evidence of several phenomena acting on the beam which should be considered individually.

The material damping, as predicted by the Zener theory, occurs at the driving frequency and not at any of the harmonics. This is because the strains causing the material damping occur only at the driving frequency. If the input motion contained more than one frequency component, then the material damping would be associated with all driving frequency components, as noted by Plunkett and Sax [53]. However, if the driving frequency component of the force and acceleration signals is considered, any contamination from higher harmonic should be avoided. Thus, to accurately assess

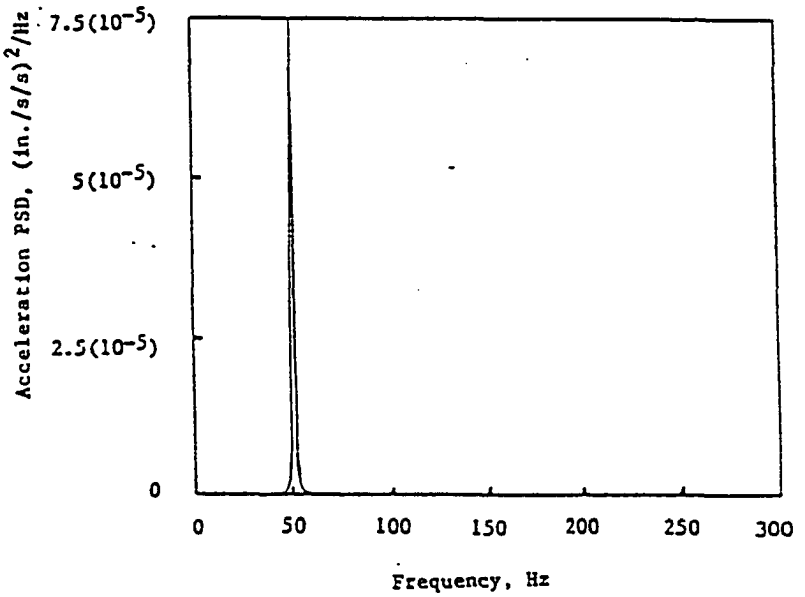

Fig. 20. Power spectrum of acceleration signal for the aluminum specimen in mode 1, ambient air using the new method

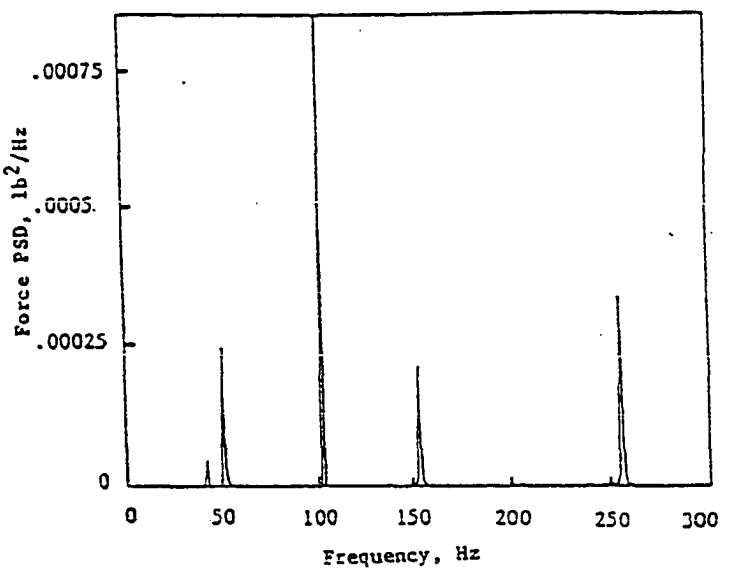

Fig. 21. Power Spectrum of force signal for the aluminum specimen in mode 1, ambient air using the new method

the material damping, analysis must be limited to the driving frequency components.

The effect of air damping on a vibrating beam has been considered by Baker et al. [14] and Stevens and Scavullo [44] who indicate that air damping is a drag effect proportional to velocity at low amplitudes and proportional to velocity squared at large amplitudes. Modi and Poon [63] and St. Hilaire and Vaidya [64] indicate that these drag forces include components at the driving frequency and at the second harmonic frequency. Thus, air damping was expected to effect the driving, or first, frequency component and the second frequency component.

To investigate the contribution of air damping to the system response, tests were run in a reduced pressure chamber. The power spectrum from the force signal obtained at an air pressure of 100 mm Hg for the same mode and acceleration amplitude as that for Fig. 21 is shown in Fig. 22. The first and second frequency components are seen to decrease significantly (15%-20%) when the air pressure is reduced. Thus, as expected, air damping has a significant effect on the first and second frequency components of the force signal due to the nonlinear drag effects.

It is of interest to note while comparing Figs. 21 and 22 that the third and fifth frequency components increase slightly with decreasing air pressure. This can be explained by considering the nonlinear effects acting in the system. As

the air is removed, the total damping in the system decreases; and, for a given base excitation, the beam motion tends to increase. The increased beam motion accentuates the nonlinear effects, causing the slight increase in these frequency components.

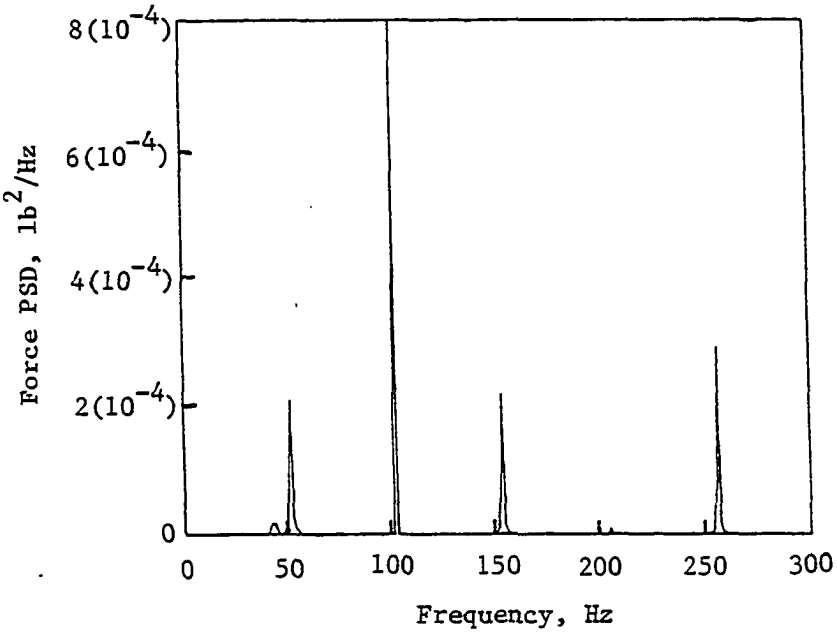

Fig. 22. Power spectrum of force signal for the aluminum specimen in mode 1, 100 mm Hg air pressure

These nonlinear effects arise from a variety of sources. The contact between the clamping blocks and the beam specimen leads to two nonlinear effects on the system. First, the clamping blocks, which were assumed to be flat and to rigidly restrain the beam motion, will have some curvature near the

edges. Thus, as amplitude increases, the effective boundary condition at the edge of the clamping block changes. The boundary condition becomes stiffer with increasing amplitude giving a "hardening spring" effect which has been shown to produce frequency components at the third and fifth harmonic frequencies. The hardening spring characteristic may be visualized by considering a cantilever beam clamped by two cylindrical surfaces. As the beam deflection increases, the beam comes into contact with the clamping surfaces farther and farther away from the point of fixity. Thus, for larger amplitudes, the effective length of the beam is reduced, and the stiffness of the system is increased.

The second nonlinear effect associated with the clamping blocks is friction damping between the beam and the blocks. The friction damping would occur twice during each cycle--when the beam slides against the top block and when the beam slides against the bottom block. Thus, friction damping was expected to contribute to the second frequency component. This contribution is clearly illustrated in Figs. 23 and 24, which show the effect of clamping tightness on the force signal. The second frequency component is very large in the loosely clamped condition, but it is significantly reduced by tightening the clamping screws. This is because when loose, the beam and clamping blocks have greater freedom for relative motion and, therefore, greater friction damping occurs. When tightly clamped, the relative motion is restricted and friction damping is reduced.

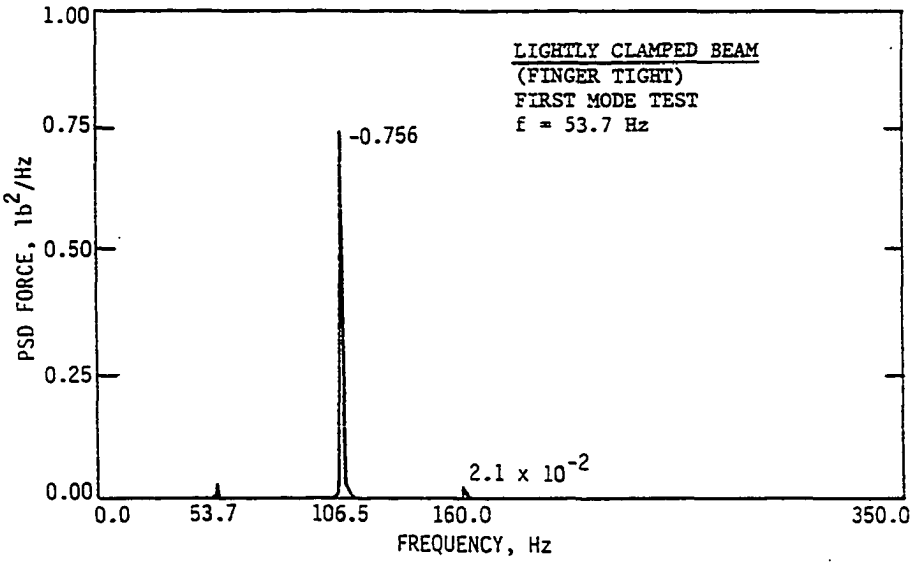

Fig. 23. Power spectrum of force signal for the aluminum specimen in mode 1, loosely clamped

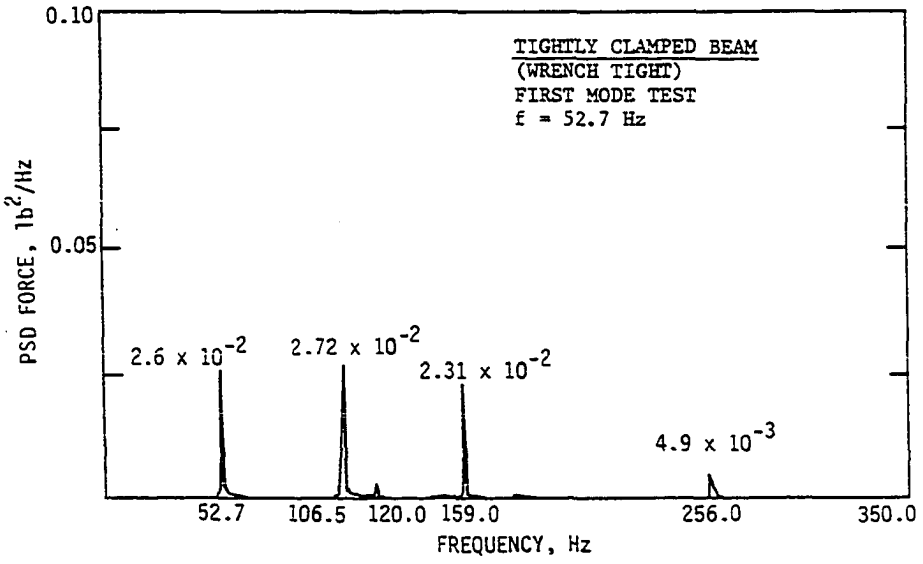

Fig. 24. Power spectrum of force signal for the aluminum specimen in mode 1, tightly clamped

Another path by which nonlinearity may effect the test system is through nonlinear motion of the exciter head. The vibration exciter is designed to produce output motion directly related to the input electrical signal. However, due to the dynamics of the moving exciter head, higher harmonic frequencies are often present. These higher harmonic components of the exciter motion are usually quite small when compared to the driving frequency component. However, even a small component in the acceleration signal can lead to large force components since the higher harmonics are not at resonant conditions. Therefore, the force signal generated by a higher harmonic of the resonant driving frequency includes contributions from the system stiffness, inertia, and damping. Even though the power spectrum of the acceleration signal shown in Fig. 20 does not appear to indicate any frequency components at other than the driving frequency, a point-by-point inspection located a very small component at the second harmonic frequency. This component was quite small, but it was still sufficient to explain a large portion of the second frequency component of the force signal.

The effect of amplitude on the material damping was investigated by running a series of tests at different amplitudes for each resonant mode. A plot of the loss factor as determined from the first (or driving) frequency components of the force and acceleration signals versus the acceleration amplitude for mode 1 is shown in Fig. 25. This plot includes

data from three tests. Data set 1 was obtained using aluminum clamping blocks while the other sets were obtained using steel clamping blocks. Since the data plot together, the clamping blocks do not have a significant effect on the results. The curve shows a noise floor-like effect, similar to that noted for the RMS tests, before flattening out to a loss factor of about 0.0008. The noise floor type of behavior was evident only for the mode 1 test on the aluminum specimen. Tests on modes 2 and 3 for the aluminum specimen showed that the loss factor was independent of amplitude. A typical plot of loss factor versus amplitude for the second mode is shown in Fig. 26. It appears that reducing the air pressure increases the damping. This effect was caused by the vacuum pump which could not be adequately isolated from the test chamber and introduced a frequency component at the second mode resonant frequency of the aluminum specimen. Thus, the apparent increase in the loss factor with reduced air pressure is an artifact of the test system and not attributable to either air or specimen properties.

The material damping was expected to be independent of amplitude since aluminum is a linear material. The linear material damping is shown in Figs. 25 and 26 at least once a threshold level has been achieved.

Air damping was expected to introduce force contributions to the first and second frequency components which would change from linear to quadritic functions of amplitude. In

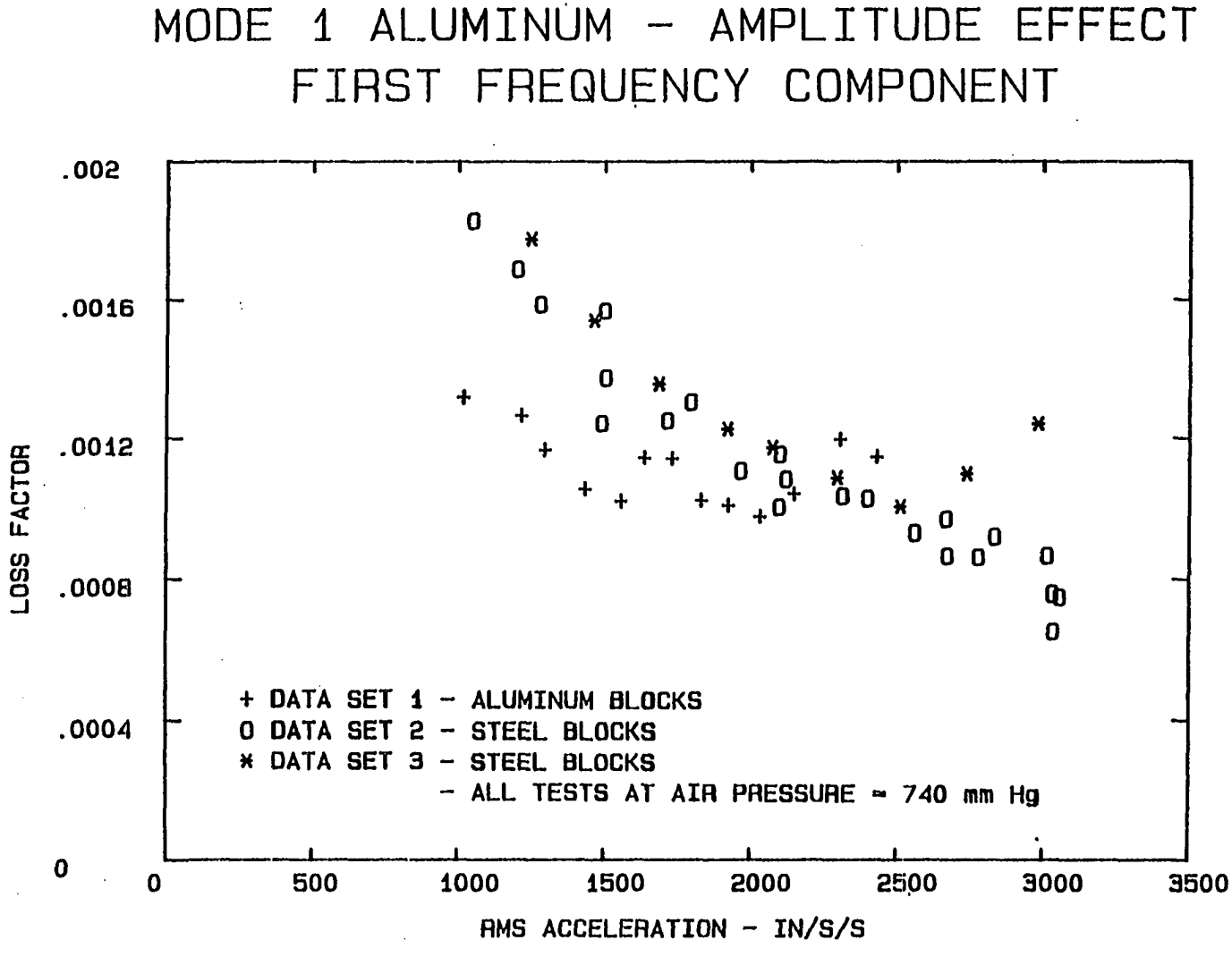

Fig. 25. Loss factor vs acceleration amplitude, mode 1, aluminum, first frequency component

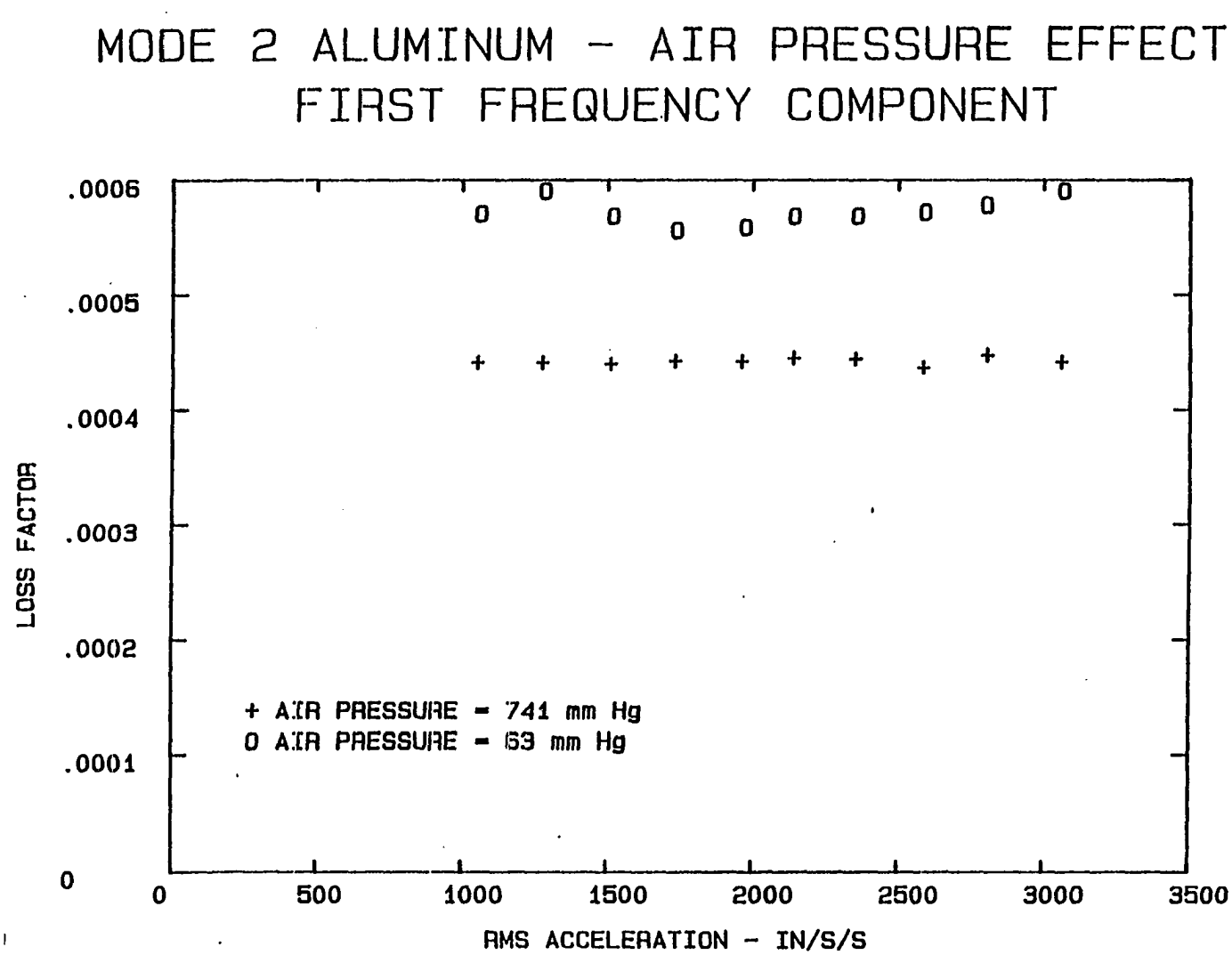

Fig. 26. Loss factor vs acceleration amplitude, mode 2, aluminum, first frequency component

addition, friction damping was expected to introduce a contribution to the second frequency component of the force which Plunkett [28] has shown to be proportional to amplitude cubed. Therefore, the second frequency component of the force signal was expected to have a significantly nonlinear relationship to the amplitude.

The second frequency component of the force signal is plotted against acceleration amplitude in Fig. 27. This plot shows the expected nonlinear relationship between force and amplitude. The nature of the curve is something between a linear and a quadratic relationship, with the actual exponent being about 1.6. Thus, the second frequency component shows significant influence from nonlinear air and friction damping effects. The behavior shown in Fig. 27 is typical of the nature of the second frequency component of the force signal for all modes of the aluminum specimen.

The effect of air pressure on system damping was studied using the reduced pressure chamber. Data were gathered for three acceleration amplitude levels at a series of pressures, ranging from atmospheric to about 60 mm Hg. The loss factor, calculated from the first frequency component for mode 1, is plotted against air pressure in Fig. 28. It is seen that, for the two lower amplitudes, the loss factor is nearly constant with varying air pressure. However, for the largest amplitude the loss factor varies linearly with pressure until, at the lowest pressure level, the loss factor shows a slight dropoff.

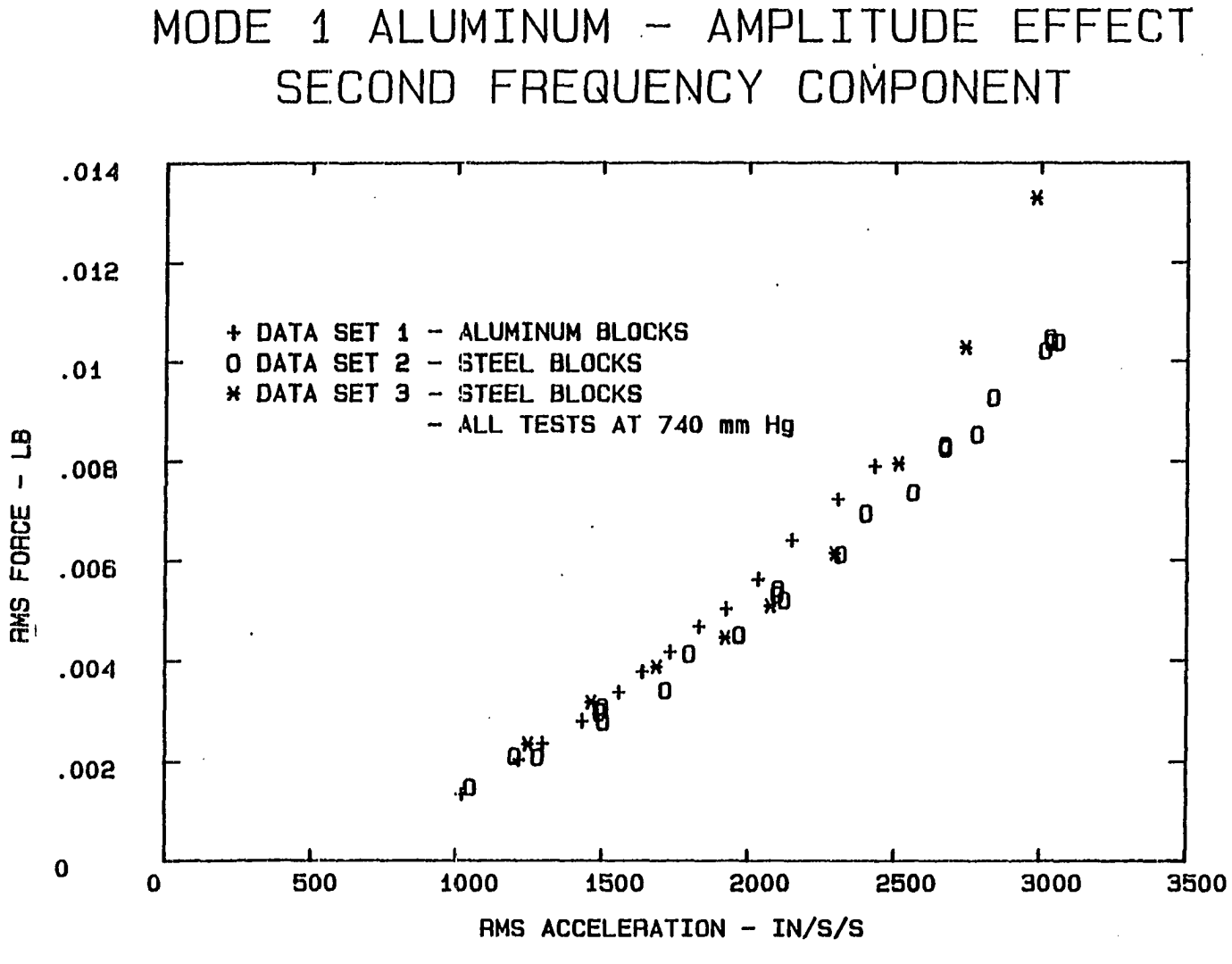

Fig. 27. Force vs acceleration amplitude, mode 1, aluminum, second frequency component

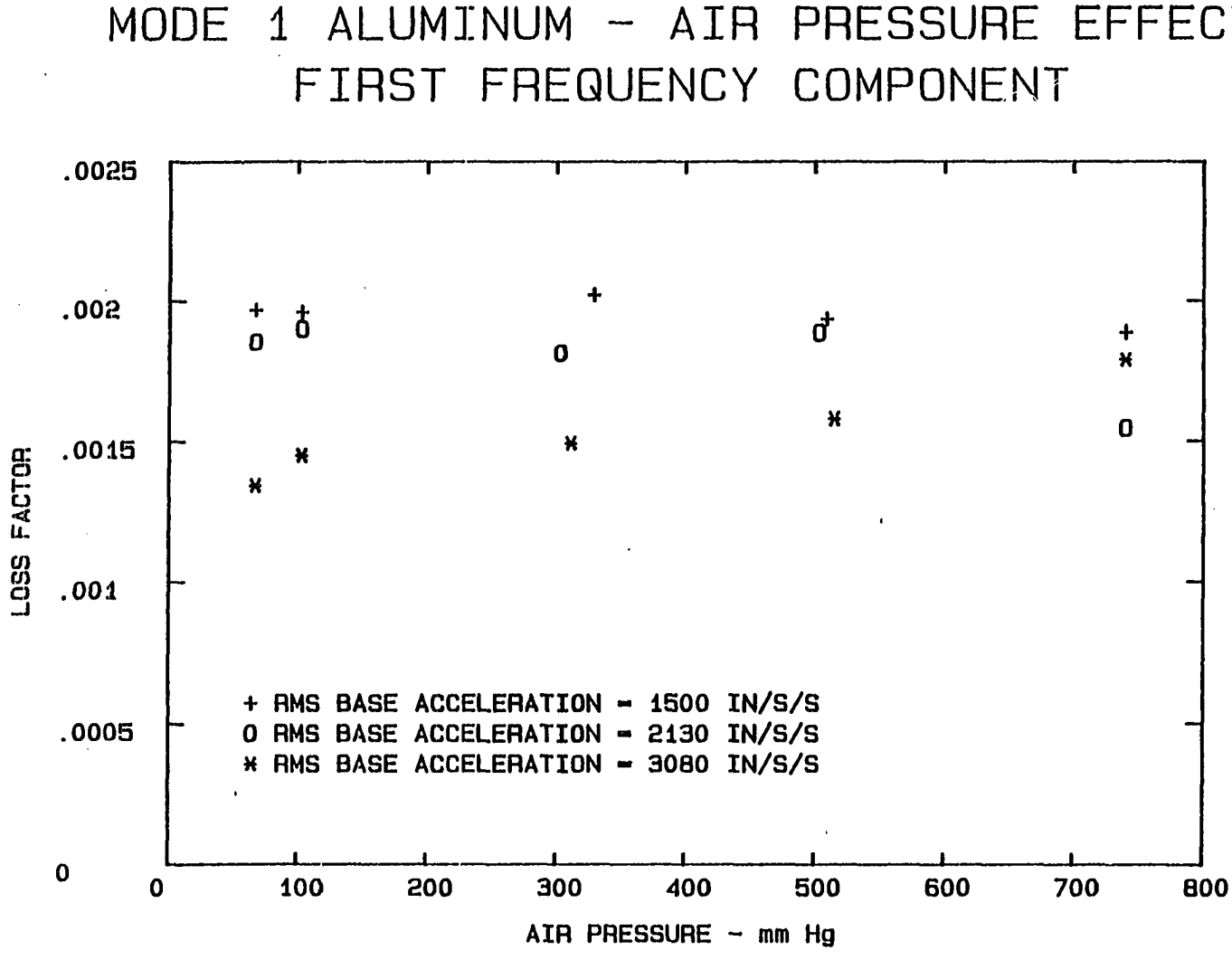

Fig. 28. Loss factor vs air pressure, mode 1, aluminum, first frequency component

The same effect is seen in Fig. 29 where the loss factor calculated from the RMS values of the first three frequency components is plotted against air pressure. This plot includes the air damping contribution from the second frequency component and shows the dropoff for all three amplitudes at the lowest pressure. A much larger dropoff occurred for the Model-Tech material (see Fig. 38).

The linear increase in the loss factor with air pressure was noted by Stevens and Scavullo [44] and is easily explained. Air damping has been shown to be due to a drag effect which is dependent on velocity or velocity squared, and air density. Since air behaves essentially as an ideal gas, the density is directly proportional to the pressure. Hence, the linear relationship between the loss factor and air pressure is seen.

The dropoff phenomenon was also noted by Stevens and Scavullo [44] but is more difficult to satisfactorily explain. However, some insight may be gained from work done on oscillating, concentric spheres by Munson and Douglass [65]. They show that a dramatic flow change occurs over a very small range of values for a dimensionless frequency parameter given by

$$\alpha = R(\omega/\nu)^{1/2} \qquad (61)$$

where

R = a typical dimension,

ω = angular frequency,

ν = kinematic viscosity.

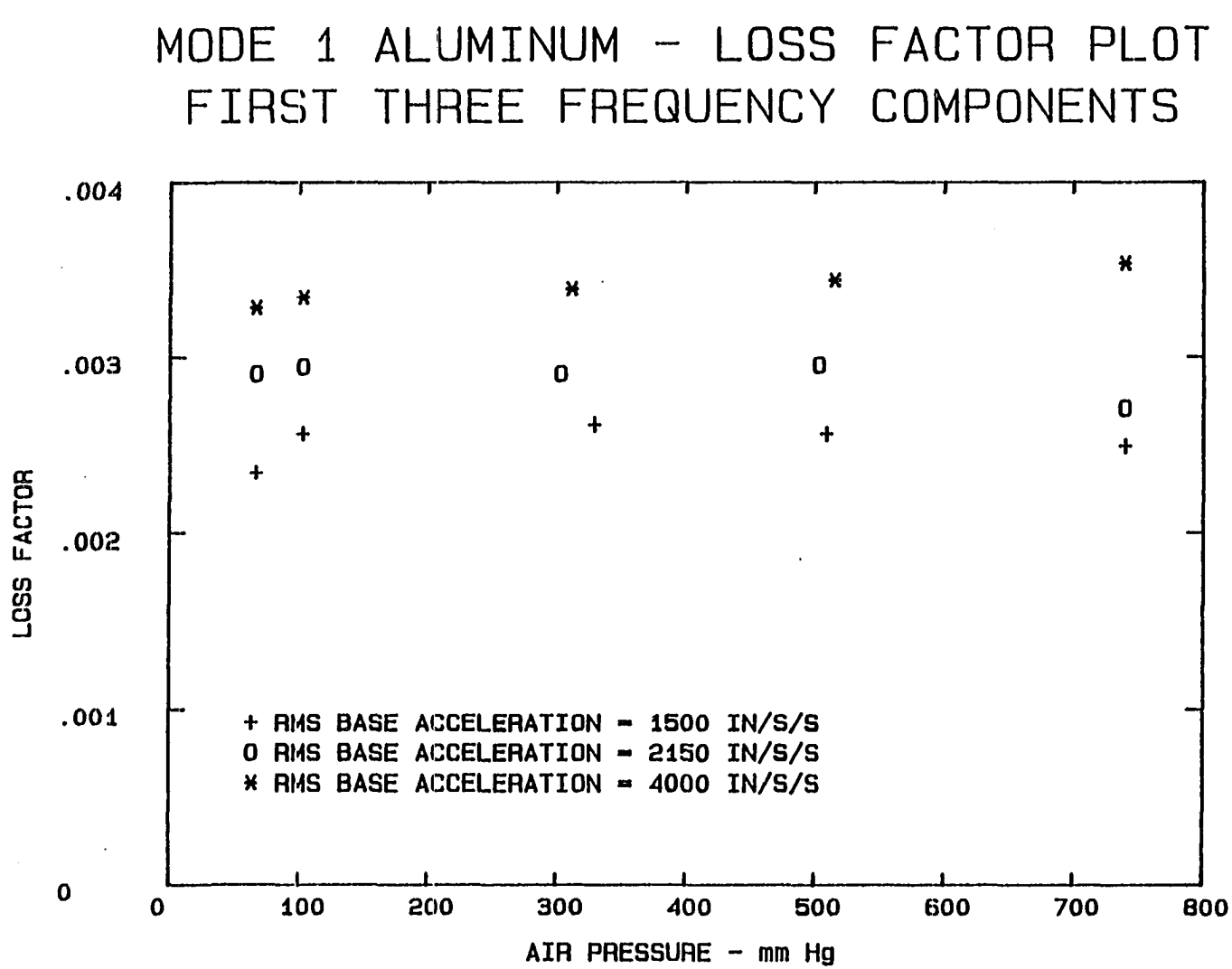

Fig. 29. Loss factor vs air pressure, mode 1, aluminum, first three frequency components

In their case, a distinct flow change occurred when the value of α was in the range $2 < \alpha < 20$, with the precise value at which the flow changed being dependent on other system parameters.

For the current work, if the beam thickness is taken for the typical dimension, the value of α ranges from nearly 15 for the atmospheric test environment to 5 for the lowest pressure level. Thus, it is reasonable to suspect that the sudden dropoff in the loss factor at low pressure was due to a dramatic change in the flow characteristics of the fluid surrounding the beam.

The dropoff phenomena just described were significant for mode 1 but became less pronounced as the mode number increased. This is probably because deflections for the higher modes were much less than for mode 1. However, based only on the current work, a mode shape dependence cannot be ruled out.

The primary reasons for running tests on the aluminum specimen were to qualify the test method with a material whose damping characteristics were known and to set the threshold of the test method. The loss factor for each mode was obtained by averaging the loss factors determined from the first frequency components. Only the values on the "flattened out" portion of the mode 1 curve were used for that value. These loss factors are shown in Fig. 30, along with the Zener Theory curve and the values determined previously using Gibson's method. The results from the new method, in general, lie

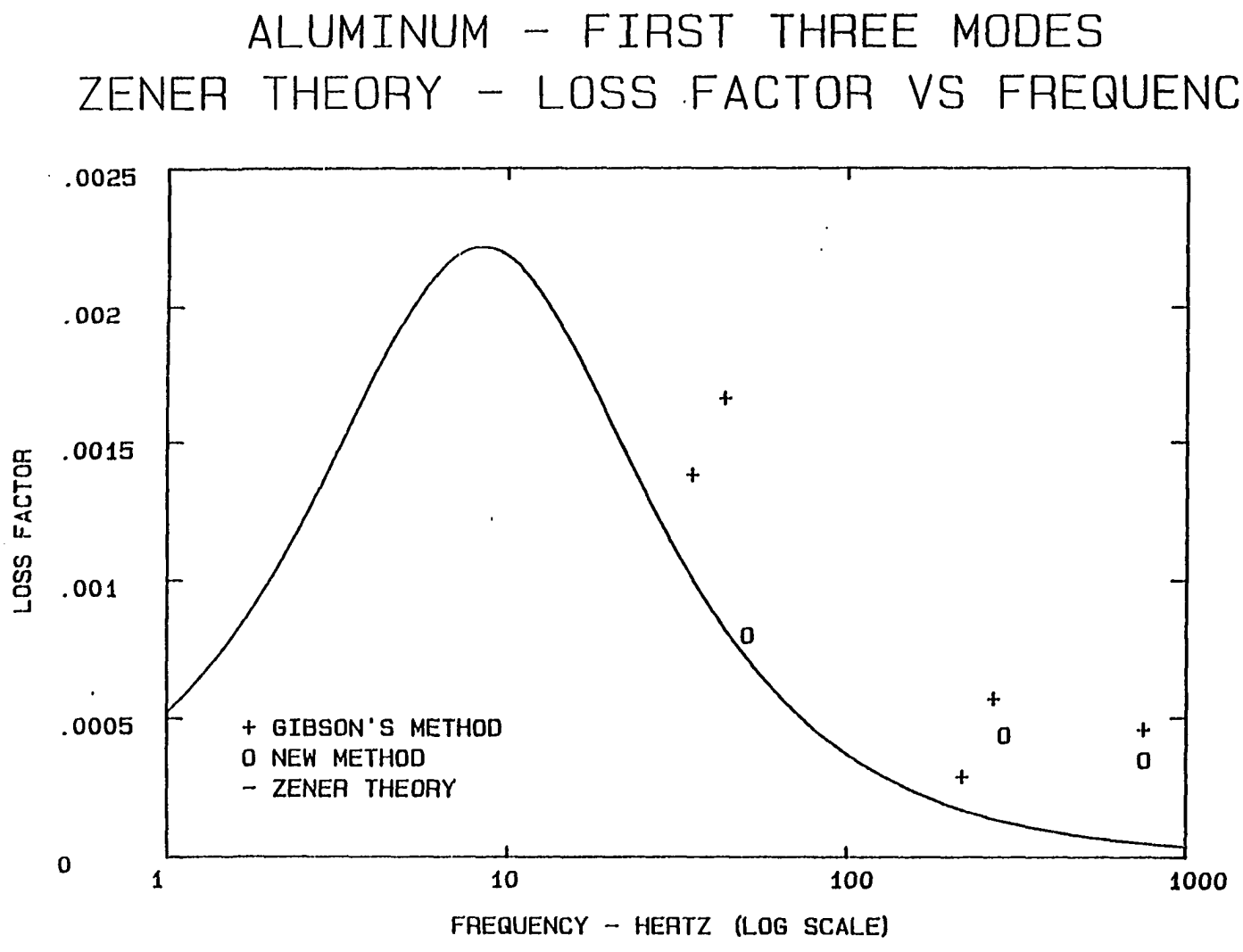

Fig. 30. Loss factor vs frequency, first three modes, aluminum, first frequency component

closer to the Zener theory curve than do those obtained from Gibson's method. Therefore, the new method is seen to give improved results compared to Gibson's method.

Model-Tech test results

The new test method has been shown to be a viable method from the results of the tests on the aluminum specimen, where the damping was predicted from theoretical considerations. Tests were then run on Model-Tech FR-20, an aluminum particle-filled epoxy composite. These tests were run using the frequency analysis approach for the new method. The tests were run for the first three resonant modes, in ambient air and at reduced pressure.

Power spectra of acceleration and force, typical of those seen for modes 2 and 3 for the Model-Tech, are shown in Figs. 31 and 32. It is significant to note that no higher harmonics appear in either the acceleration or force PSD plots. This is because the material damping of Model-Tech is much larger than that of aluminum, and, in this case, the material damping dominates the force signal. The higher harmonics actually are present in the force signal; however, they are so small that they do not appear on the linearly scaled PSD plot.

Consider next Figs. 33 and 34 which show the power spectra of acceleration and force for mode 1. The acceleration signal shows significant components at the driving

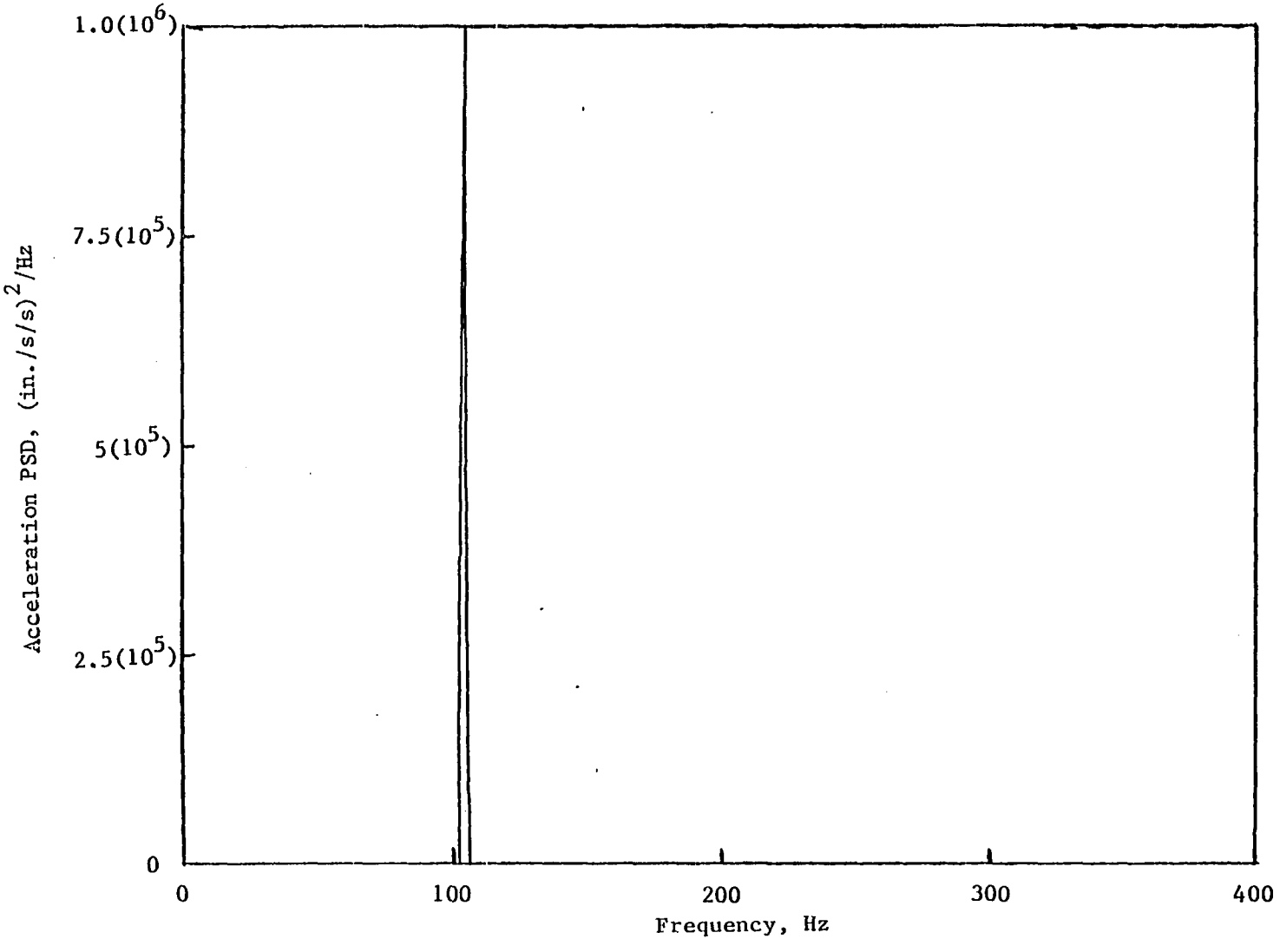

Fig. 31. Power spectrum of acceleration signal for the Model-Tech specimen in mode 2, ambient air

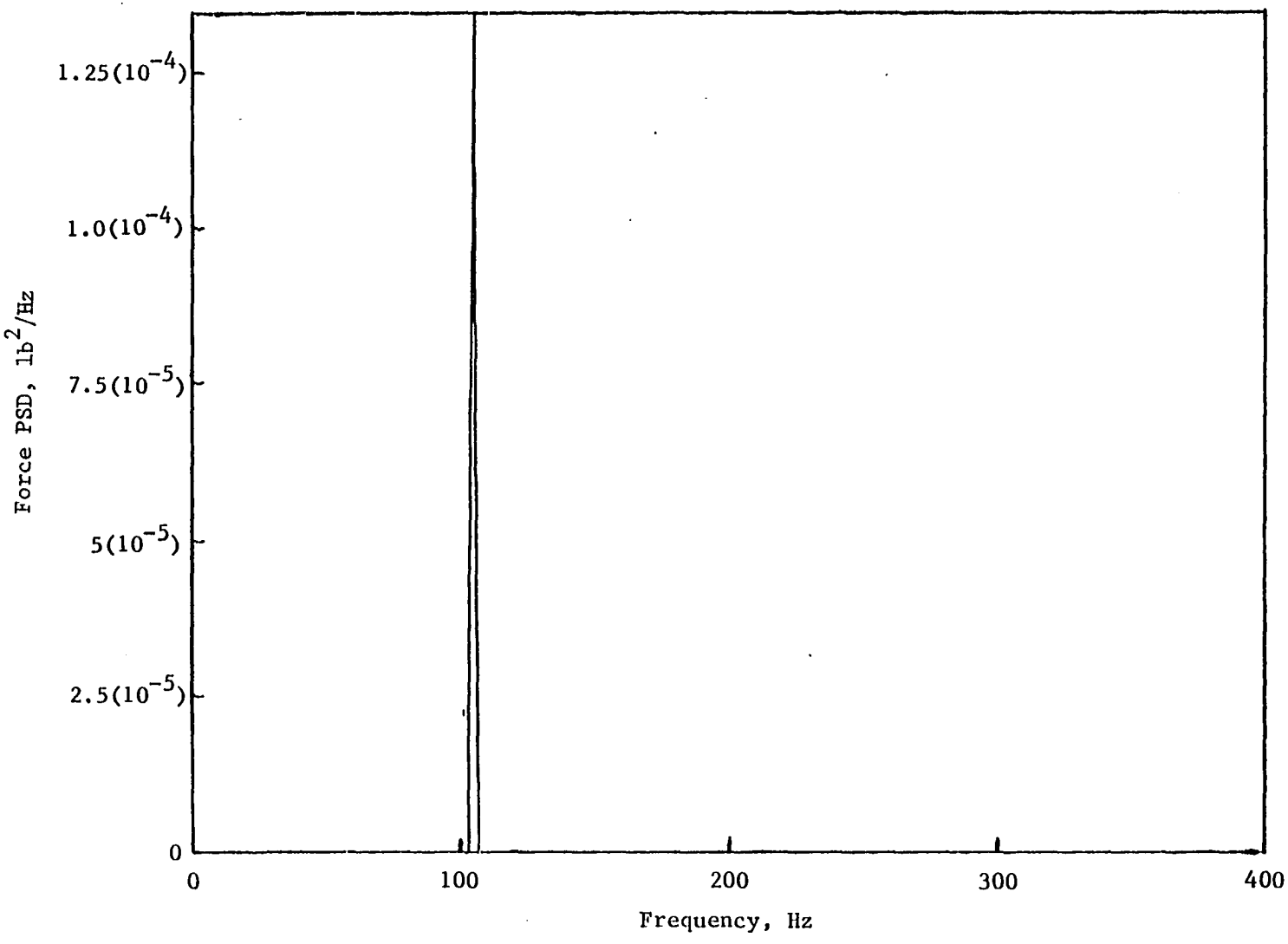

Fig. 32. Power spectrum of force signal for the Model-Tech specimen in mode 2, ambient air

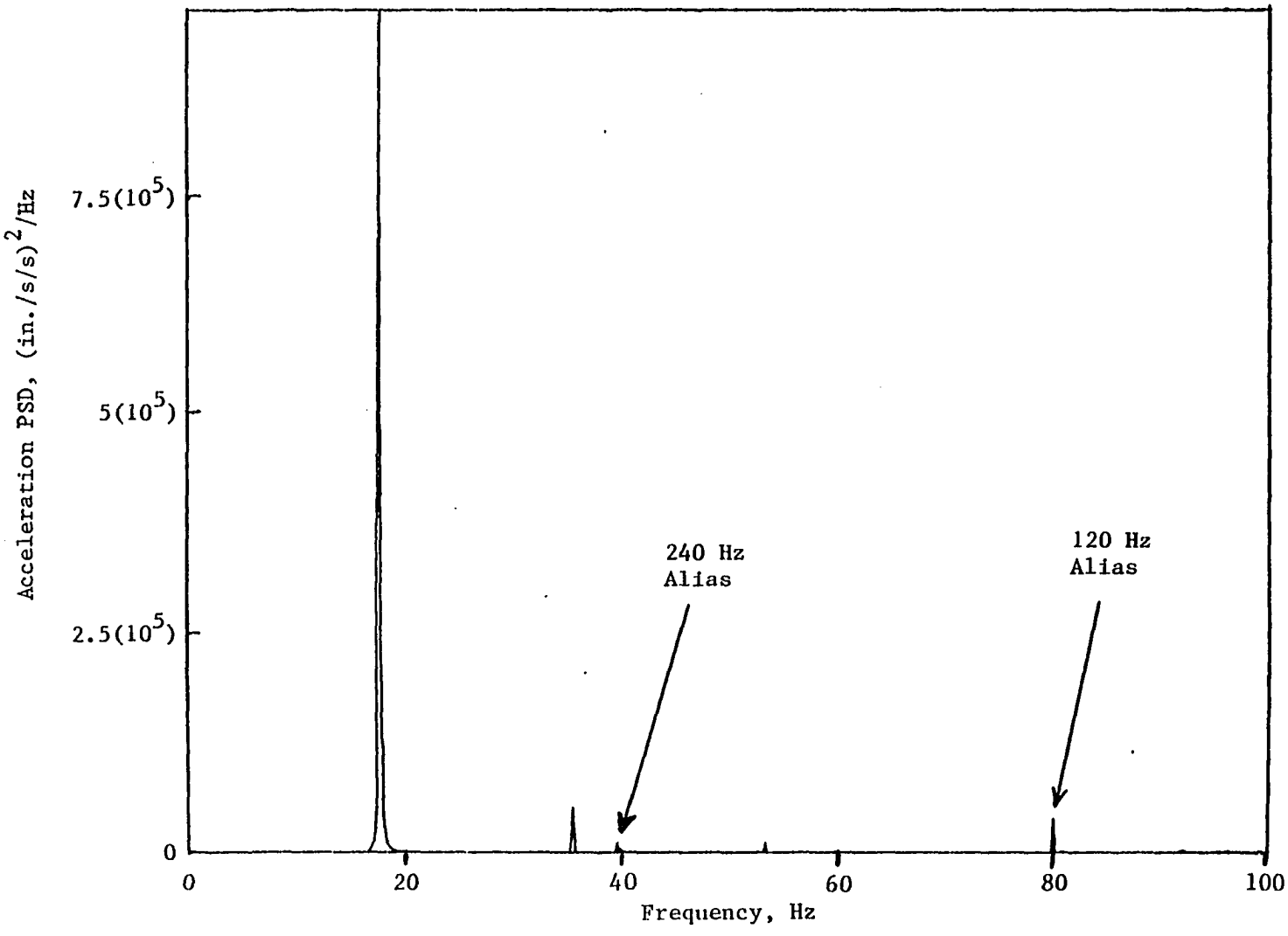

Fig. 33. Power spectrum of acceleration signal for the Model-Tech specimen in mode 1, ambient air

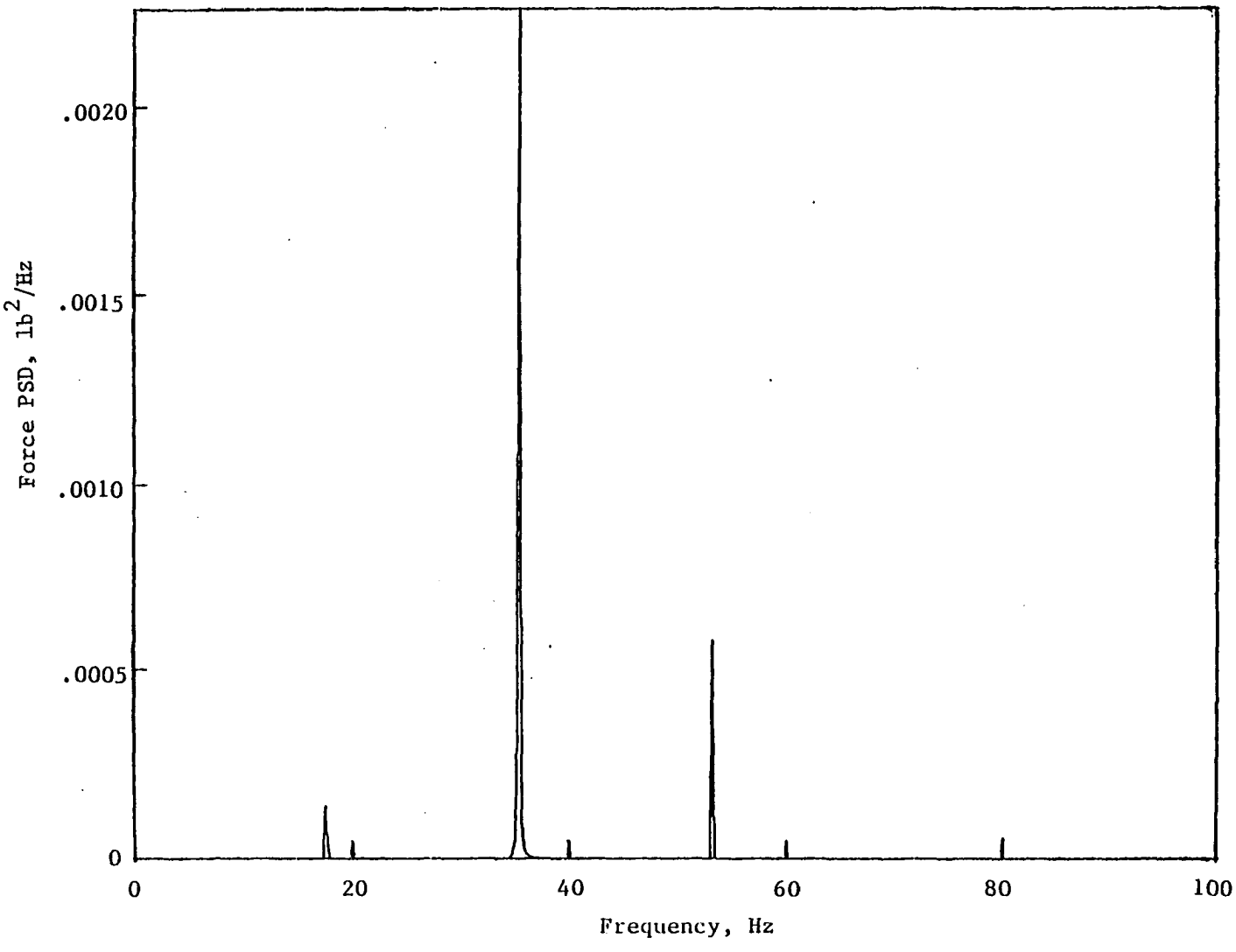

Fig. 34. Power spectrum of force signal for the Model-Tech specimen in mode 1, ambient air

frequency and at the second and third harmonics. A component is also seen at 80 Hz; however, this component is the alias of 120 Hz power line noise wrapping around the Nyquist frequency of the signal processor. Thus, it is only an artifact of the measurement system and may be discarded. The second and third harmonics must be considered since they appear due to the nonlinear motion of the exciter head, caused by the very low driving frequency and the nonlinearities of the exciter head support system.

The effect of the nonlinear shaker motion is seen clearly in Fig. 34. The small acceleration components at the second and third harmonics produce very large forces when compared to the resonant force component. This clearly illustrates how a very small acceleration component at a nonresonant frequency can produce a significant force component. Note that the 120 Hz alias is not present in the force PSD since this signal was conditioned by battery powered equipment so that 120 Hz line noise could not contaminate the signal.

The effect of amplitude on the loss factor for mode 1, calculated from the first frequency component, is shown in Fig. 35. In this case the loss factor shows a significant amplitude dependence which manifests itself for acceleration amplitudes greater than about 800 in./s/s. Below this level the loss factor is essentially constant. The amplitude dependence is probably due to the nonlinear material behavior of the epoxy matrix and the matrix-particle interfaces, with some contribution from air damping.

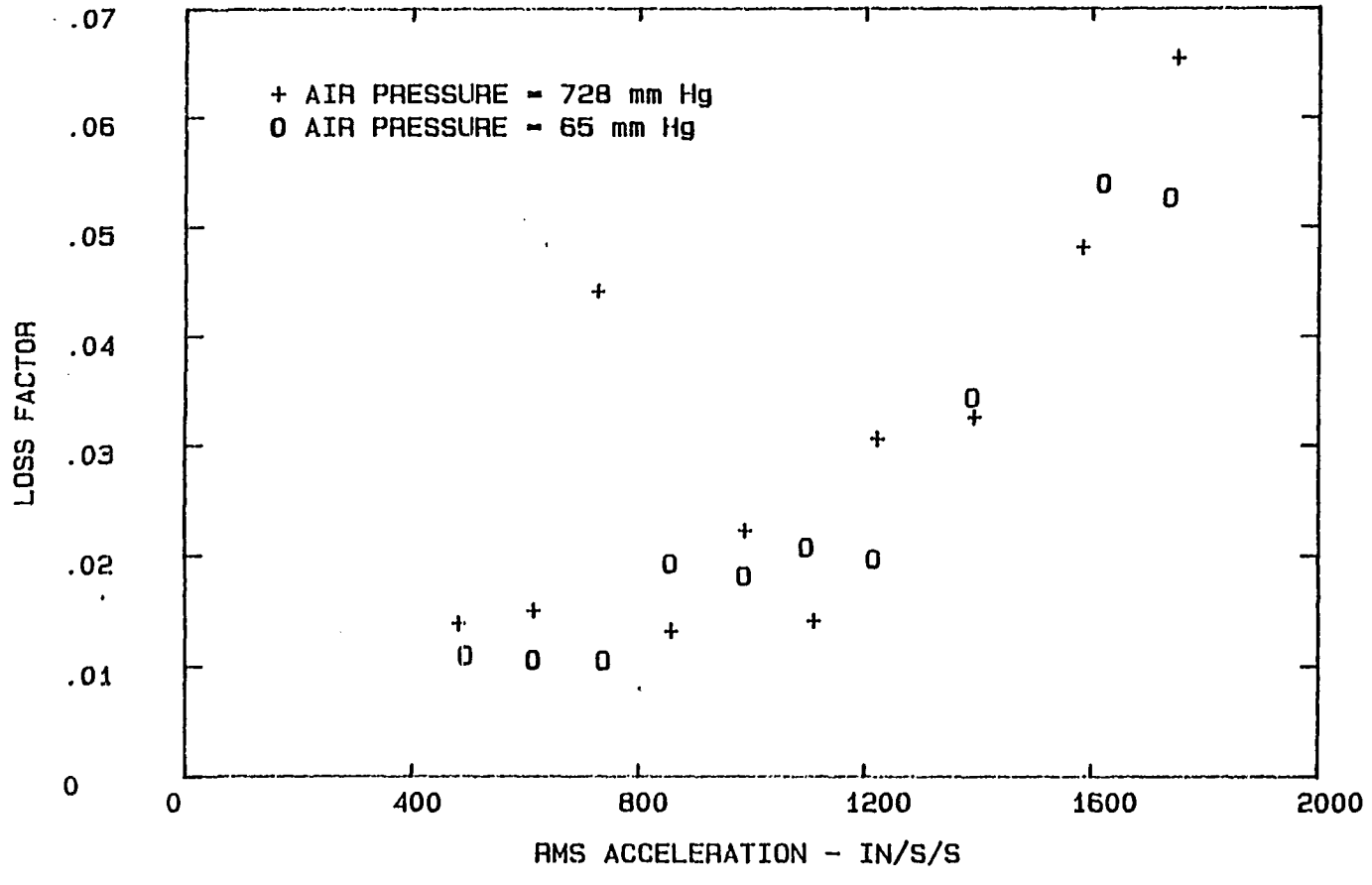

Fig. 35. Loss factor vs acceleration amplitude, mode 1, Model-Tech, first frequency component

Consider next Fig. 36 which is a plot of the loss factor calculated from the first frequency components versus acceleration amplitude for mode 2. Comparing this plot with Fig. 35, an apparent inconsistency is seen. The loss factor for mode 2 is essentially constant with acceleration amplitude over nearly the same range of acceleration amplitudes as the mode 1 test, which showed a strong amplitude effect. This observation can be explained by investigating the maximum stress amplitude associated with a given acceleration amplitude for each mode. It follows from the elementary beam theory and the mode shape functions [58] for a free-free beam (essentially the mode shape at the test condition) that in order to obtain the same stress amplitude in mode 2 as in mode 1 for the Model-Tech specimen, the acceleration amplitude must be increased by a factor of 7.7. Since the loss factor is seen from Fig. 33 to be essentially constant below an acceleration level of 800 in./s/s, the acceleration level required to achieve the same maximum stress amplitude in mode 2 would be about 6,160 in./s/s or 16 g's. This acceleration level would only approach the onset of the amplitude dependent response of the Model-Tech. Thus, the results shown in Figs. 33 and 34 are not contradictory; they only require careful interpretation. Similarly, for the third mode shown in Fig. 37 the input would have to be nearly 22 times as much (45 g's) to approach the onset of nonlinear behavior.

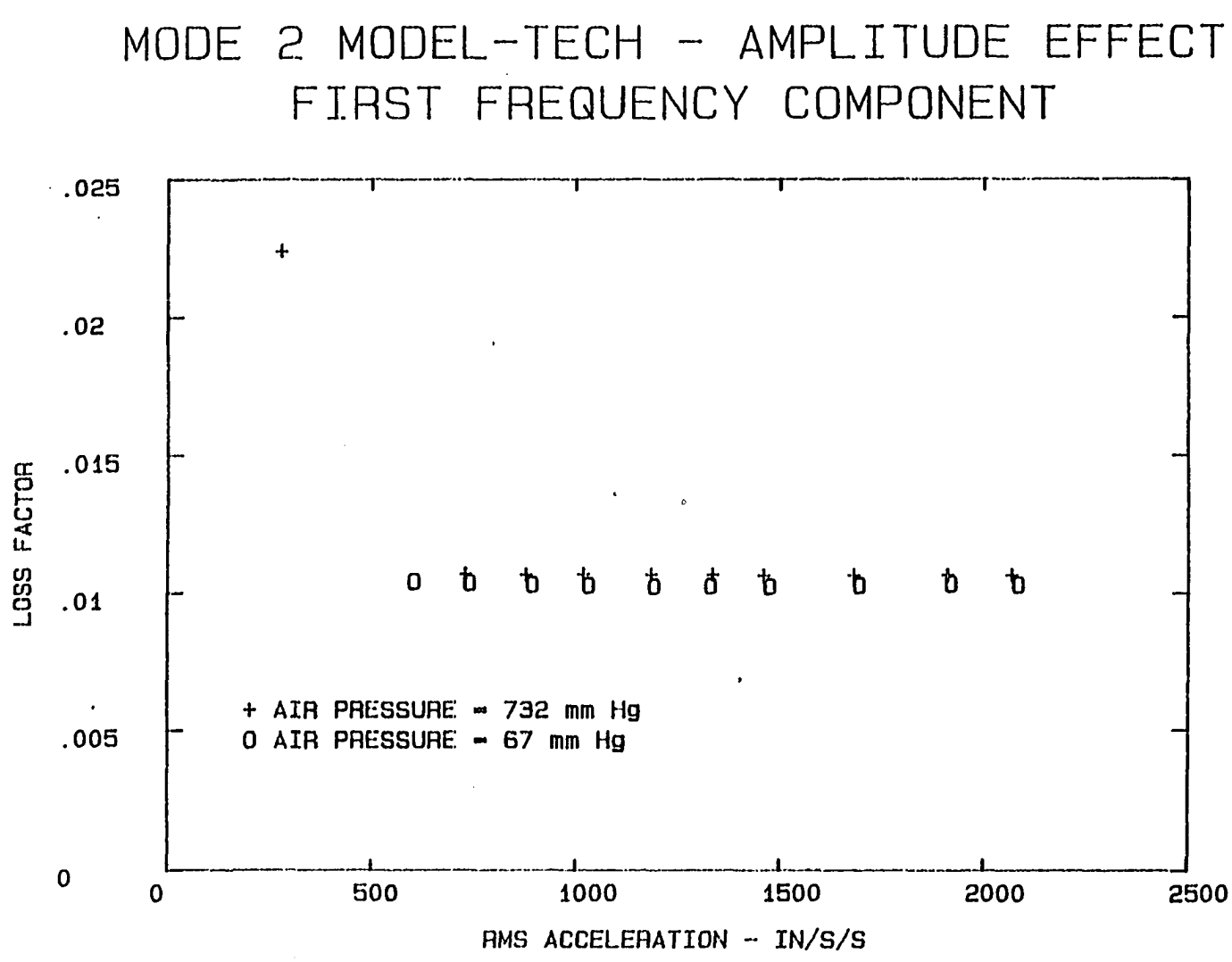

Fig. 36. Loss factor vs acceleration amplitude, mode 2, Model-Tech, first frequency component

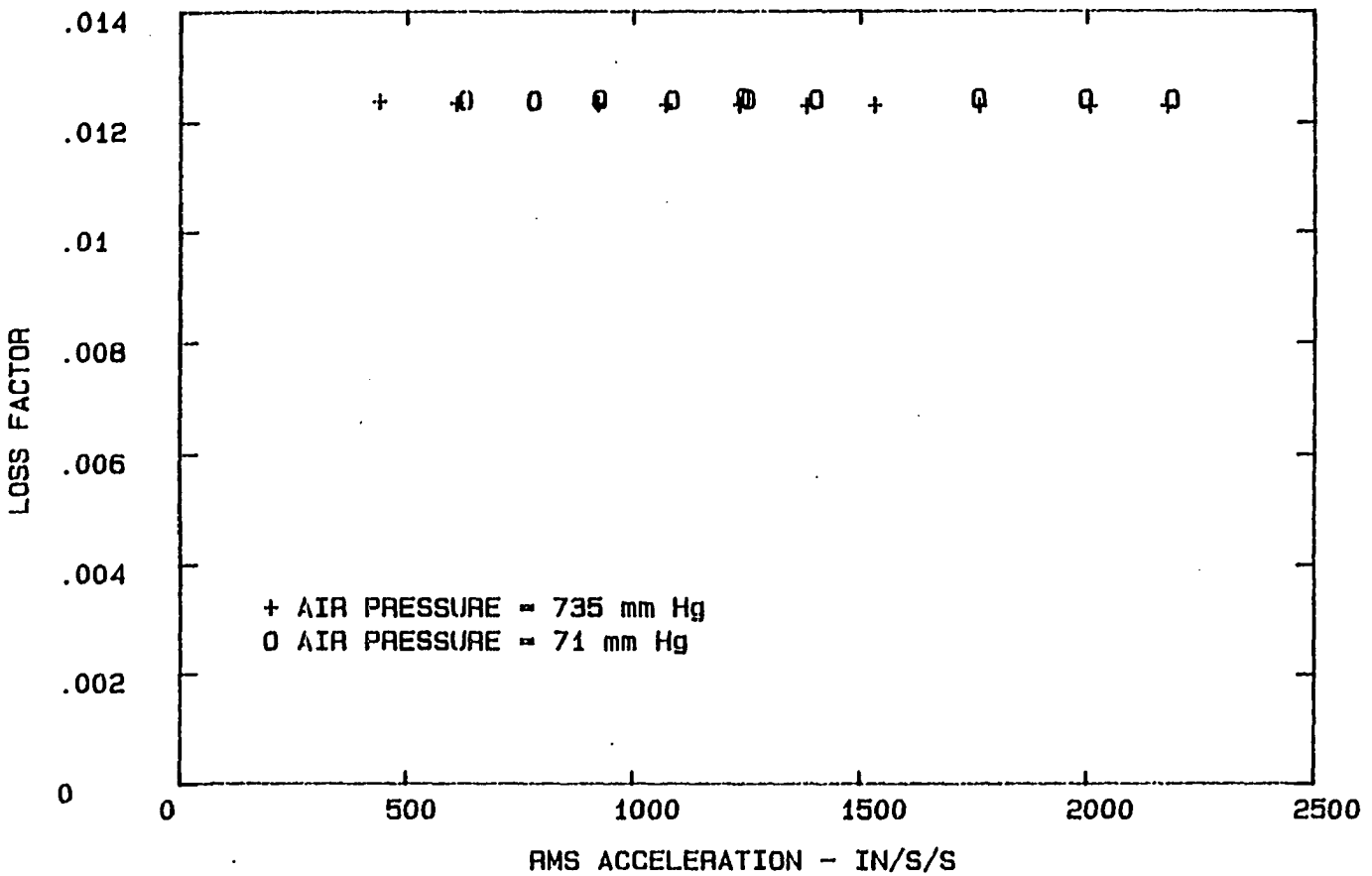

Fig. 37. Loss factor vs acceleration amplitude, mode 3, Model-Tech, first frequency component

The effect of air pressure on the damping of Model-Tech was the same as for aluminum. The dropoff effect, however, was much more dramatic as shown in Fig. 38. The increased effect was probably due to the larger deflection amplitudes obtained by the Model-Tech specimen because of its lower elastic modulus. The dropoff occurred at the same pressure level as before, about 100 mm Hg. This, again, lends some credibility to the notion that the dropoff was due to a rapid change in the flow pattern. The dropoff effect was significant for mode 1 but of diminishing importance for the higher modes.

The frequency dependence of the Model-Tech loss factor at low amplitudes is shown in Fig. 39. The loss factor is plotted against frequency for both Gibson's method and the new method. The loss factor is seen to increase with increasing frequency for both test methods. This is probably due to the viscoelastic nature of the epoxy matrix material previously noted by Gibson and Plunkett [15]. The loss factors determined by the two methods correspond fairly well for the second and third modes; however, for the first mode, the results are quite different.

The most likely reason for the discrepancy between the mode 1 results for the different test methods requires re-examination of Gibson's method. In Gibson's method, the deflection at a point along the beam was measured and used to predict the beam tip deflection, via the cantilever mode

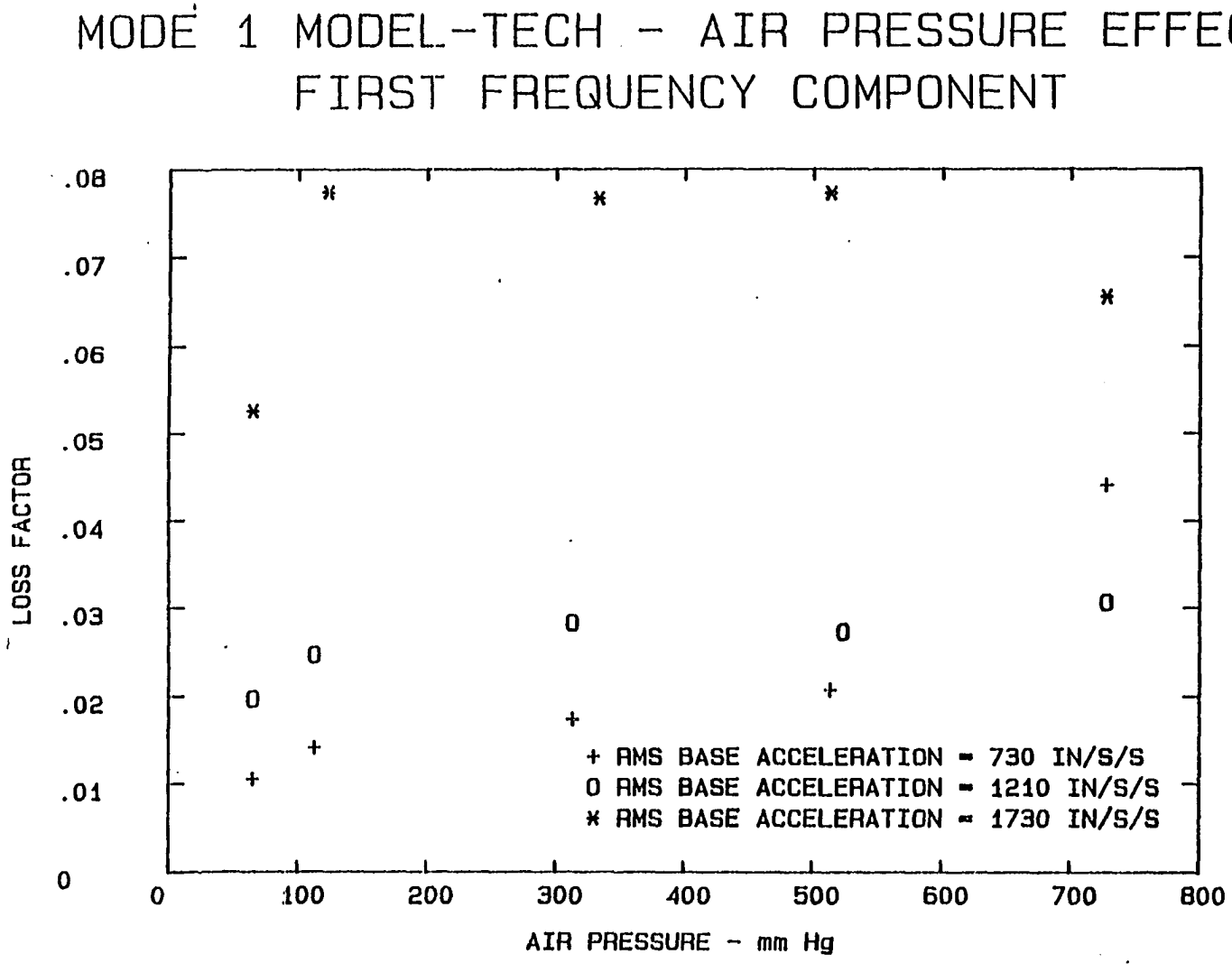

Fig. 38. Loss factor vs air pressure, mode 1, Model-Tech, first frequency component

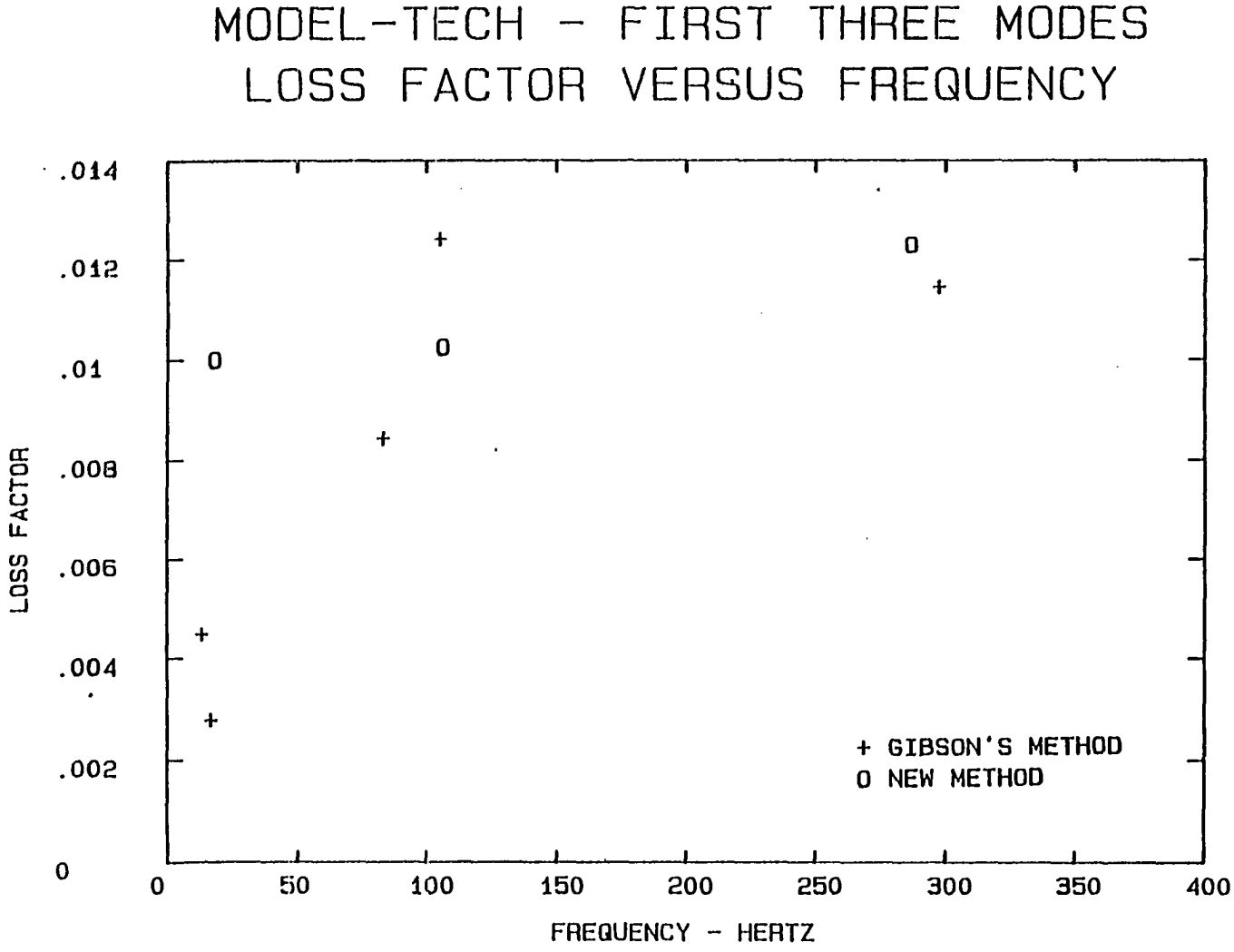

Fig. 39. Loss factor vs frequency, first three modes, Model-Tech, first frequency component

shapes tabulated by Bishop and Johnson [58]. The deflection was measured by a non-contacting eddy current proximity transducer with a fairly small linear measurement range. Therefore, for mode 1 of the Model-Tech specimen, the transducer was located quite close to the specimen base so that the specimen remained in the transducer's linear range. However, with the proximity probe located quite close to the moving base, the base motion became a significant contribution to the beam motion at that point, violating the base fixity assumption implicit in using the mode shape functions [58]. Thus, the beam tip deflection, predicted from the motion at the probe location and the mode shape functions, was too large.

The magnitude of the tip deflection error is dependent on the base motion contribution to the probe location motion and the ratio of the beam tip to probe location mode shape amplitudes. For the case of the Model-Tech in mode 1, the ratio of mode shape amplitudes was about 10 so a small base motion contribution to the probe location motion led to a large error in the beam tip deflection prediction. Since the beam tip deflection appears in the denominator of the loss factor equation for Gibson's method, Eq. (13), beam tip deflections which are too large produce loss factors which are too small. Thus, the loss factor for mode 1, Model-Tech, is most reliably given by the new method. Note also that the loss factors, shown in Fig. 39, from the new method exhibit a linear relationship with frequency as predicted by the Kelvin-Voigt model.

The probe location motion error was significant only for mode 1 with the Model-Tech specimen. For the aluminum specimen the stiffness was a factor of 10 larger, and the proximity probe was always near the beam tip. The higher modes for Model-Tech also exhibited sufficiently small amplitudes for the probe to remain near the beam tip. Thus, the results for the tests using Gibson's method were reasonably good for all cases except mode 1, Model-Tech. However, this case does illustrate the potential for significant errors from Gibson's method as well as the reliability of the new method.

The preceding sections have presented several plots of data gathered using the new test method. These plots were selected because they typified the results obtained for all cases. However, since the data from a specific test may be of interest, plots are included in Appendix B which, when added to those contained in this chapter, give a complete set of the data for all modes and both specimens.

CHAPTER V. CONCLUSIONS

The new test method has been shown to be a viable method for determining material damping and is superior to Gibson's method for several reasons. A significant advantage of the new method over Gibson's method is the ability to accurately determine material damping in the fundamental mode of vibration, as illustrated by the results from the Model-Tech specimen in mode 1. Since the frequency-dependent characteristics of material damping are often of great interest, the reliable measurement of damping is quite important. For this reason, if for no other, the new method is a substantial improvement in the field of damping investigation.

The use of frequency analysis in the measurement of damping is another significant improvement. Frequency analysis allows the investigation of the various frequency components of the force and acceleration signals, leading to an improved understanding of the various phenomena at work in the vibrating system. This improved analysis has shown that the non-material damping contributions can be quite significant and can mask the actual material characteristics if not properly interpreted.

The test condition of system resonance is quite compatible with the frequency analysis approach to data analysis. At resonance the linear elastic and inertia forces cancel each other, leaving only damping and nonlinear force contributions

to the driving force signal. These remaining force components are small and are usually masked by the large linear elastic and inertia forces. However, at resonance the small force components become significant and may be investigated. In addition, at resonance the vibration exciter needs to produce only a small force to drive the system. The small force requirement placed on the exciter leads to essentially sinusoidal base motion, as assumed in the derivation. This is another significant improvement over Gibson's method which violated this assumption.

The material damping of aluminum has again been shown to be linear, following the Zener Thermal Relaxation Theory. The material damping of the Model-Tech has shown itself to have two distinct behaviors. At small amplitudes the damping is seen to be linear, acting in a classical viscoelastic manner. The damping is independent of amplitude but increasing with increasing frequency. At large amplitudes, however, the damping increases significantly with increasing amplitude. This nonlinear material damping behavior is probably due to slip at the matrix-particle interfaces.

Air damping has been shown to have amplitude dependence consistent with the theoretical expectations for a drag effect dependent on velocity and velocity squared. The frequency components of the air damping forces are also consistent with these theoretical expectations. Thus, it is reasonable to conclude that air damping is caused by a drag effect proportional to velocity and velocity squared.

Air pressure has been shown to play an important role in air damping. At air pressures above about 100 mm Hg, air damping is a linear function of air pressure. This effect is predictable from the pressure dependence of density through the ideal gas law. For low pressures, below about 100 mm Hg, the loss factor drops off rapidly. This effect is probably due to a change in the flow pattern surrounding the beam.

CHAPTER VI. RECOMMENDATIONS FOR FURTHER WORK

The new test method has proven itself to be accurate, useful, and convenient to run. However, further improvements could be made in the instrumentation to alleviate such problems as the power line noise and vacuum pump contributions. A significant improvement could be made with better vibration isolation of the test system from outside vibration sources. This would result in cleaner power spectra and a better signal to-noise ratio.

A useful study could be made of the clamping technique's effect on system damping by machining specimens from a large block of material so that the clamping block would be a part of the specimen. This would eliminate most of the clamping block friction damping from the system, allowing better investigation of material and friction damping.

The new method might also be useful for nondestructive evaluation studies. The various frequency components of the force signal obtained during these tests may be important in damage assessment or crack growth monitoring.

A very strong candidate for future development is the study of air damping at low pressure. The dropoff effect noted in this work was explained only in a qualitative way, based on some questionable assumptions. A careful study could provide a quantitative understanding of this phenomenon.

REFERENCES

1. S. H. Crandall. "The Role of Damping in Vibration Theory." J. Sound & Vib., 11(1): 3-18 (1970).

2. C. W. Bert. "Material Damping: An Introductory Review of Mathematical Models, Measures and Experimental Techniques." J. Sound & Vib., 29(2): 129-153 (1973).

3. J. D. Rogers. "Dynamic Response of Materials in Vibrations." Proc. 1984 SEM Fall Mtg., Milwaukee, Wis., November 4-7, 1984, pp. 12-17.

4. W. T. Thomson. Theory of Vibration with Applications. Englewood Cliffs, New Jersey: Prentice-Hall, 1981.

5. L. Rogers. "On Modeling Viscoelastic Behavior." Shock & Vib. Bull., 51: 55-69 (April 1981).

6. L. Rogers. "Operators and Fractional Derivatives for Viscoelastic Constitutive Equations." J. Rheology, 27(4): 351-372 (1983).

7. R. L. Bagley and P. J. Torvik. "Fractional Calculus - a Different Approach to the Analysis of Viscoelastically Damped Structures." AIAA J., 21(5): 741-748 (May 1983).

8. P. J. Torvik and R. L. Bagley. "On the Appearance of the Fractional Derivative in the Behavior of Real Materials." J. Appl. Mech., 51: 294-298 (June 1984).

9. R. C. Koeller. "Applications of Fractional Calculus to the Theory of Viscoelasticity." J. Appl. Mech., 51: 299-304 (June 1984).

10. D. I. G. Jones. "Viscoelastic Materials for Damping Applications." Damping Appl. for Vib. Control, ed. P. J. Torvik, ASME Pub. AMD-V.38: 27-51 (1981).

11. B. J. Lazen. Damping of Materials and Members in Structural Mechanics. London: Pergamon Press, 1968.

12. C. Zener. Elasticity and Anelasticity of Metals. Chicago, Ill.: Univ. of Chicago Press, 1948.

13. J. M. Lee. "A Study of Material Damping of Aluminum Alloy 2024-T4 in Longitudinal Vibration." M.S. Thesis, Iowa State University, Ames, Iowa (1972).

14. W. E. Baker, W. E. Woolam, and D. F. Young. "Air and Internal Damping of Thin Cantilever Beams." Int'l. J. Mech. Sci., 9: 743-766 (1967).

15. R. F. Gibson and R. Plunkett. "A Forced-Vibration Technique for Measurement of Material Damping." Exp. Mech., 11(8): 297-302 (Aug. 1977).

16. S. H. Crandall. "On Scaling Laws for Material Damping." NASA, TN D-1467, Dec. 1962.

17. T. H. Dawson. "Continuum Description of Hysteresis Damping of Vibrations." Int'l. J. Solids Struct., 14: 457-464 (1978).

18. I. R. Whiteman. "A Mathematical Model Depicting the Stress-Strain Diagram and the Hysteresis Loop." J. Appl. Mech., 26: 95-100 (March 1959).

19. P. W. Whaley. "Entropy Production During Fatigue as a Criterion for Failure: A Local Theory of Fracture in Engineering Materials." ONR Final Report, Contract N00014-82-K-0804 NR229-046, Dec. 1984.

20. P. W. Whaley. "A Mathematical Model for Material Damping and Fatigue Damage Based on Random Yielding." Personal communication. Dept. of Engr. Mech., Univ. of Nebraska, Lincoln, Nebraska, 1986.

21. S. Motegi. "A Phenomenological Theory of Hysteresis Damping of Vibrations in Ferromagnetic Materials." Communicated by G. A. Maugin. Int'l. J. Engr. Sci., 20(7): 823-834 (1982).

22. R. D. Adams. "The Damping Characteritics of Certain Steel, Cast Irons and Other Metals." J. Sound & Vib., 23(2): 199-216 (1972).

23. R. F. Gibson and R. Plunkett. "Dynamic Stiffness and Damping of Fiber-Reinforced Composite Materials." Shock & Vib. Digest, 9(2): 9-17 (February 1977).

24. R. F. Gibson. "Recent Research on Dynamic Mechanical Properties of Fiber Reinforced Composite Materials and Structures." Shock & Vib. Digest, 15(2): 3-15 (February 1983).

25. C. W. Bert. "Compoaite Materials: A Survey of the Damping Capacity of Fiber Reinforced Composites." Damping Appl. for Vib. Control, ed. P. J. Torvik. ASME Pub. AMD-V., 38: 53-63 (1981).

26. R. F. Gibson and R. Plunkett. "Dynamic Mechanical Behavior of Fiber Reinforced Composites: Measurement and Analysis." J. Comp. Mat., 10: 325-341 (1976).

27. J. P. DenHartog. Mechanical Vibrations. New York: McGraw-Hill, 1956.

28. R. Plunkett. "Friction Damping." Damping Appl. for Vib. Control, ed. P. J. Torvik. ASME Pub. AMD-V. 38: 65-74 (1981).

29. R. F. Gibson, A. Yau, and D. A. Riegner. "Vibration Characteristics of Automotive Composite Material." ASTM Symp. on Short Fiber-Reinforced Comp., Minneapolis, Minn., April 14, 1980.

30. R. F. Gibson, S. K. Chaturvedi, and C. T. Sun. "Complex Moduli of Aligned Discontinuous Fibre-Reinforced Polymer Composites." J. Mat. Sci., 17: 3499-3509 (1982).

31. D. F. Golla and P. C. Hughes. "Dynamics of Viscoelastic Structures--A Time Domain, Finite Element Formulation." J. Appl. Mech., 52: 897-906 (December 1985).

32. A. K. Misra and V. J. Modi. "The Influence of Satellite Flexibility on Orbital Motion." Celestial Mech., 17: 145-165 (1978).

33. D. J. Mead. "The Practical Problems of Assessing Damping Treatment." J. Sound & Vib., 1(3): 270-291 (1964).

34. A. D. Nashif, D. I. G. Jones, and J. P. Henderson. Vibration Damping. New York: Wiley, 1985.

35. R. D. Adams, P. Cawley, C. J. Pye, and B. J. Stone. "A Vibration Technique for Nondestructively Assessing the Integrity of Structures." J. Mech. Engr. Sci., 20(2): 93-100 (1978).

36. B. S. Haisty and W. T. Springer. "The Longitudinal Vibration Characteristics of a Uniform Beam Containing Two Symmetrical Discontinuities." Proc. 1985 SEM Spring Mtg., Las Vegas, Nevada, June 10-15, 1985, pp. 389-393.

37. M. E. Reznicek and W. T. Springer. "Damage Assessment of Traversely Vibrating Uniform Beams Containing a Symmetric Discontinuity." Proc. 1985 SEM Spring Mtg., Las Vegas, Nevada, June 10-15, 1985, pp. 404-409.

38. T. DiBenedetto, J. V. Gauchel, R. L. Thomas, and J. W. Barlow. "Nondestructive Determination of Fatigue Crack Damage in Composites Using Vibration Tests." J. Materials, 7(2): 211-215 (June 1972).

39. R. Mantena, T. A. Place, and R. F. Gibson. "Characterization of Matrix Cracking in Composite Laminates by the Use of Damping Capacity Measurements." Role of Surfaces and Interfaces in Material Damping, 1985 ASM Metals Cong., Toronto, Canada, October 14-17, 1985.

40. P. W. Whaley, P. S. Chen, and G. M. Smith. "Continuous Measurement of Material Damping During Fatigue Tests." Exp. Mech., 24: 342-348 (December 1984).

41. R. L. Jones and G. E. Warren. "Internal Damping as a Disgnostic Indicator of Hyperbaric Chamber Integrity." Proc. 1985 SEM Spring Mtg., Las Vegas, Nevada, June 10-15, 1985, pp. 394-403.

42. J. M. Lee and K. G. McConnell. "Experimental Cross Verification of Damping in Three Metals." Exp. Mech., 15(9): 221-225 (Sept. 1975).

43. R. Sierakowski, G. Hemp, and A. Hokstad. "Some Damping Properties of Aluminum Particle Filled Epoxy Composites." J. Comp. Mat., 5: 417-420 (July 1971).

44. D. G. Stephens and M. A. Scavullo. "Investigation of Air Damping of Circular and Rectangular Plates, a Cylinder, and a Sphere." NASA TN D-1865 (1965).

45. O. B. Sorensen and V. Tarnow. "Measurement of Elastic Modulus and Loss Factor of PVC at High Frequencies." B&K Instruments, Inc., Tech. Review No. 2, pp. 19-27 (1977).

46. W. J. Hanson and G. A. Hampel. "A Performance Comparison of Vibration Damping Materials." Sound & Vib., 18: 22-34 (July 1984).

47. S. A. Suarez, R. F. Gibson, and L. R. Deobald. "Random and Impulse Techniques for Measurement of Damping in Composite Materials." Exp. Tech., 8(10): 19-24 (Oct. 1984).

48. R. L. Wegel and H. Walther. "Internal Dissipation in Solids for Small Cyclic Strains." J. Appl. Physics, 6: 141-157 (April 1935).

49. G. W. Laird and H. B. Kingsbury. "A Method of Determining Complex Moduli of Viscoelastic Materials." Exp. Mech., 13(3): 126-131 (March 1973).

50. D. M. Norris, Jr., and W. Young. "Complex-Modulus Measurements by Longitudinal Vibration Testing." Exp. Mech., 10(2): 93-96 (Feb. 1970).

51. R. J. Hooker. "Damping in Metals Under Combined Stress Loading." J. Sound & Vib., 79(2): 243-262 (1981).

52. N. Basavanhally and R. D. Marangoni. "Measurement of Mechanical Vibration Damping in Orthotropic, Composite and Isotropic Plates Based on a Continuous System Analysis." Int'l. J. Solids Struc., 13: 699-707 (1977).

53. R. Plunkett and M. Sax. "Nonlinear Material Damping for Nonsinusoidal Strain." J. Appl. Mech., 45: 883-888 (Dec. 1978).

54. P. W. Whaley and P. S. Chen. "Experimental Measurement of Material Damping Using Digital Test Equipment." Shock & Vib. Bull., 53(Part 4): 41-50 (May 1983).

55. N. Granick and J. E. Stern. "Material Damping of Aluminum by a Resonant-Dwell Technique." NASA TN D-2893 (August 1965).

56. R. F. Gibson, A. Yau, and D. A. Riegner. "An Improved Forced Vibration Technique for Measurement of Material Damping." Proc. SESA 1981 Spring Conf., Dearborn, Mich., May 31-June 4, 1981.

57. J. D. Rogers. "Damping and Vibration Characteristics of an Aluminum Particle Filled Epoxy." M.S. Thesis, Iowa State University, Ames, Iowa (1984).

58. R. E. D. Bishop and D. C. Johnson. The Mechanics of Vibration. Cambridge, England: Cambridge Univ. Press, 1960.

59. J. W. Dally, W. F. Riley, and K. G. McConnell. Instrumentation for Engineering Measurement. New York: Wiley, 1984.

60. J. C. Snowdon. Vibration and Shock in Damped Mechanical Systems. New York: Wiley, 1968.

61. J. L. Hilburn and D. B. Johnson. Manual of Active Filter Design. 2nd ed. New York: McGraw-Hill, 1983.

62. J. S. Bendat and A. G. Piersol. Engineering Applications of Correlation and Spectral Analysis. New York: Wiley, 1980.

63. V. J. Modi and D. T. Poon. "Dynamics of Neutrally Buoyant Inflated Viscoelastic Tapered Cantilevers Used in Underwater Applications." J. Mech. Design, 100: 337-346 (April 1978).

64. A. O. St. Hilaire and P. G. Vaidya. "Finite Amplitude Analysis of a Flow-Structure Interaction Problem." J. Fluid Mech., 67(Part 2): 377-396 (1975).

65. B. R. Munson and R. W. Douglass. "Viscous Flow in Oscillatory Spherical Annuli." Phys. Fluids, 22(2): 205-208 (February 1979).

ACKNOWLEDGMENTS

I would like to thank my wife Brenda for her support and encouragement during my graduate study. I also must thank her for typing this manuscript.

A very special thanks goes to Dr. Kenneth G. McConnell for his endless patience, encouragement, and sound guidance throughout this project. A note of appreciation goes to my other committee members, Dr. Leo C. Peters, Dr. Steven B. Skaar, Dr. Loren W. Zachary, Dr. Lowell F. Greimann, and Professor William F. Riley, for their support.

A note of thanks goes to the City of Ames, Public Works Department for providing the piece of water main pipe which became my reduced pressure testing chamber.

I also wish to thank the Department of Engineering Science & Mechanics and the Engineering Research Institute at Iowa State University for their continuous support.

APPENDIX A. DATA ACQUISITION PROGRAM FOR NORLAND DIGITAL PROCESSING OSCILLOSCOPE

```
001    DPLY A B R0 R1 E I DPLY
002    DMX Q3 1
003    DMX Q4 1
004    TRG.H
005    DMX Q3 0
006    DMX Q4 0
007    0.0000 ==> I
008    0.0000 ==> A
009    0.0000 ==> B
010    0.0000 ==> C
011    0.0000 ==> D
012    0.0000 ==> R0
013    0.0000 ==> R1
014    0.0000 ==> R2
015    0.0000 ==> R3
016    0.0000 ==> R4
017    0.0000 ==> R5
018    2048.0 ==> HSETP
019    2048.0 ==> HSETQ
020    HSETP
021    HSETQ
022    I * 1024.0 ==> R9
023    DMX R9 ==> Q3
024    DMX R9 ==> Q4
025    Q3 * 38640. ==> Q3
026    QMOVR
027    1/DT ==> E
028    E / 1024.0 ==> R7
029    PMAX
030    QMAX
031    QMAX
032    QMAX
033    QMAX
034    QMAX
035    QMAX
036    1/DT ==> E
037    5.0000 * E ==> R6
038    R6 / R7 ==> R8
039    RMS ==> E
040    E ==> A'
041    A + E ==> A
```

```
042   PNEXT
043   QNEXT
044   RMS ==> E
045   E ==> B'
046   B + E ==> B
047   PSD Q3 ==> Q1
048   Q1 ==> Q3
049   PSD Q4 ==> Q2
050   Q3 ==> Q1
051   R8 - 4.0000 ==> HSETP
052   R8 + 4.0000 ==> HSETQ
053   HSETP
054   HSETQ
055   INTPQ ==> E
056   2.0000 * E ==> E
057   SQRT E ==> E
058   E ==> C'
059   E + R0 ==> R0
060   PNEXT
061   QNEXT
062   INTPQ ==> E
063   2.0000 * E ==> E
064   SQRT E ==> E
065   E ==> D'
066   E + R1 ==> R1
067   R8 * 2.0000 ==> R8
068   R8 - 4.0000 ==> HSETP
069   R8 + 4.0000 ==> HSETQ
070   HSETP
071   HSETQ
072   INTPQ ==> E
073   2.0000 * E ==> E
074   SQRT E ==> E
075   E ==> E'
076   E + R2 ==> R2
077   PNEXT
078   QNEXT
079   INTPQ ==> E
080   2.0000 * E ==> E
081   SQRT E ==> E
082   E ==> D
083   E + R3 ==> R3
084   R8 * 1.5000 ==> R8
085   RB - 4.0000 ==> HSETP
086   RB + 4.0000 ==> HSETQ
087   HSETP
088   HSETQ
089   INTPQ ==> E
090   2.0000 * E ==> E
091   SQRT E ==> E
092   E ==> C
093   E + R4 ==> R4
```

```
094    PNEXT
095    QNEXT
096    INTPQ ==> E
097    2.0000 * E ==> E
098    SQRT E ==> E
099    E + R5 ==> R5
100    INCI
101    4.0000 IF > I
102    GOTO 18.
103    END
104    A / 4.0000 ==> A
105    B / 4.0000 ==> B
106    R0 / 4.0000 ==> R0
107    R1 / 4.0000 ==> R1
108    R2 / 4.0000 ==> R2
109    R3 / 4.0000 ==> R3
110    R4 / 4.0000 ==> R4
111    R5 / 4.0000 ==> R5
112    PRINT R6 R7 A B R0 R1 R2 R3 R4 R5 PRINT
```

APPENDIX B. ADDITIONAL PLOTS OF TEST DATA

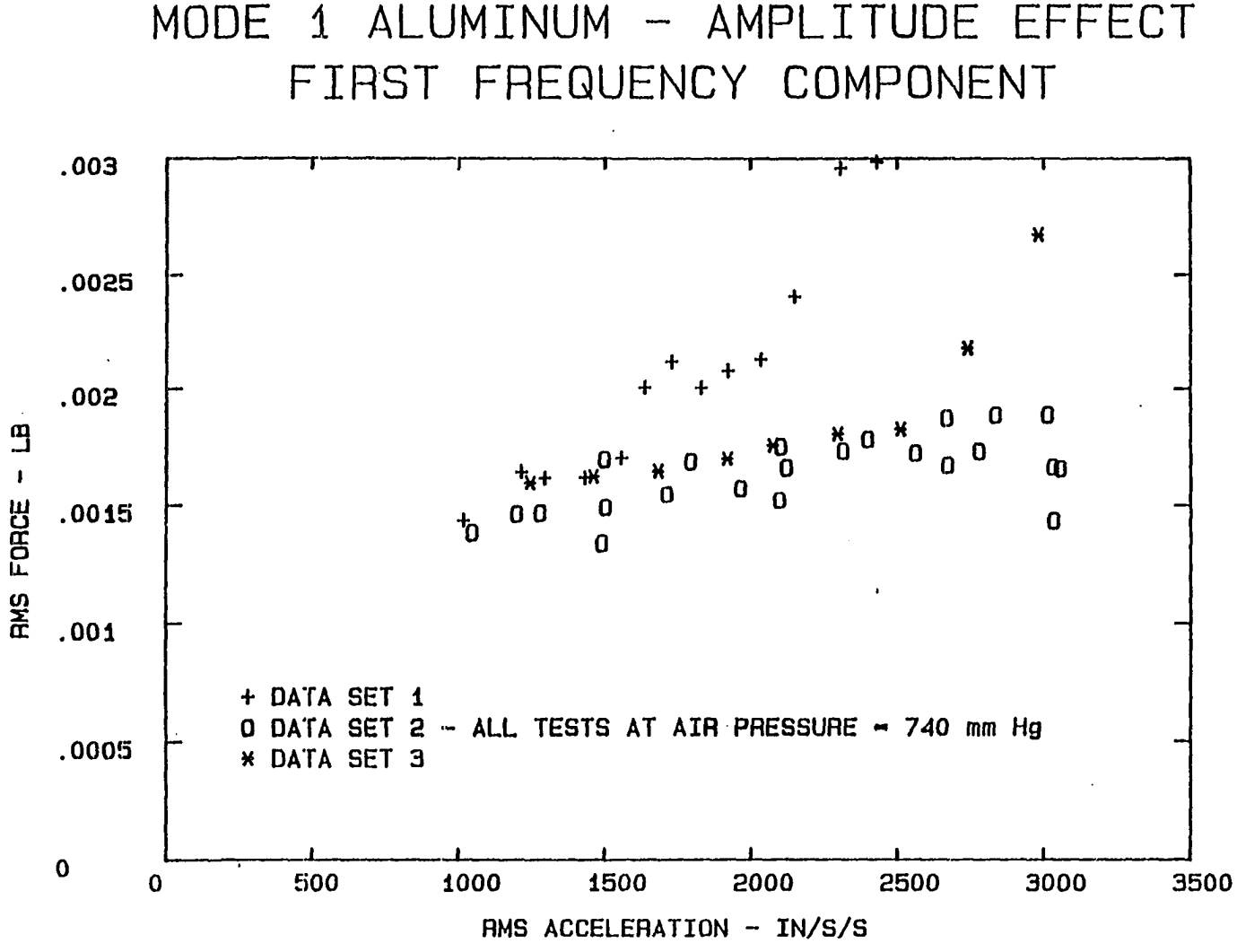

Fig. B-1. Force vs acceleration amplitude, mode 1, aluminum, first frequency component

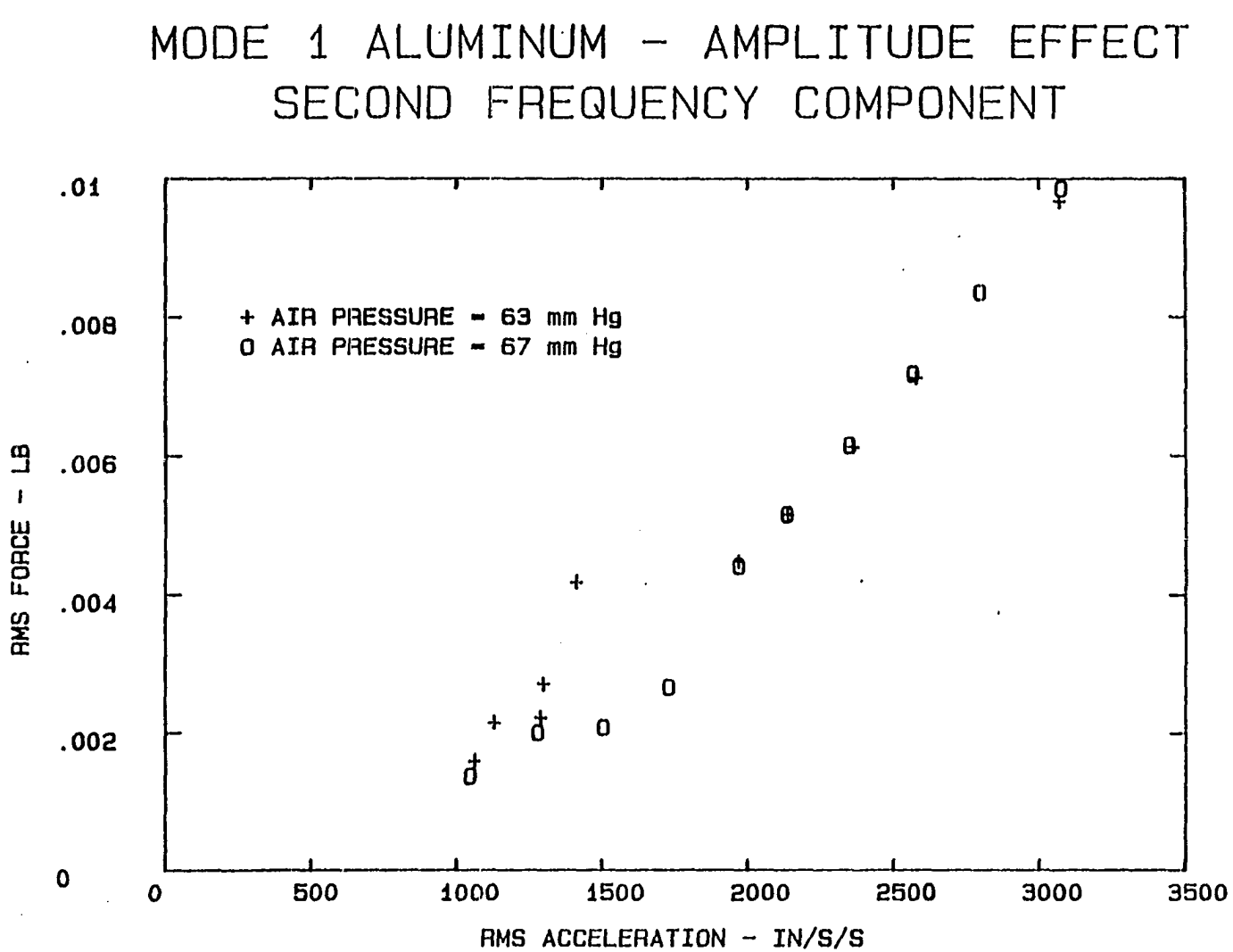

Fig. B-2. Force vs acceleration amplitude, mode 1, aluminum, second frequency component

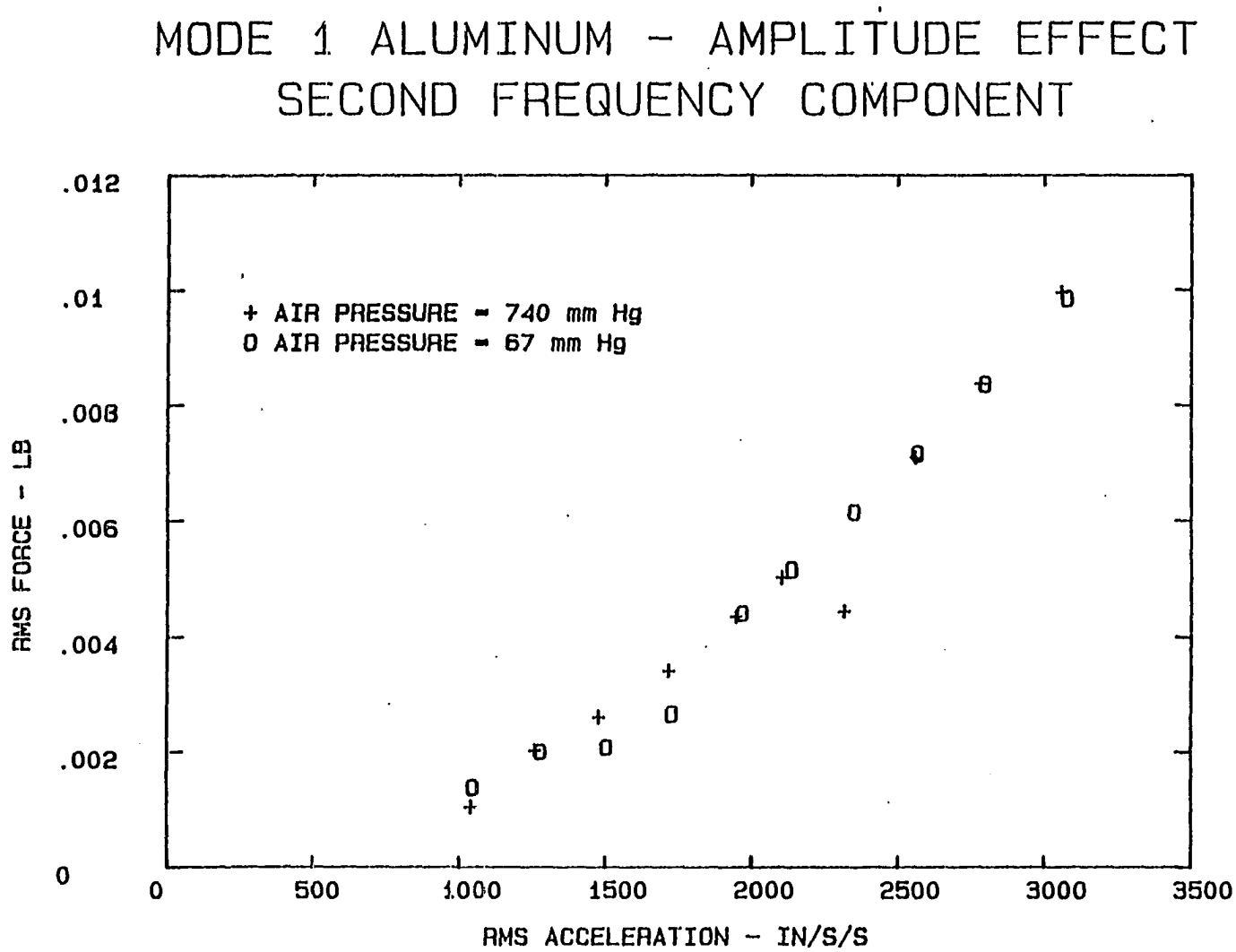

Fig. B-3. Force vs acceleration amplitude, mode 1, aluminum, second frequency component

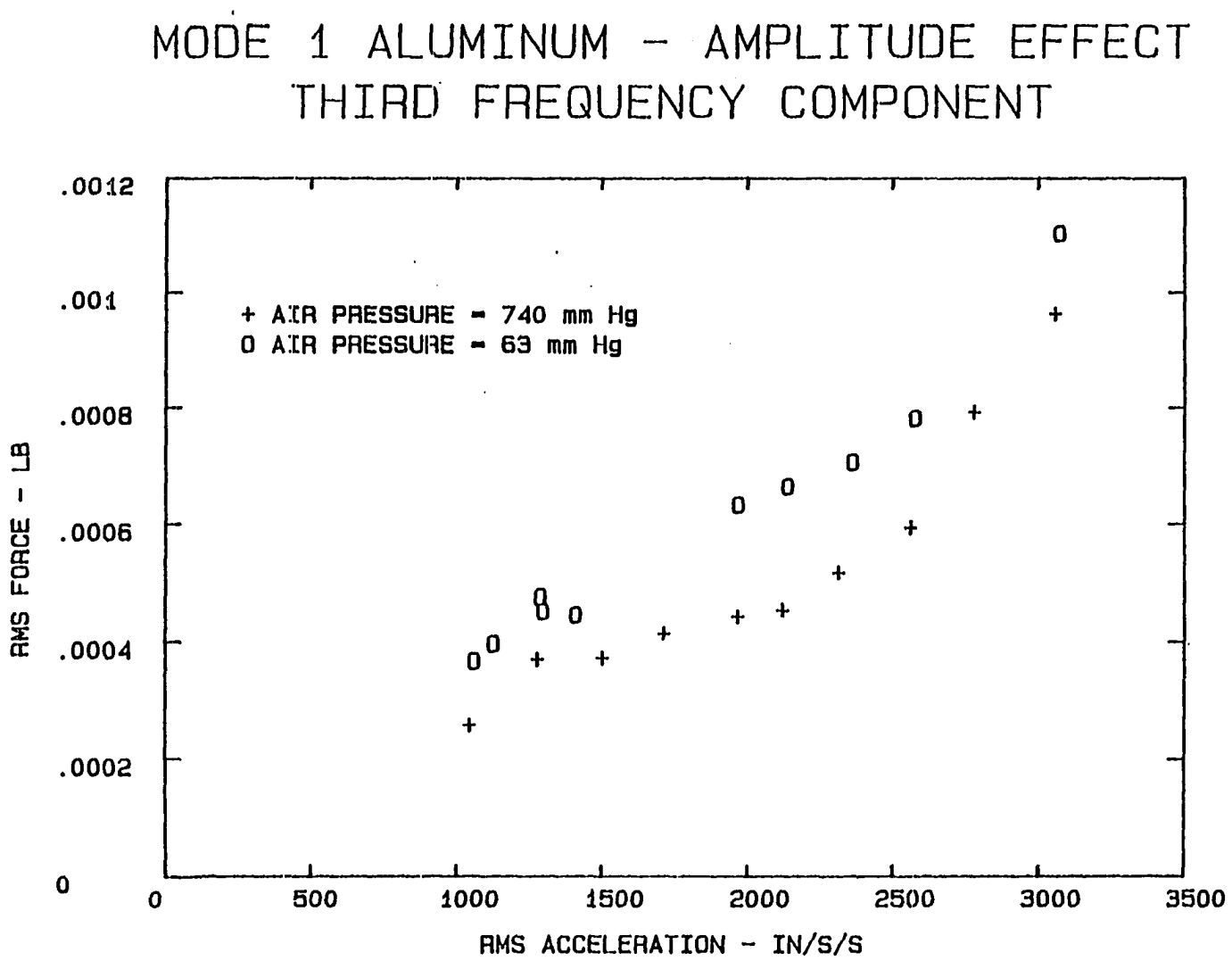

Fig. B-4. Force vs acceleration amplitude, mode 1, aluminum, third frequency component

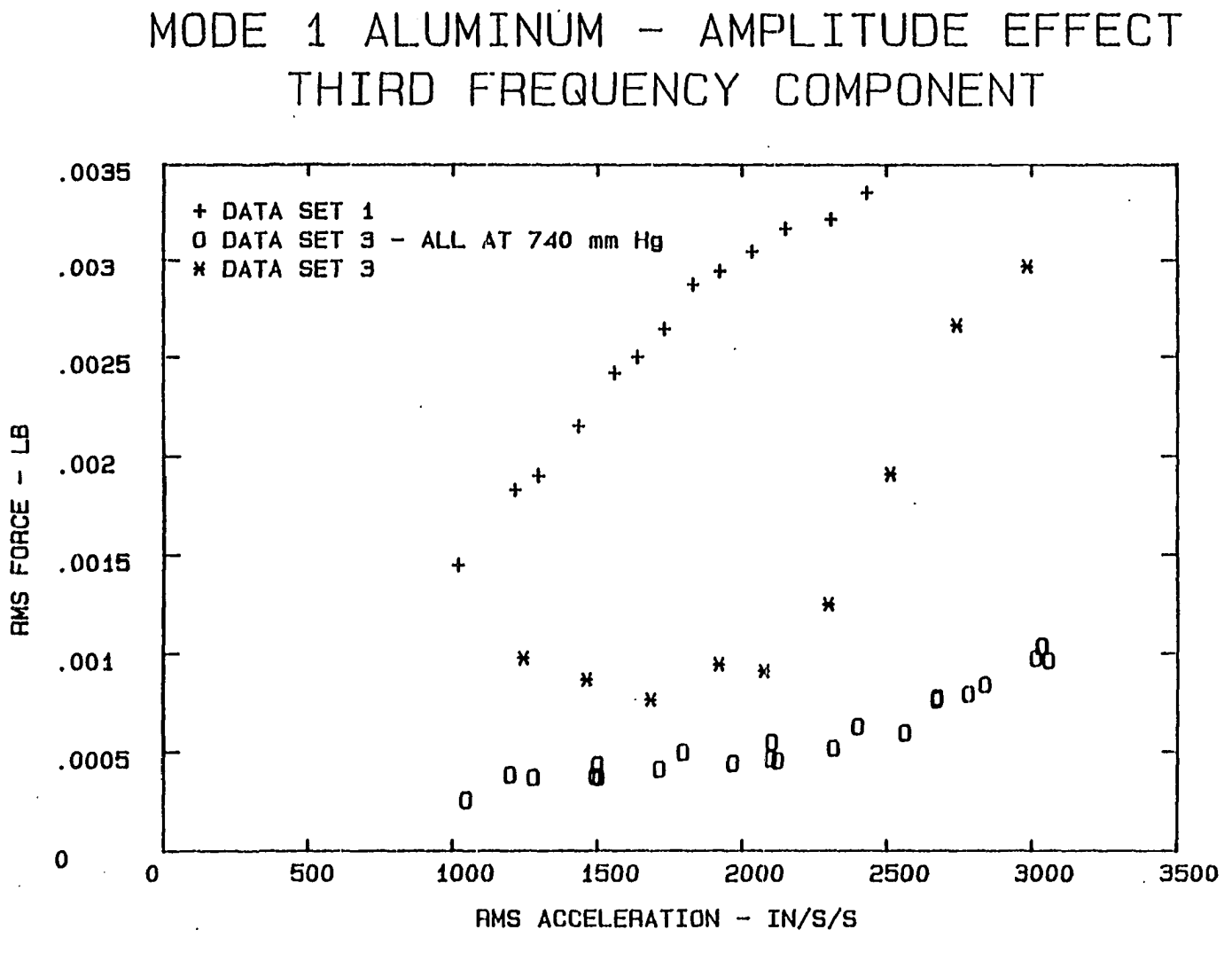

Fig. B-5. Force vs acceleration amplitude, mode 1, aluminum, third frequency component

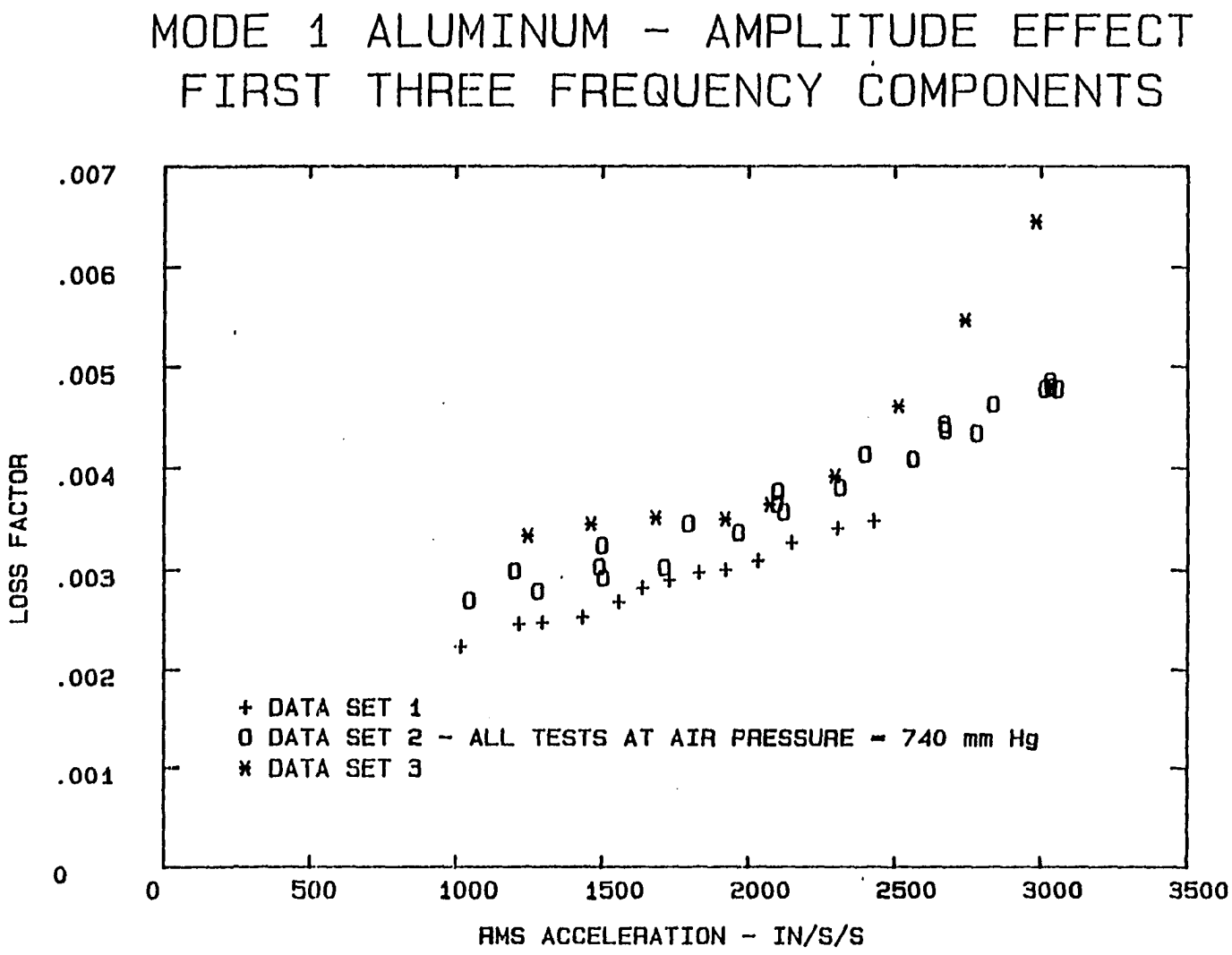

Fig. B-6. Loss factor vs acceleration amplitude, mode 1, aluminum, first three frequency components

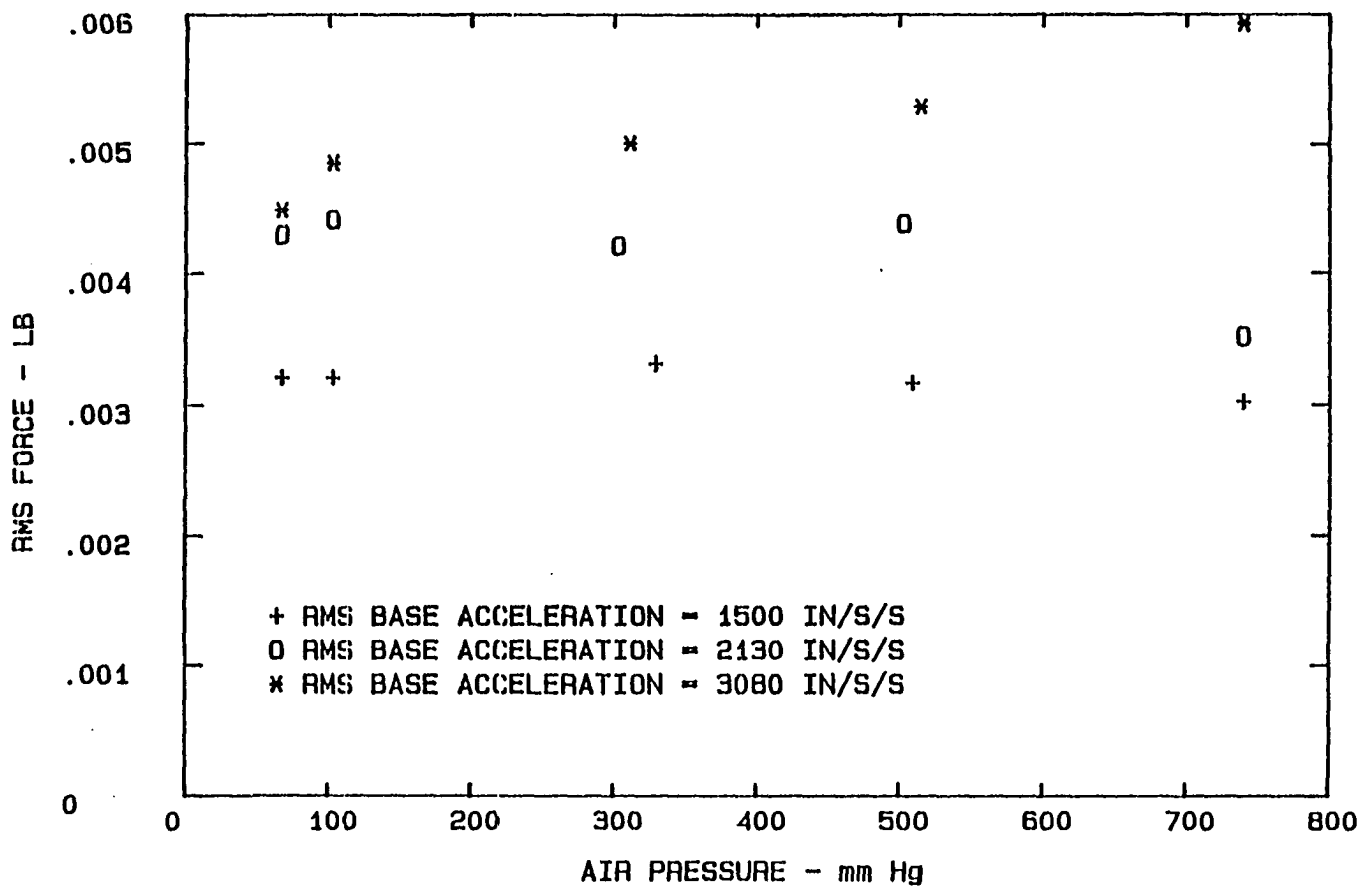

Fig. B-7. Force vs air pressure, mode 1, aluminum, first frequency component

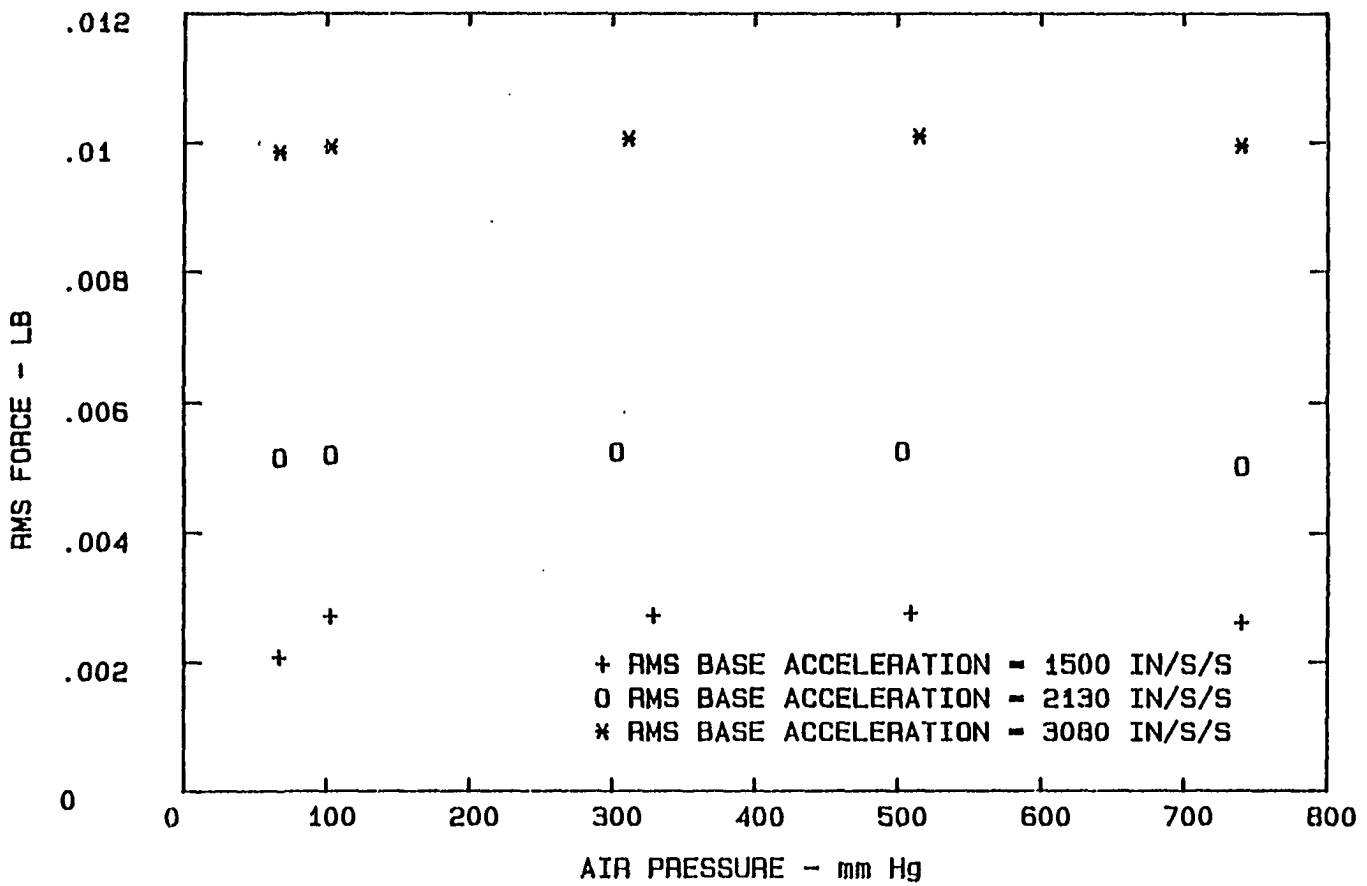

Fig. B-8. Force vs air pressure, mode 1, aluminum, second frequency component

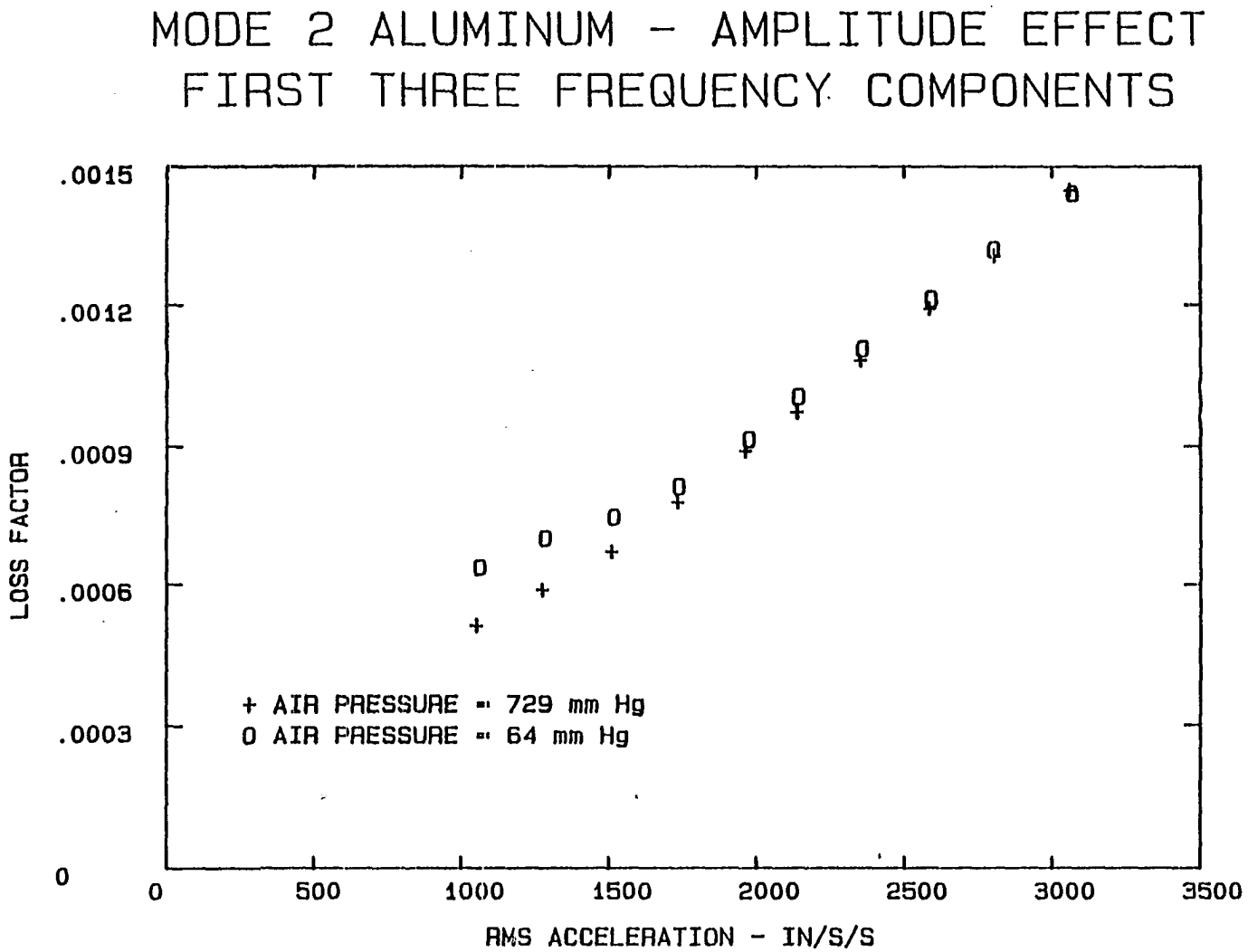

Fig. B-9. Loss factor vs acceleration amplitude, mode 2, aluminum, first three frequency components

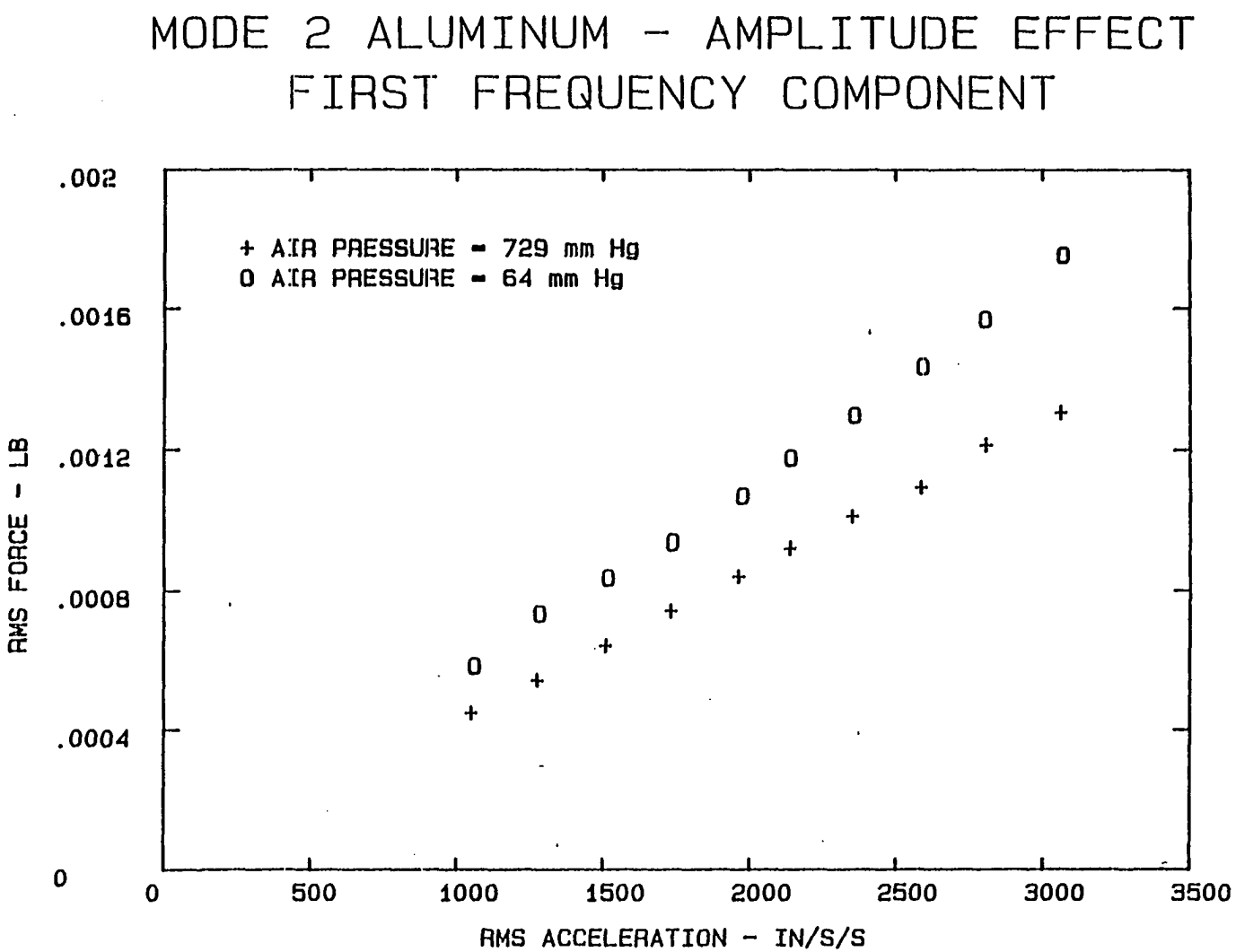

Fig. B-10. Force vs acceleration amplitude, mode 2, aluminum, first frequency component

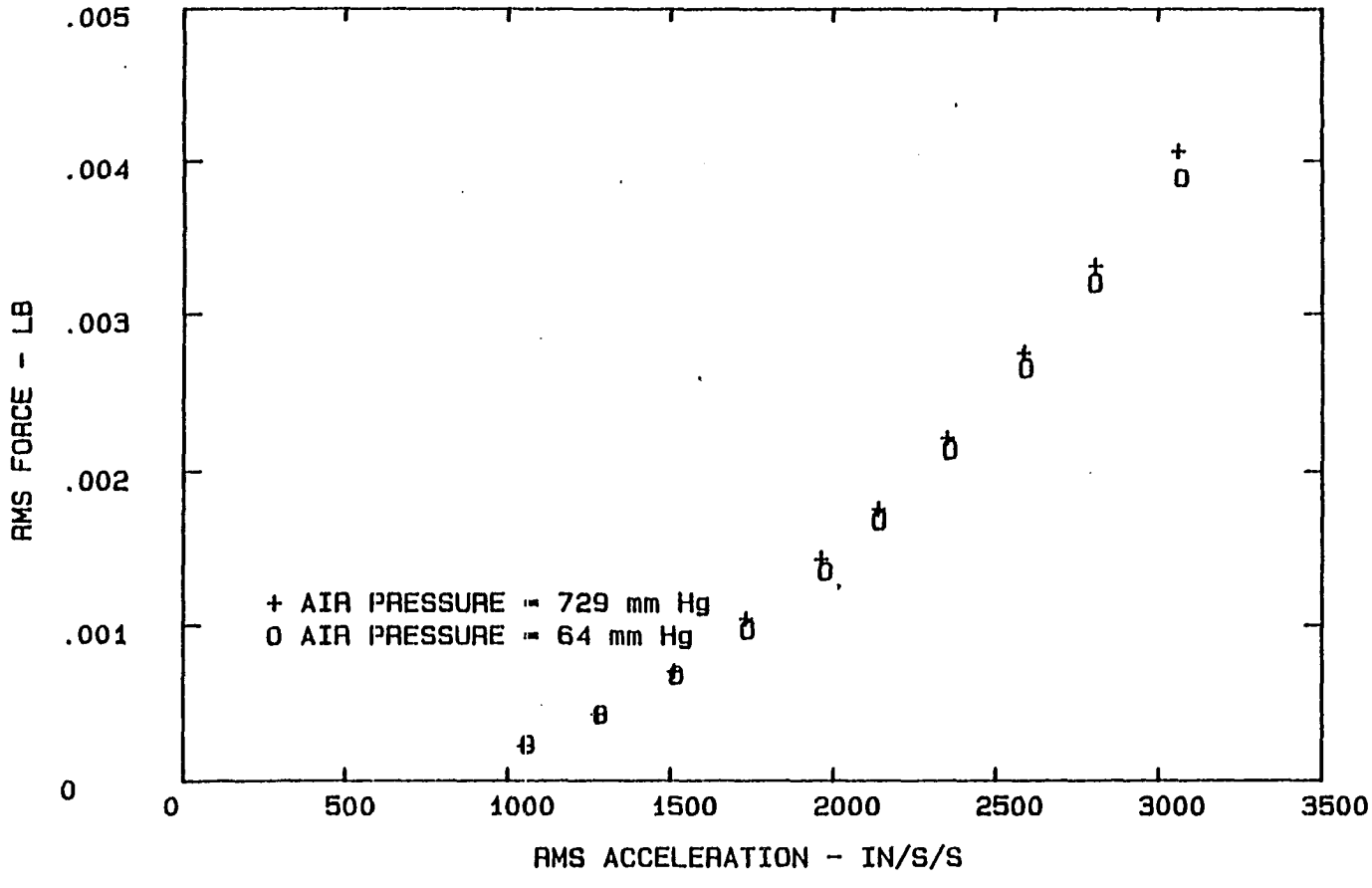

Fig. B-11. Force vs acceleration amplitude, mode 2, aluminum, second frequency component

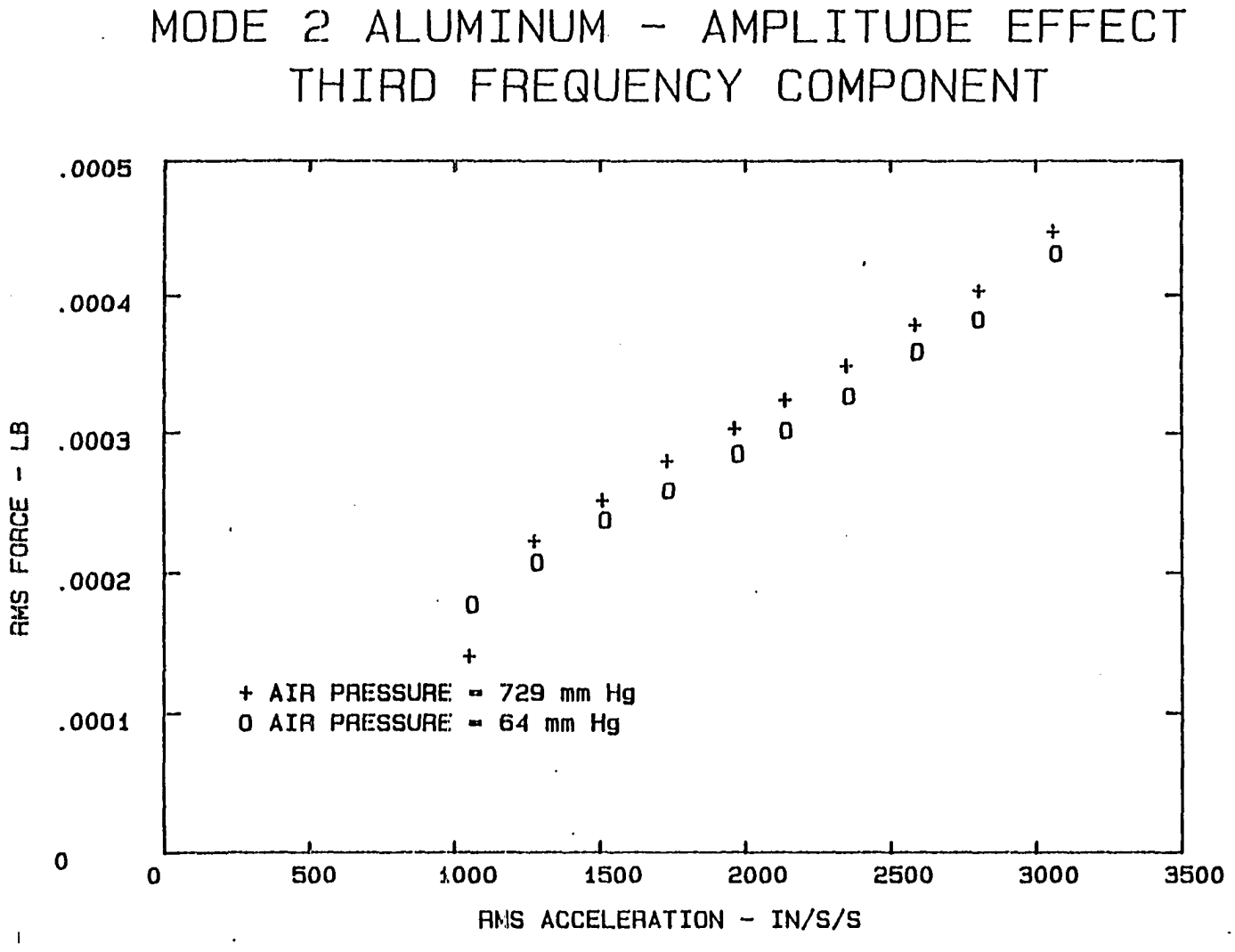

Fig. B-12. Force vs acceleration amplitude, mode 2, aluminum, third frequency component

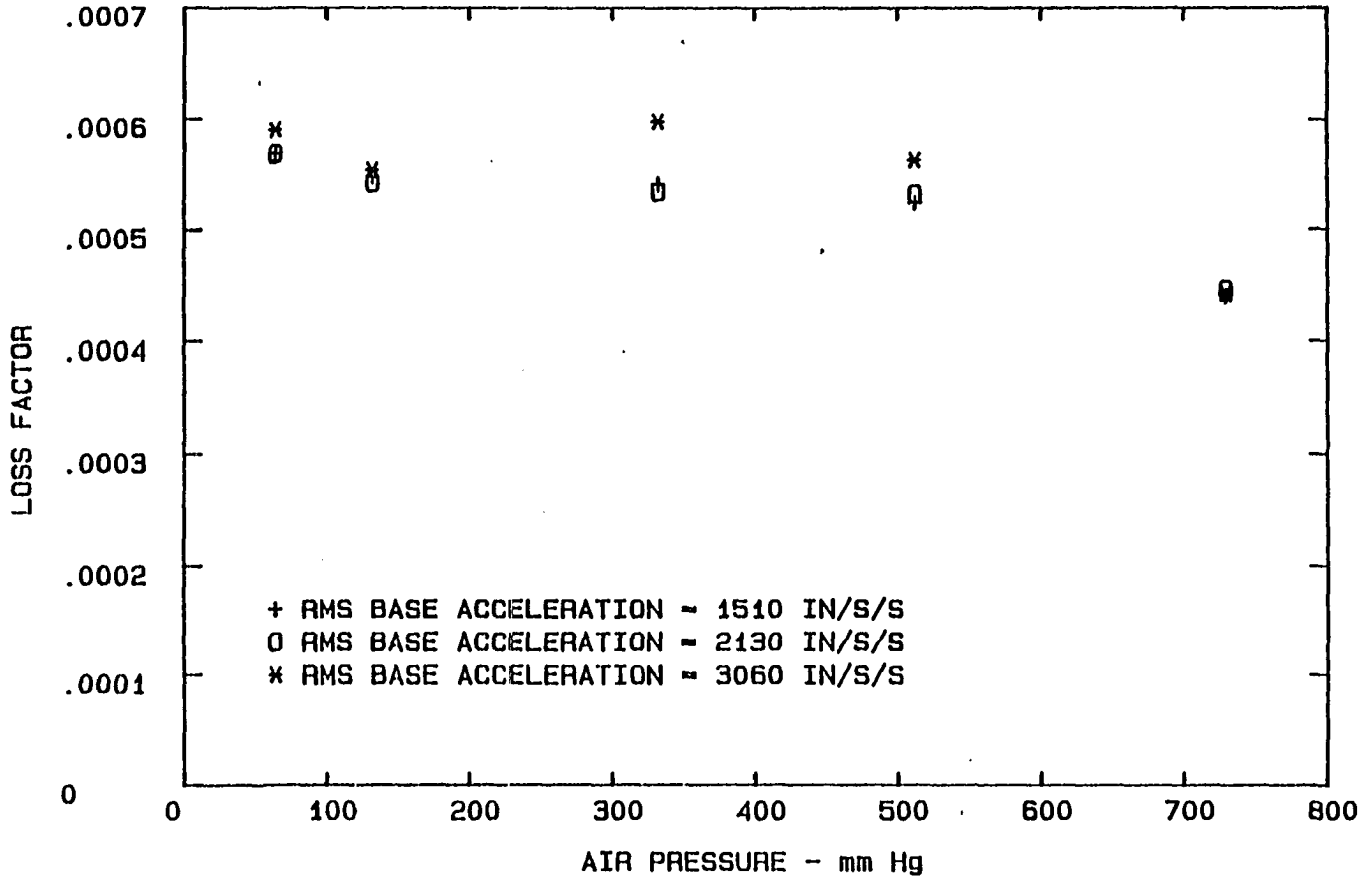

Fig. B-13. Loss factor vs air pressure, mode 2, aluminum, first frequency component

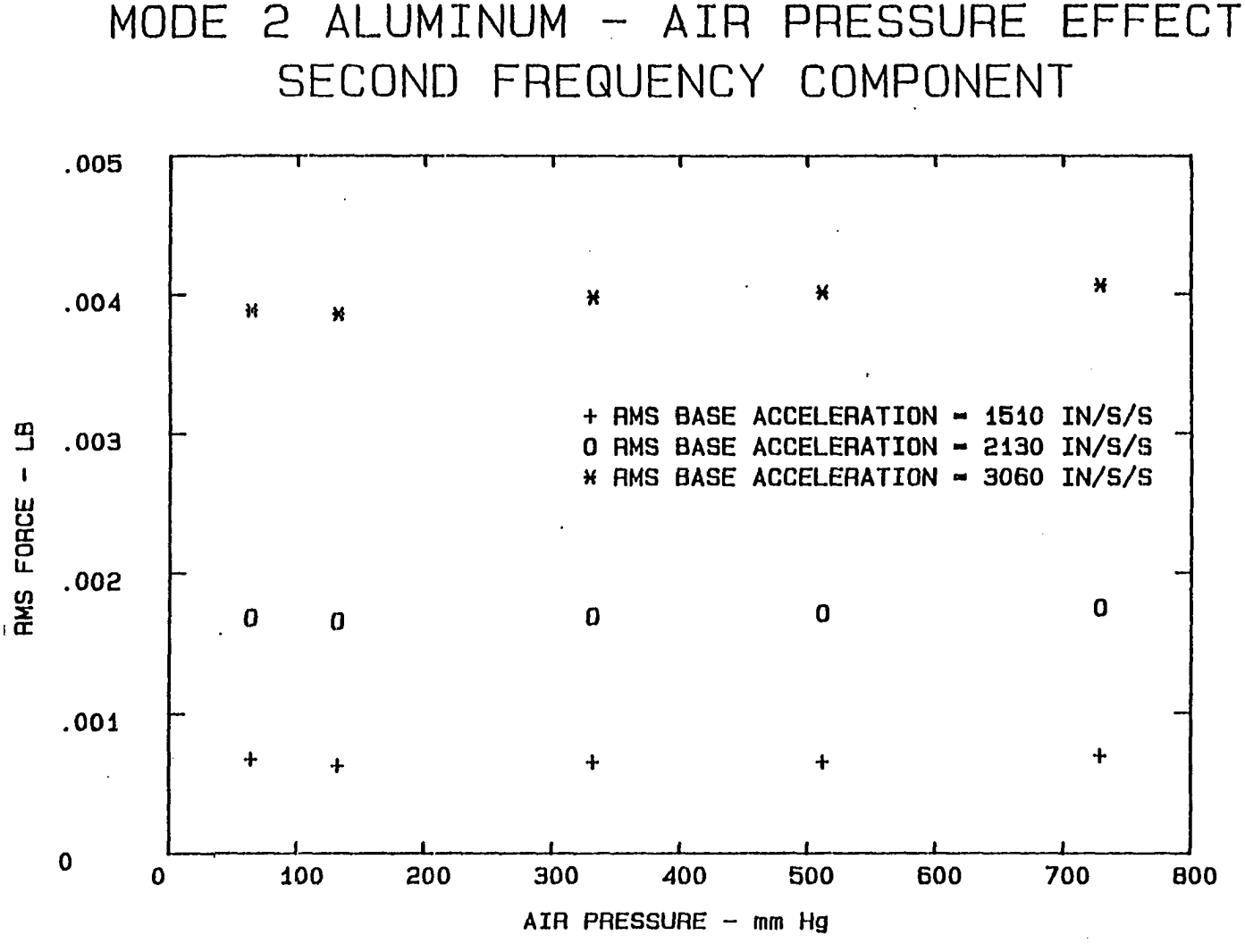

Fig. B-14. Force vs air pressure, mode 2, aluminum, second frequency component

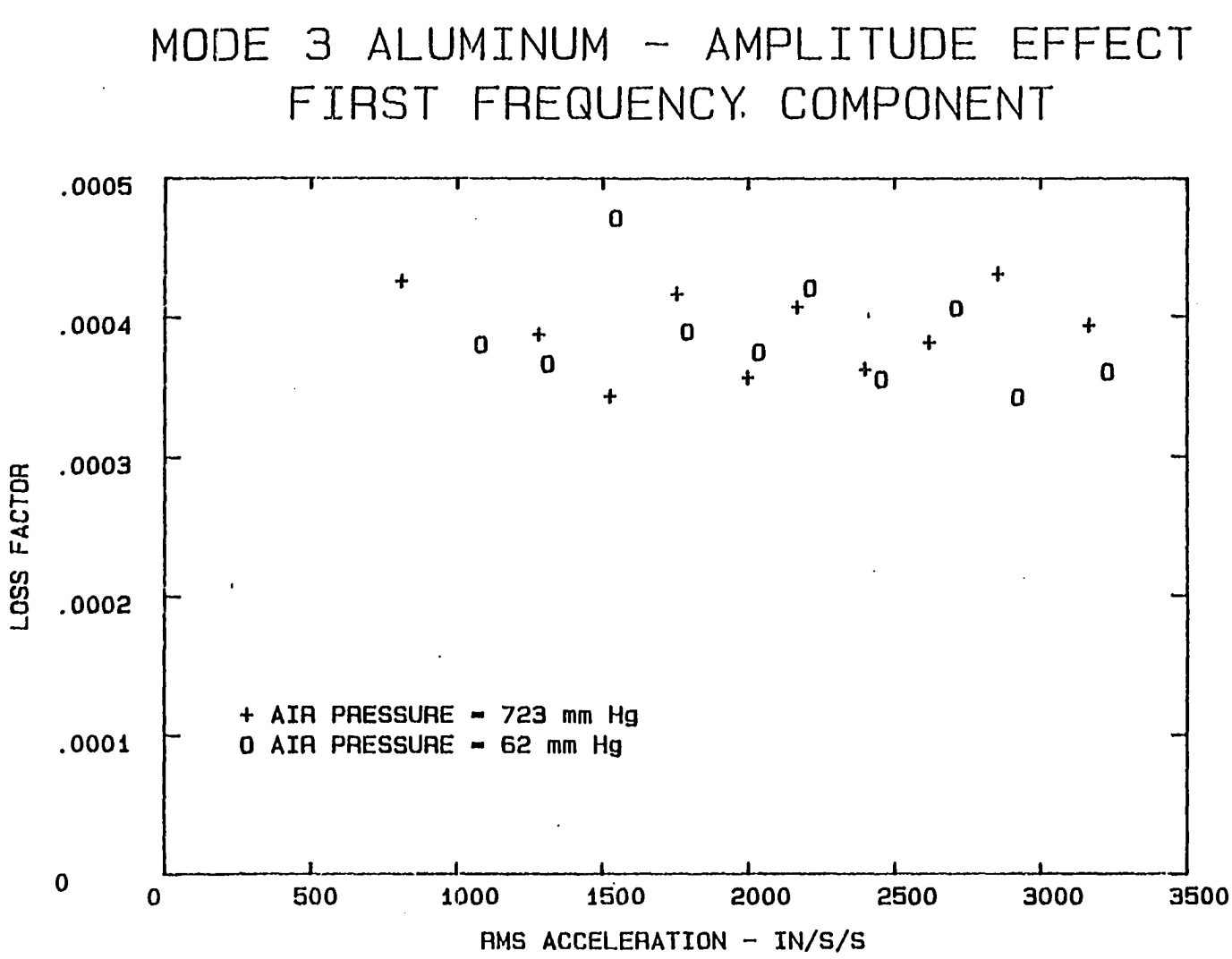

Fig. B-15. Loss factor vs acceleration amplitude, mode 3, aluminum, first frequency component

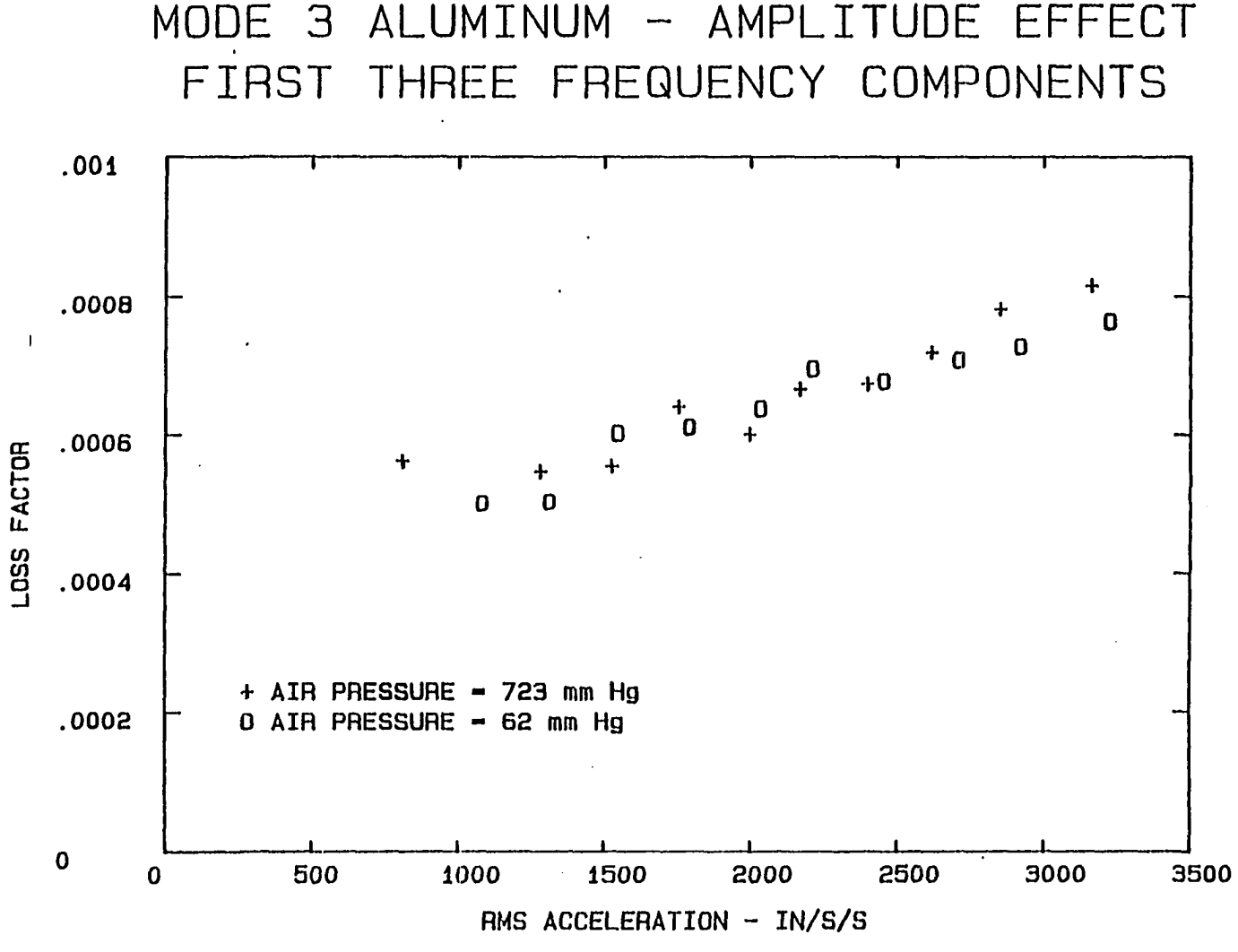

Fig. B-16. Loss factor vs acceleration amplitude, mode 3, aluminum, first three frequency components

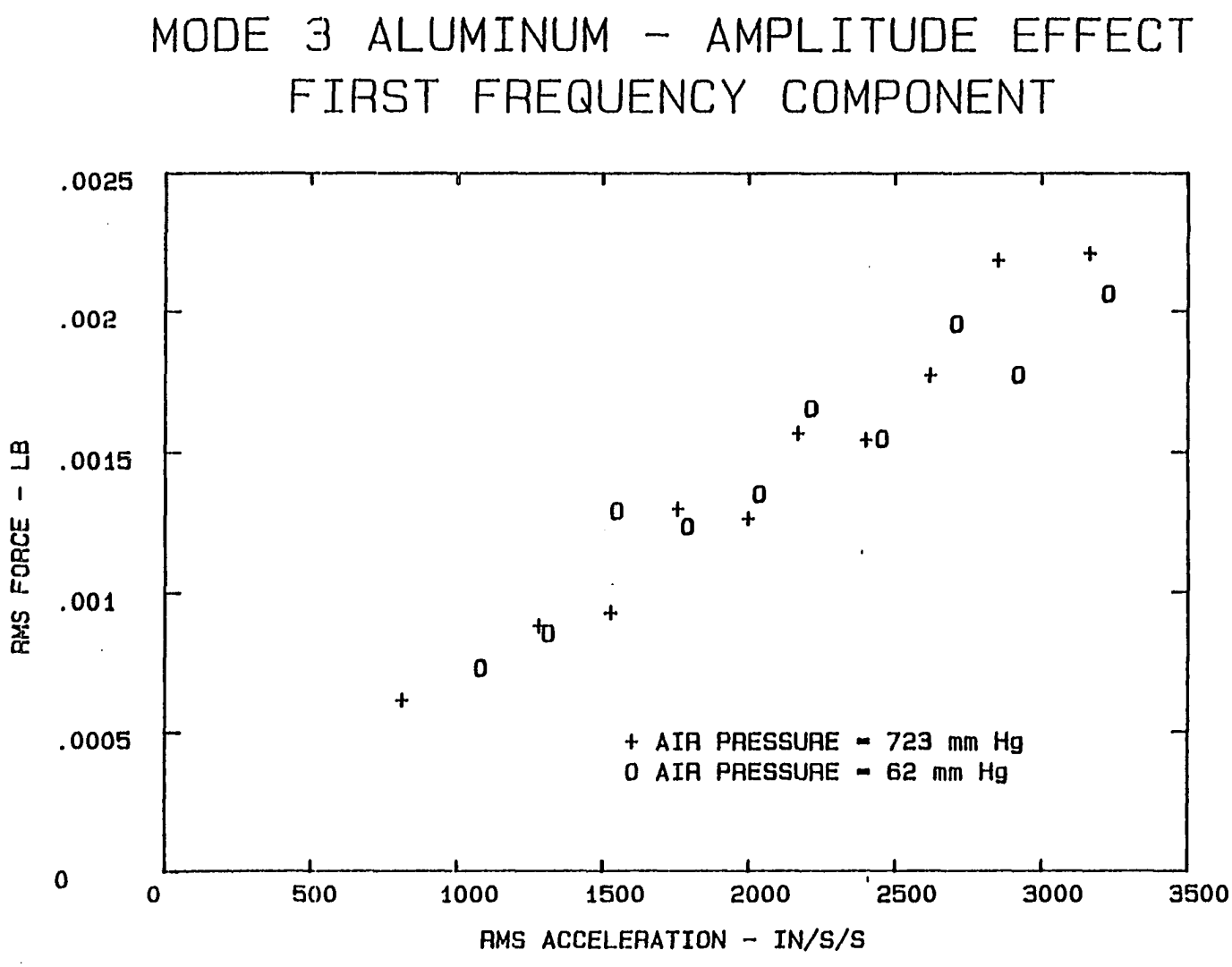

Fig. B-17. Force vs acceleration amplitude, mode 3, aluminum, first frequency component

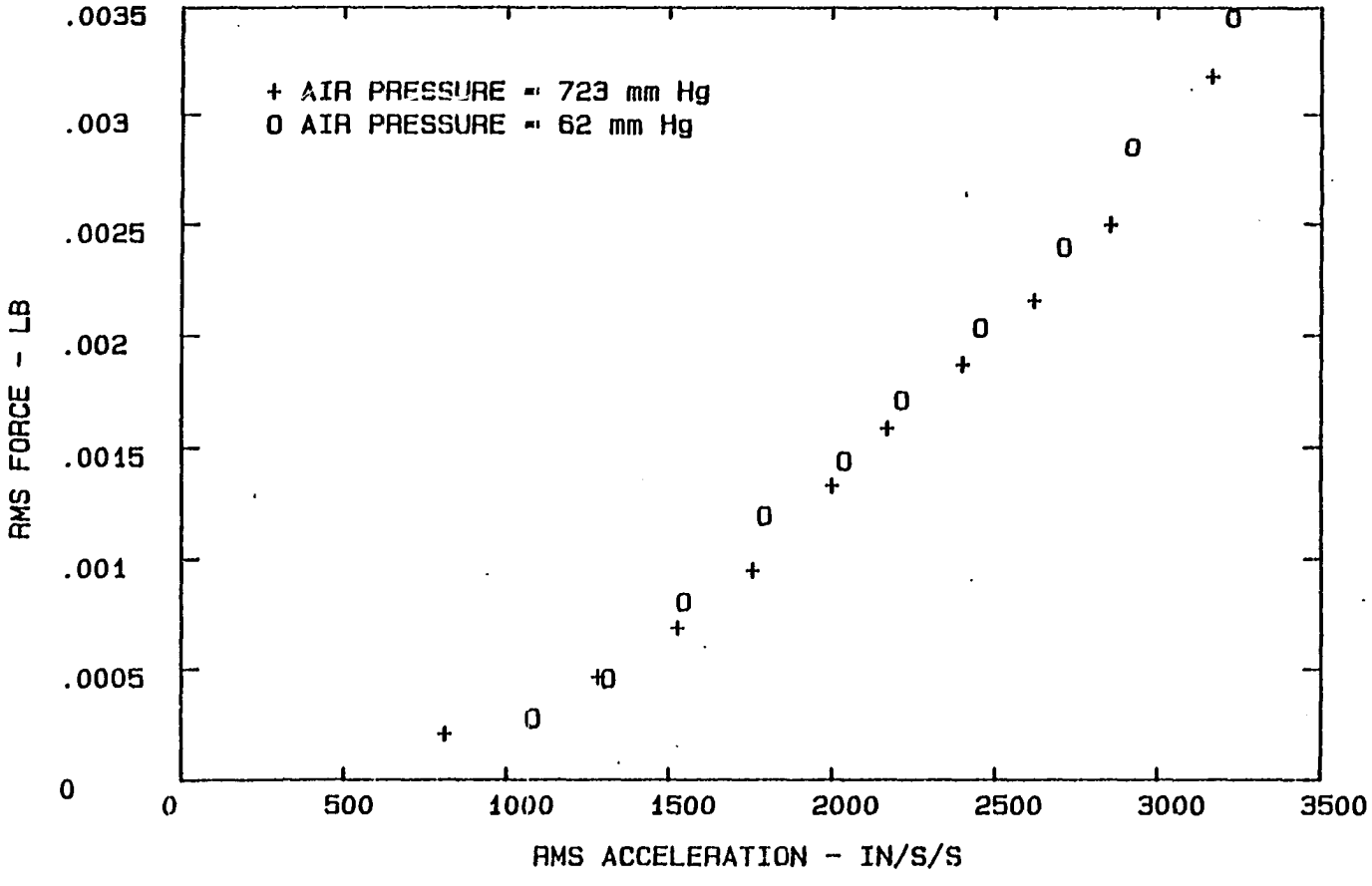

Fig. B-18. Force vs acceleration amplitude, mode 3, aluminum, second frequency component

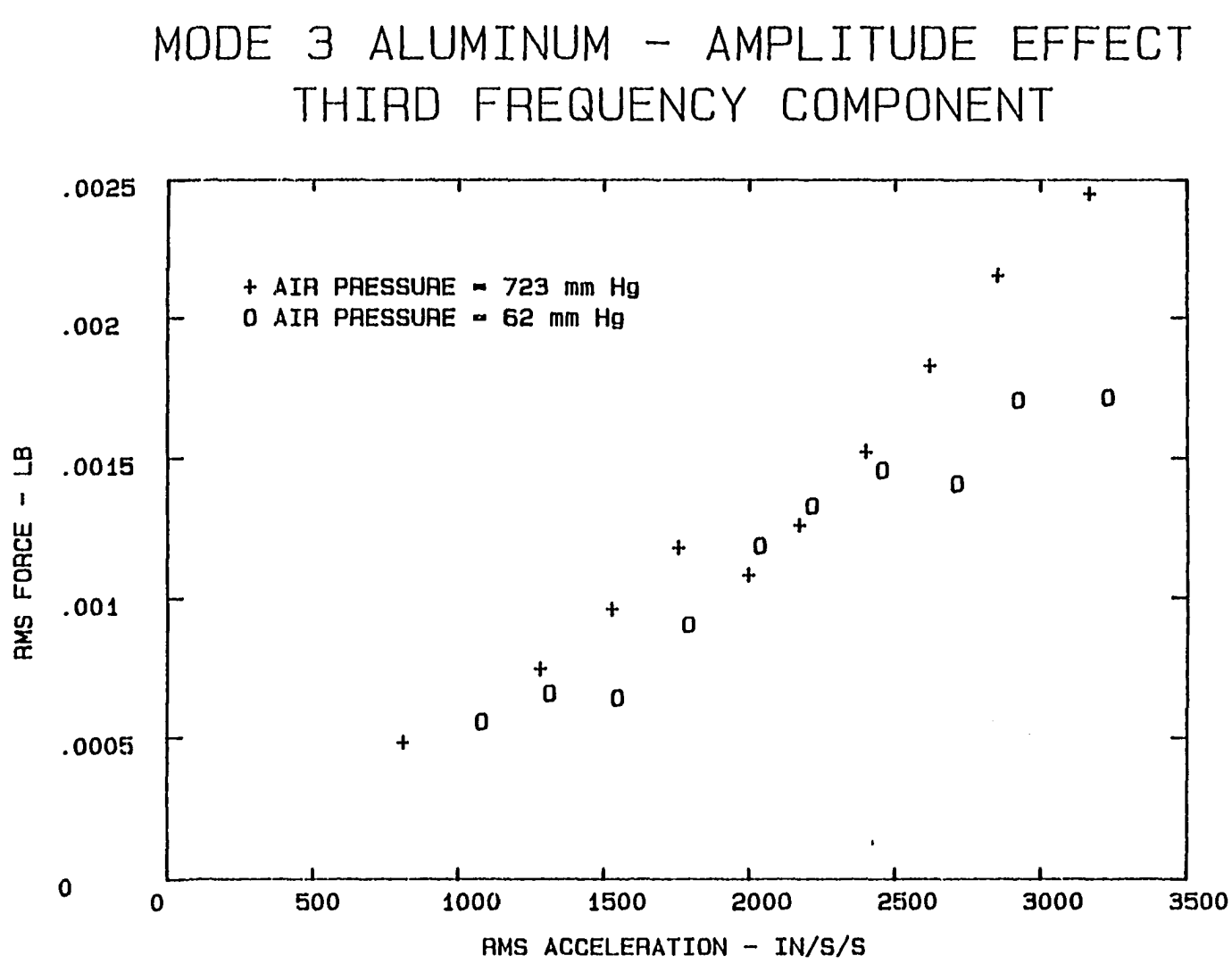

Fig. B-19. Force vs acceleration amplitude, mode 3, aluminum, third frequency component

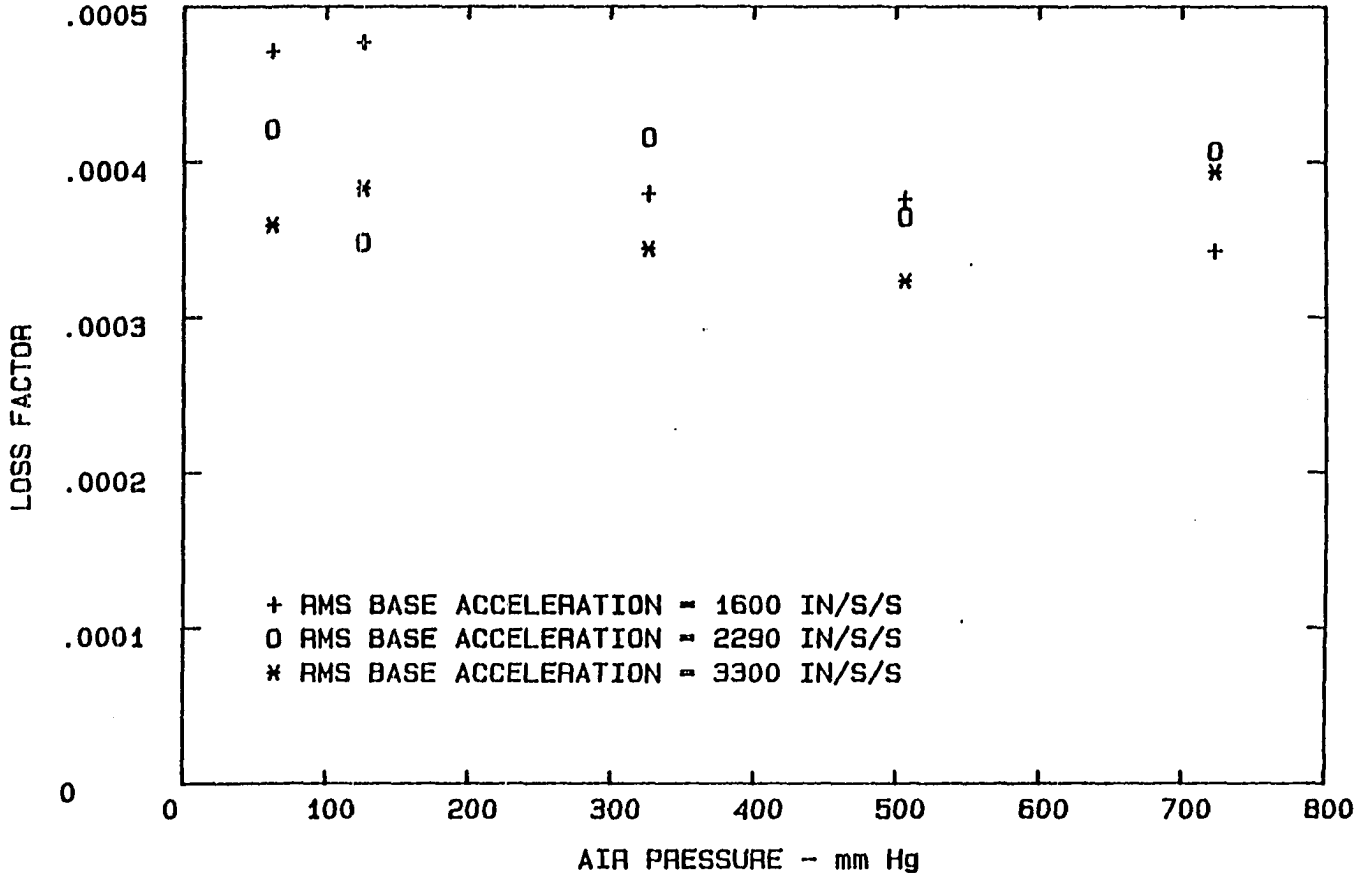

Fig. B-20. Loss factor vs air pressure, mode 3, aluminum, first frequency component

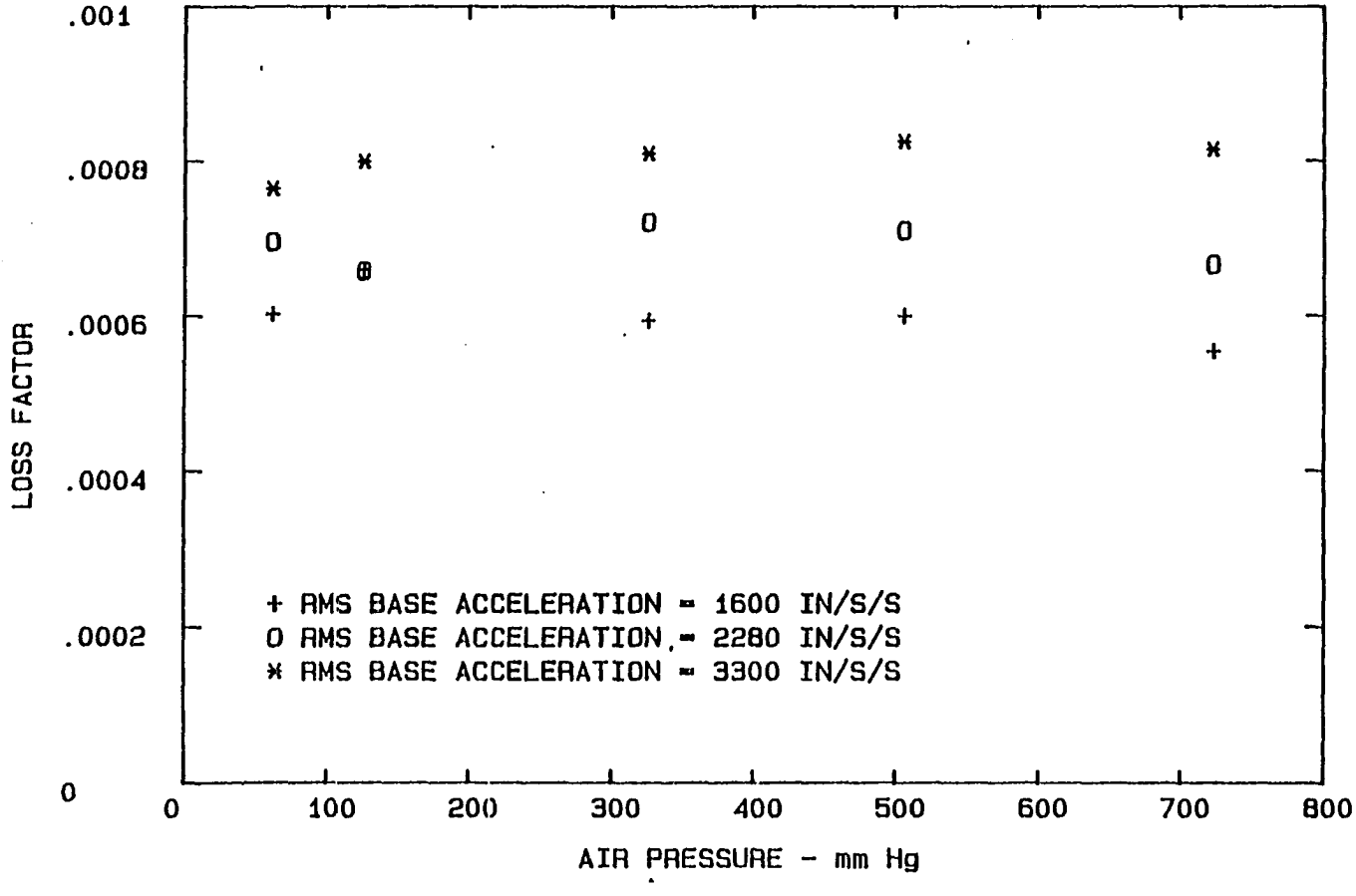

Fig. B-21. Loss factor vs air pressure, mode 3, aluminum, first three frequency components

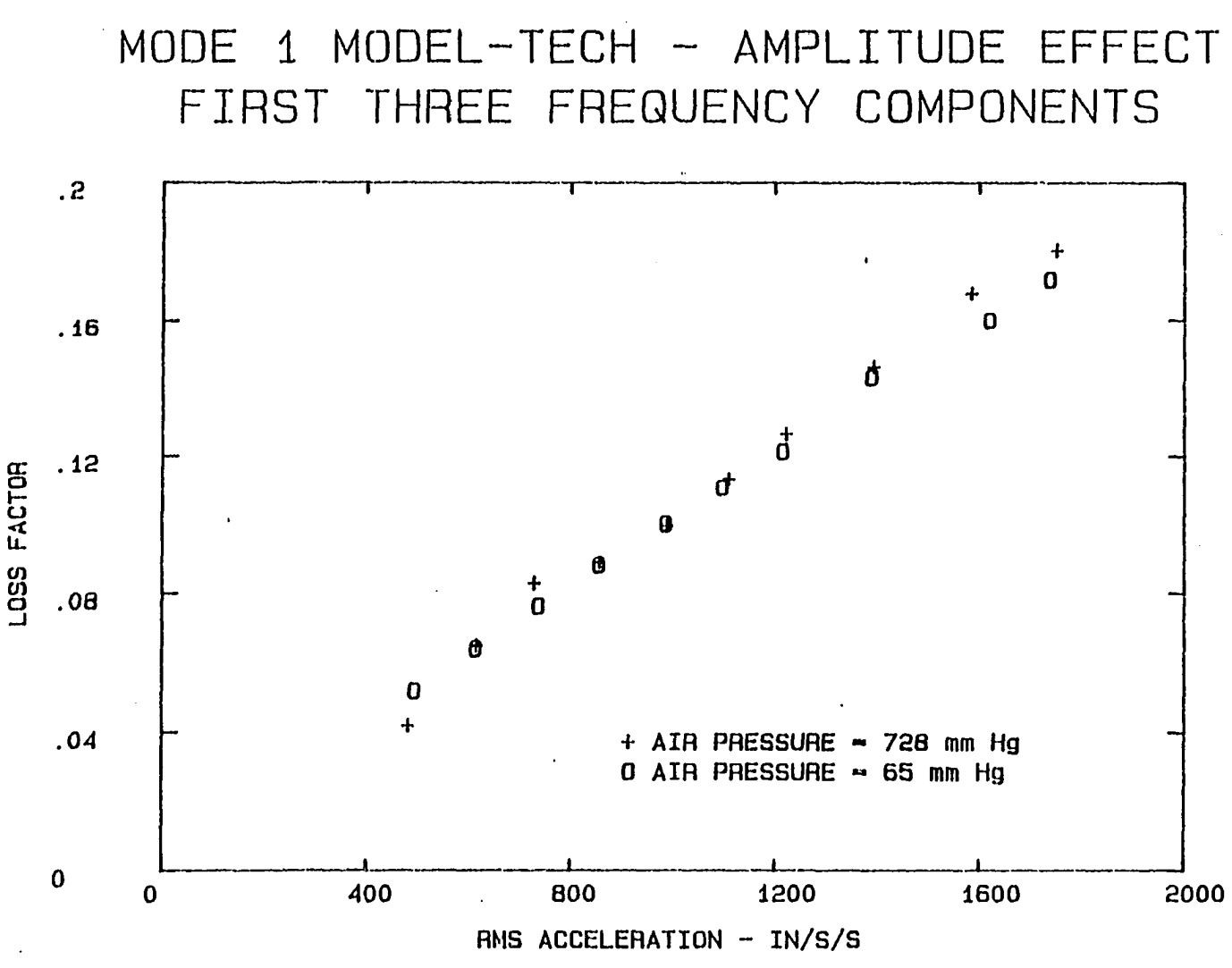

Fig. B-22. Loss factor vs acceleration amplitude, mode 1, Model-Tech, first three frequency components

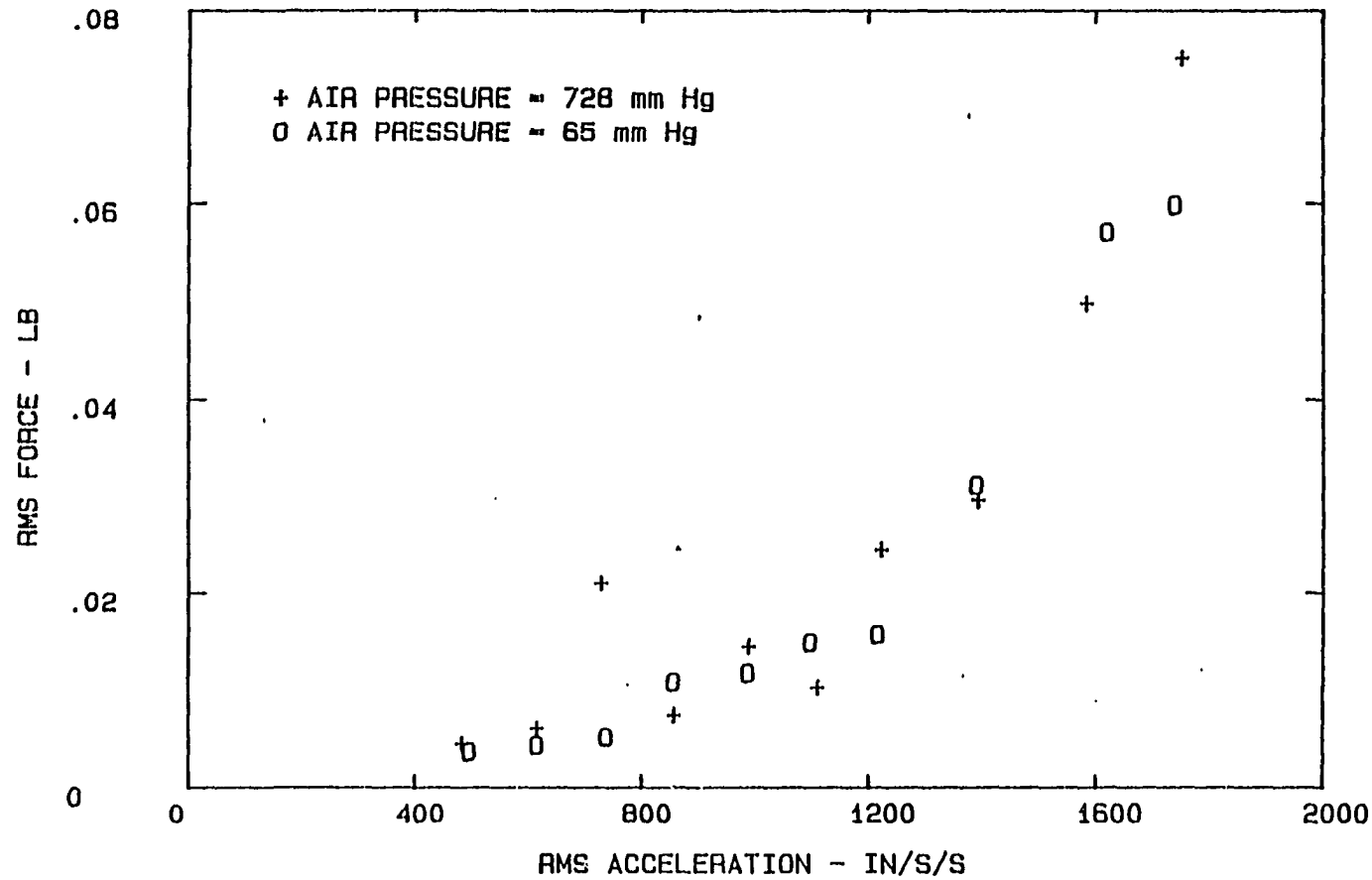

Fig. B-23. Force vs acceleration amplitude, mode 1, Model-Tech, first frequency component

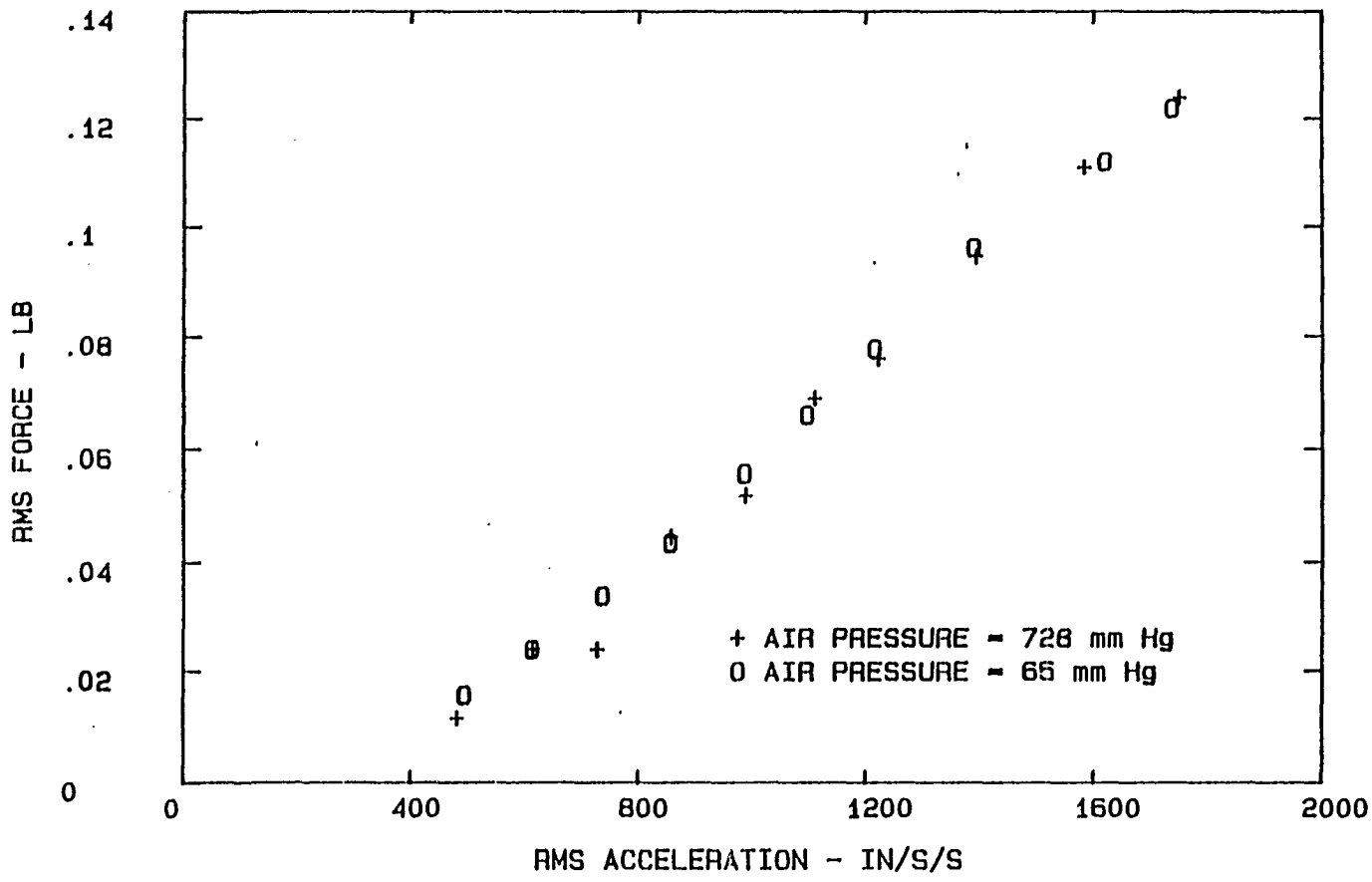

Fig. B-24. Force vs acceleration amplitude, mode 1, Model-Tech, second frequency component

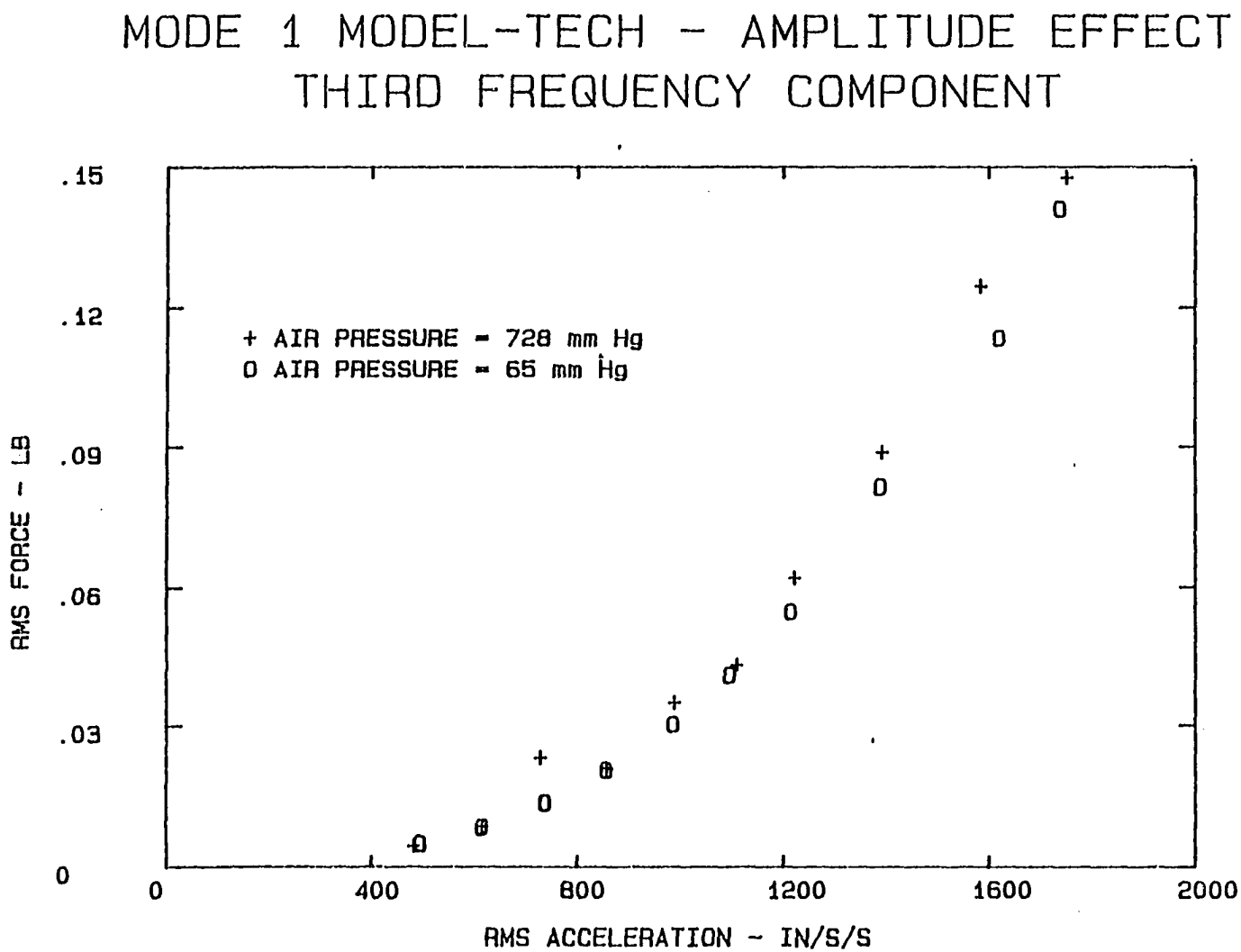

Fig. B-25. Force vs acceleration amplitude, mode 1, Model-Tech, third frequency component

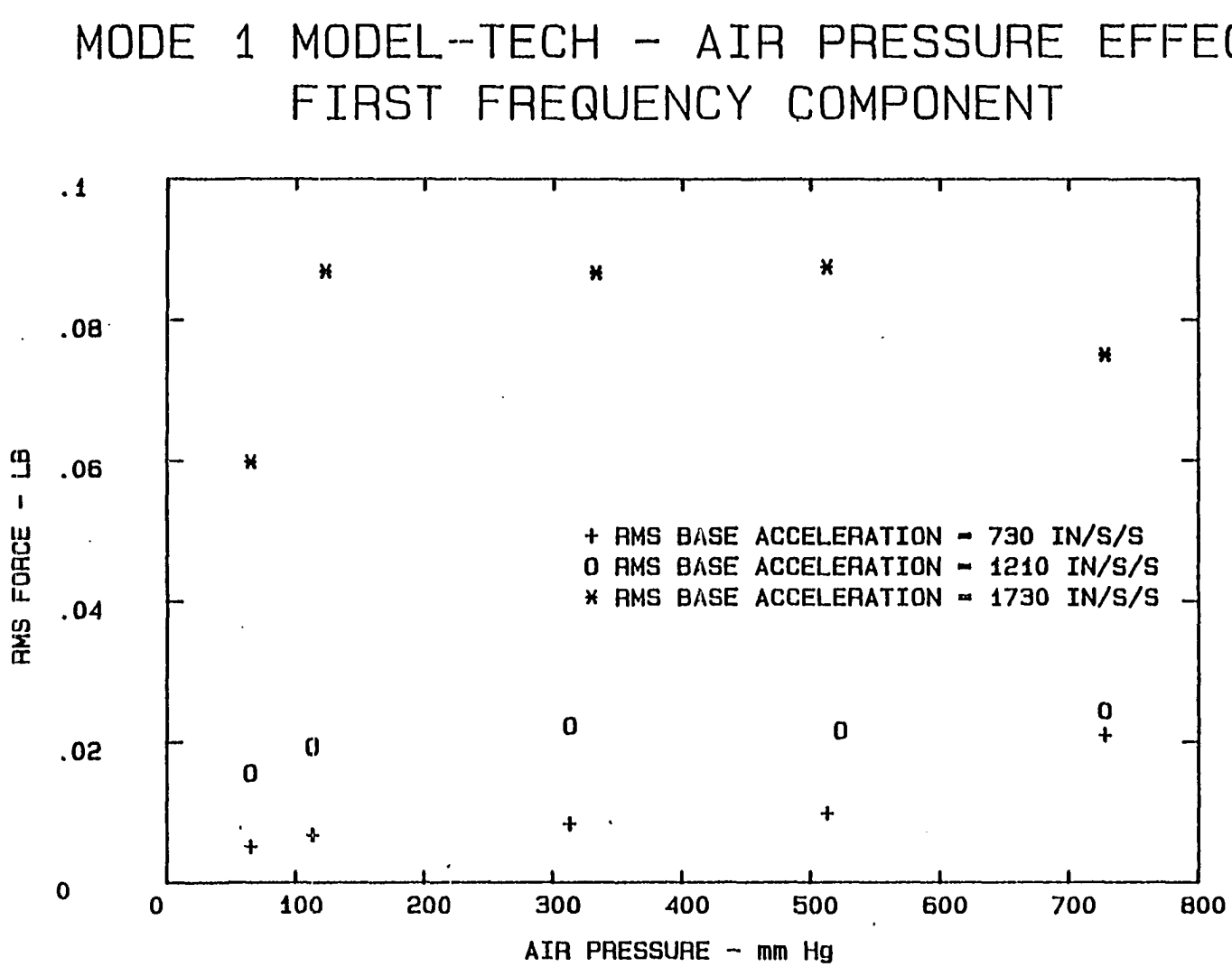

Fig. B-26. Force vs air pressure, mode 1, Model-Tech, first frequency component

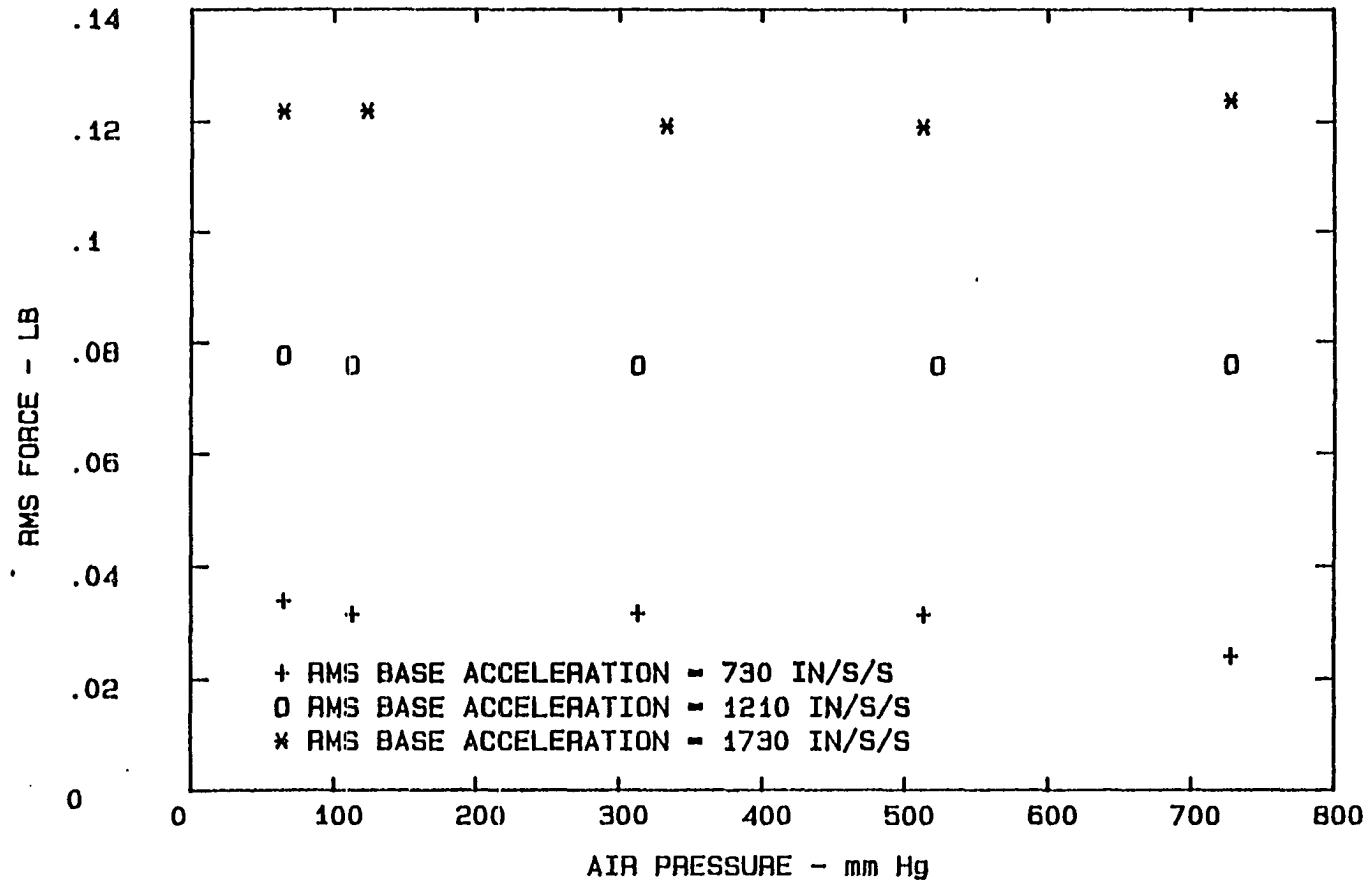

Fig. B-27. Force vs air pressure, mode 1, Model-Tech, second frequency component

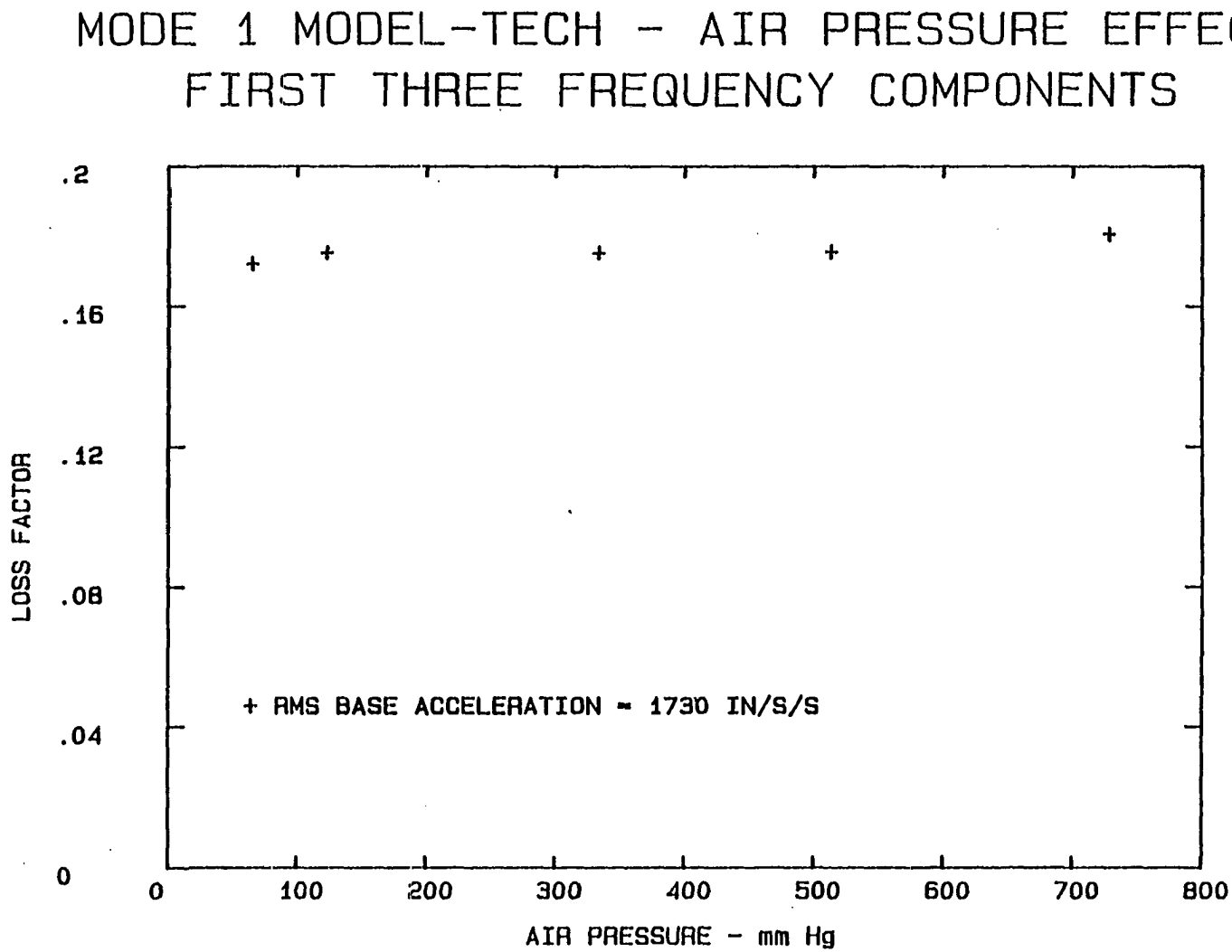

Fig. B-28. Loss factor vs air pressure, mode 1, Model-Tech, first three frequency components

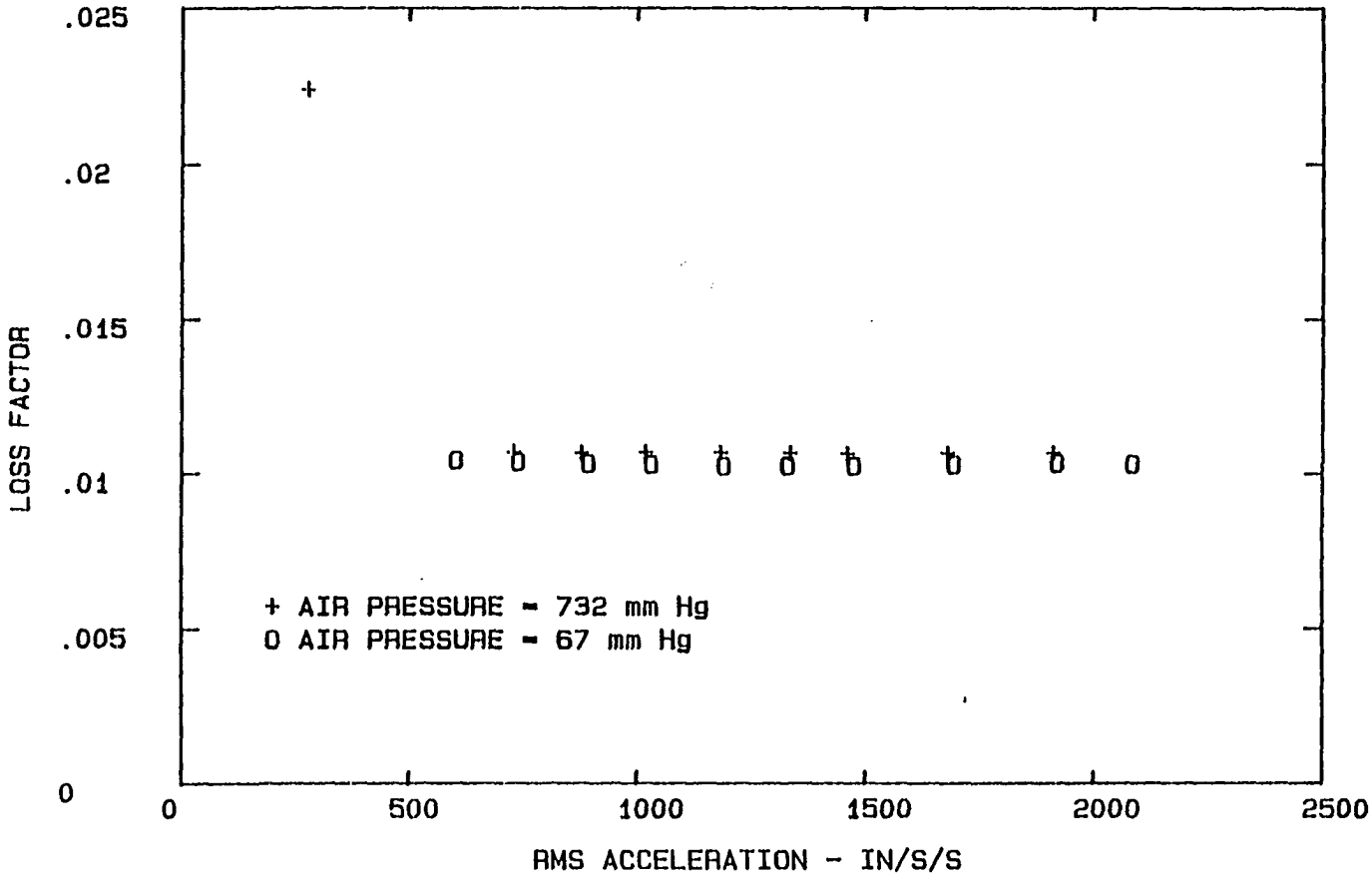

Fig. B-29. Loss factor vs acceleration amplitude, mode 2, Model-Tech, first three frequency components

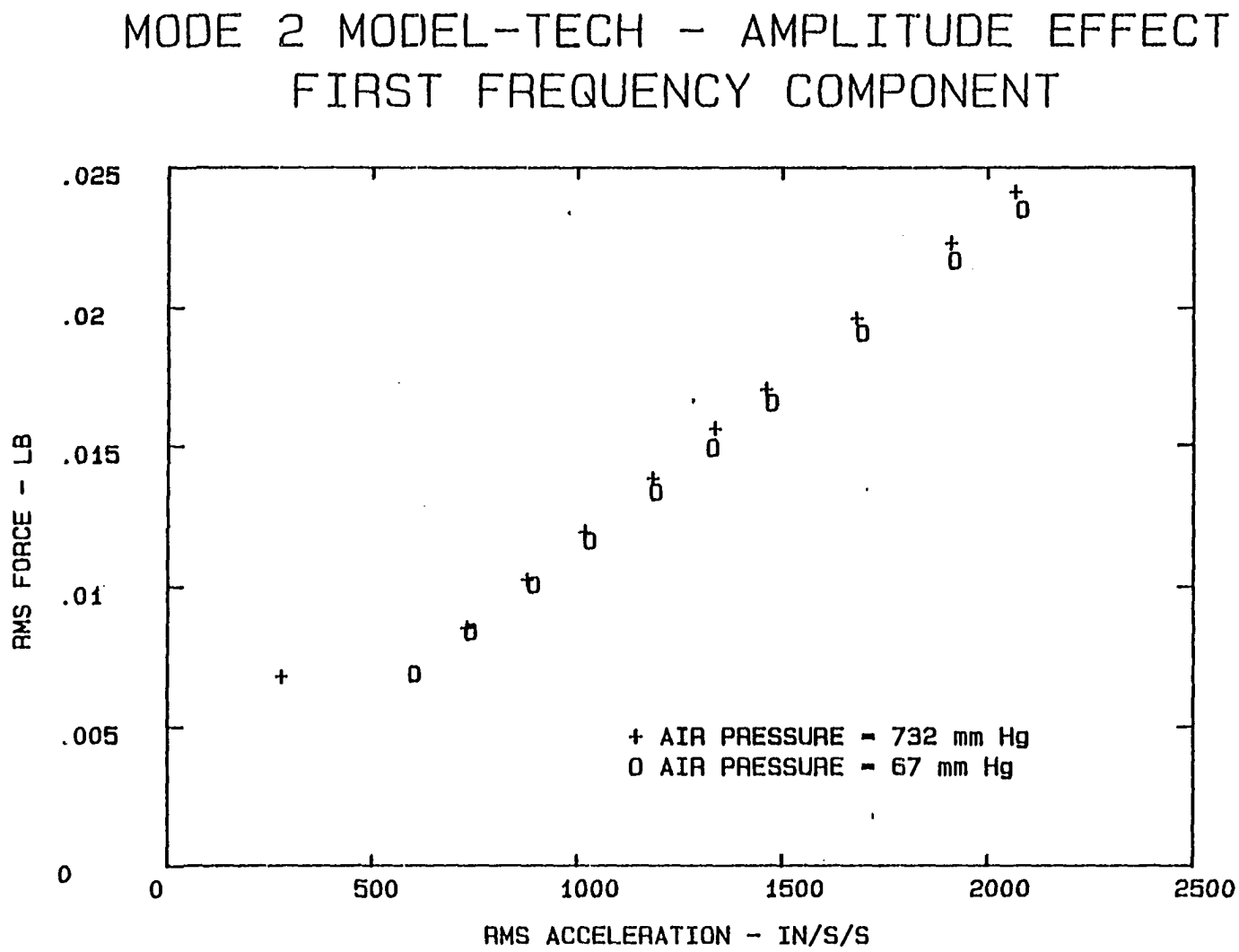

Fig. B-30. Force vs acceleration amplitude, mode 2, Model-Tech, first frequency component

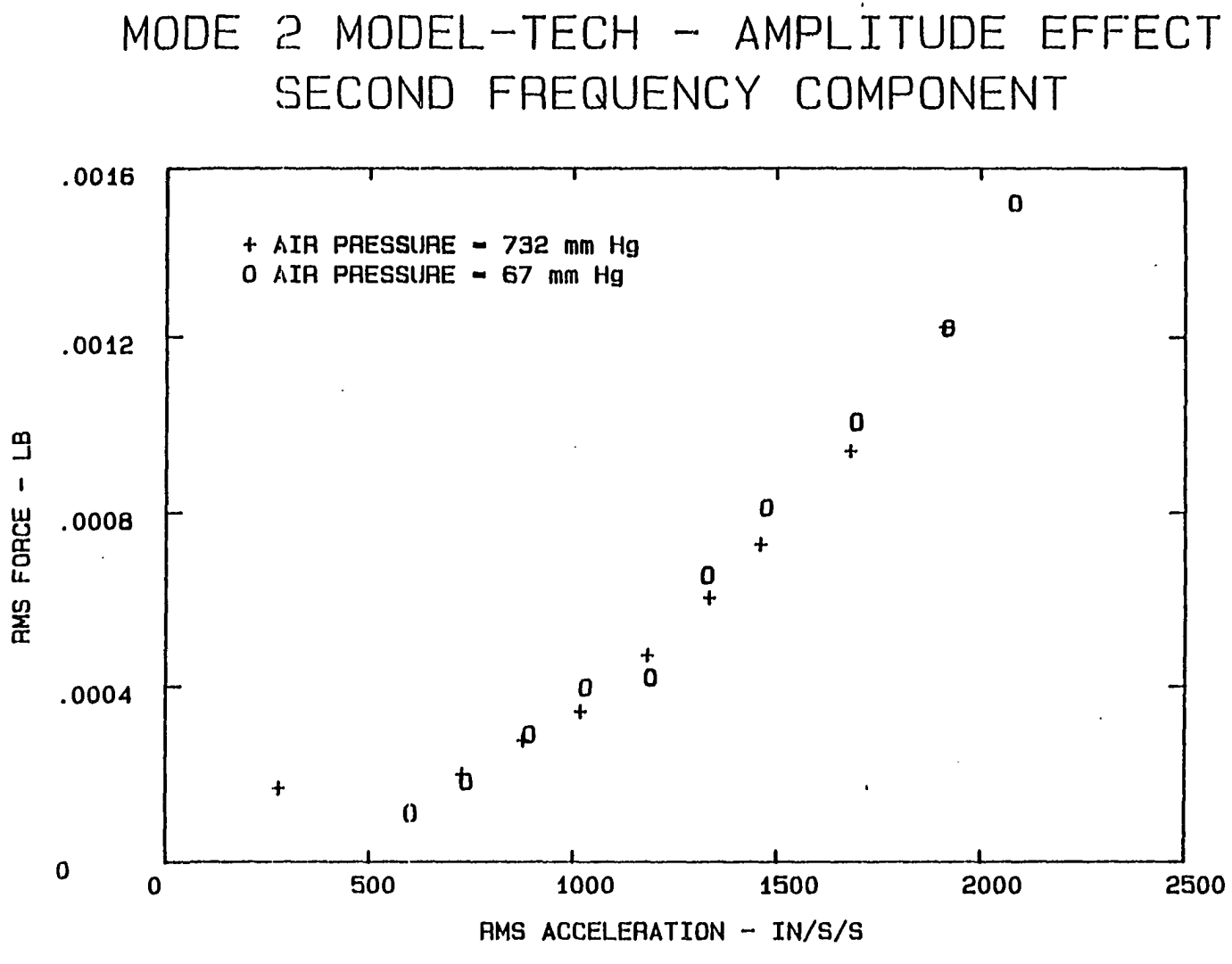

Fig. B-31. Force vs acceleration amplitude, mode 2, Model-Tech, second frequency component

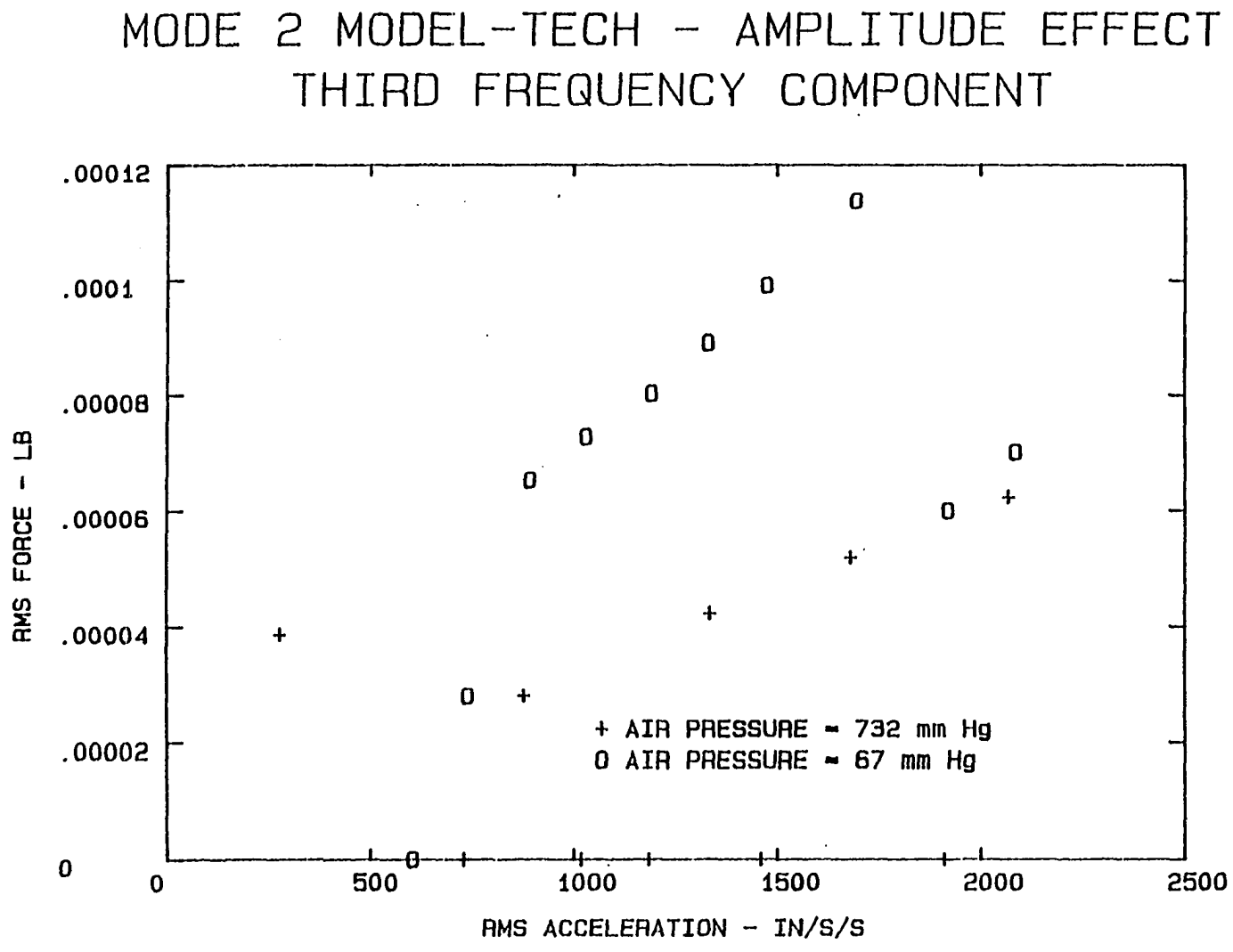

Fig. B-32. Force vs acceleration amplitude, mode 2, Model-Tech, third frequency component

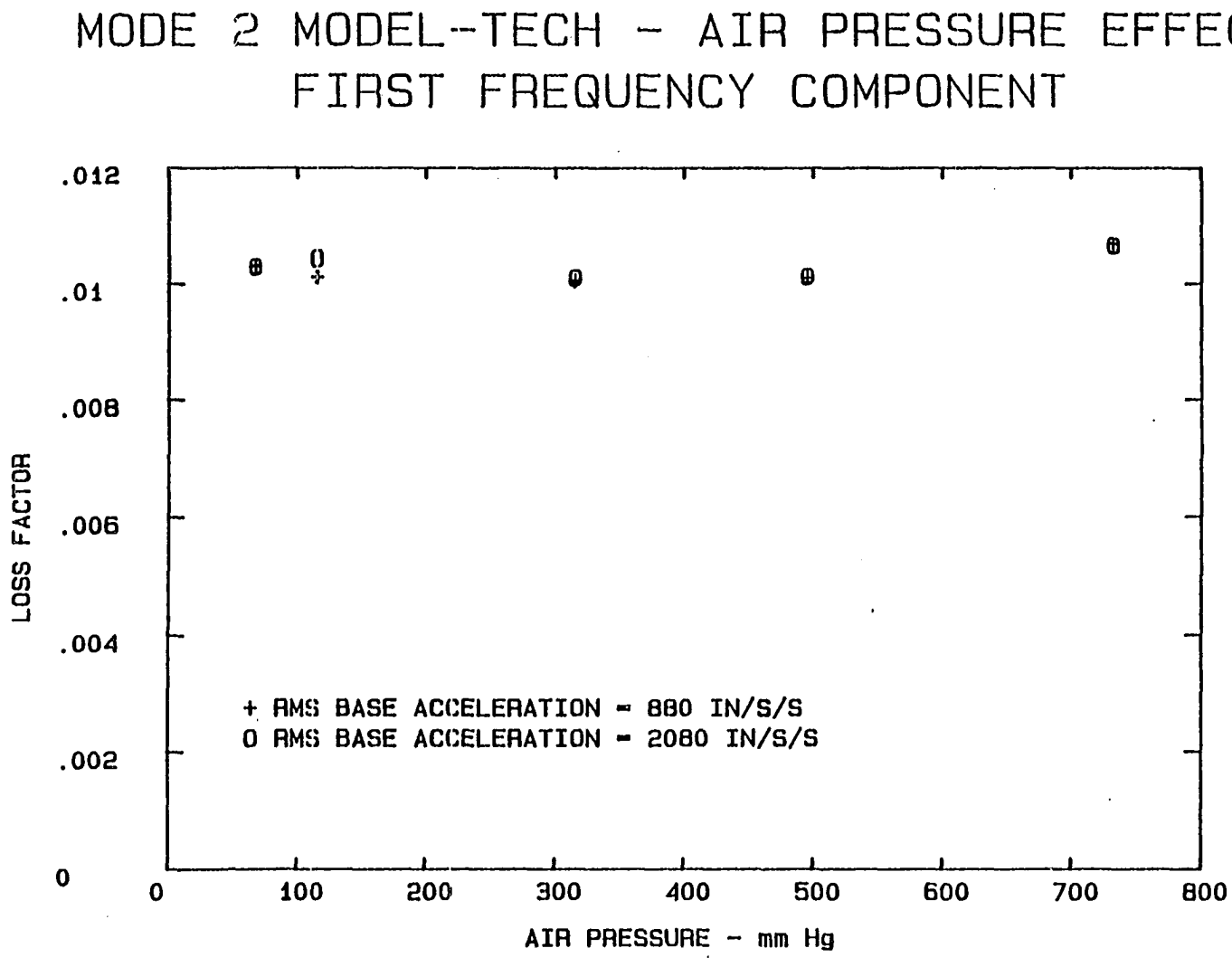

Fig. B-33. Loss factor vs air pressure, mode 2, Model-Tech, first frequency component

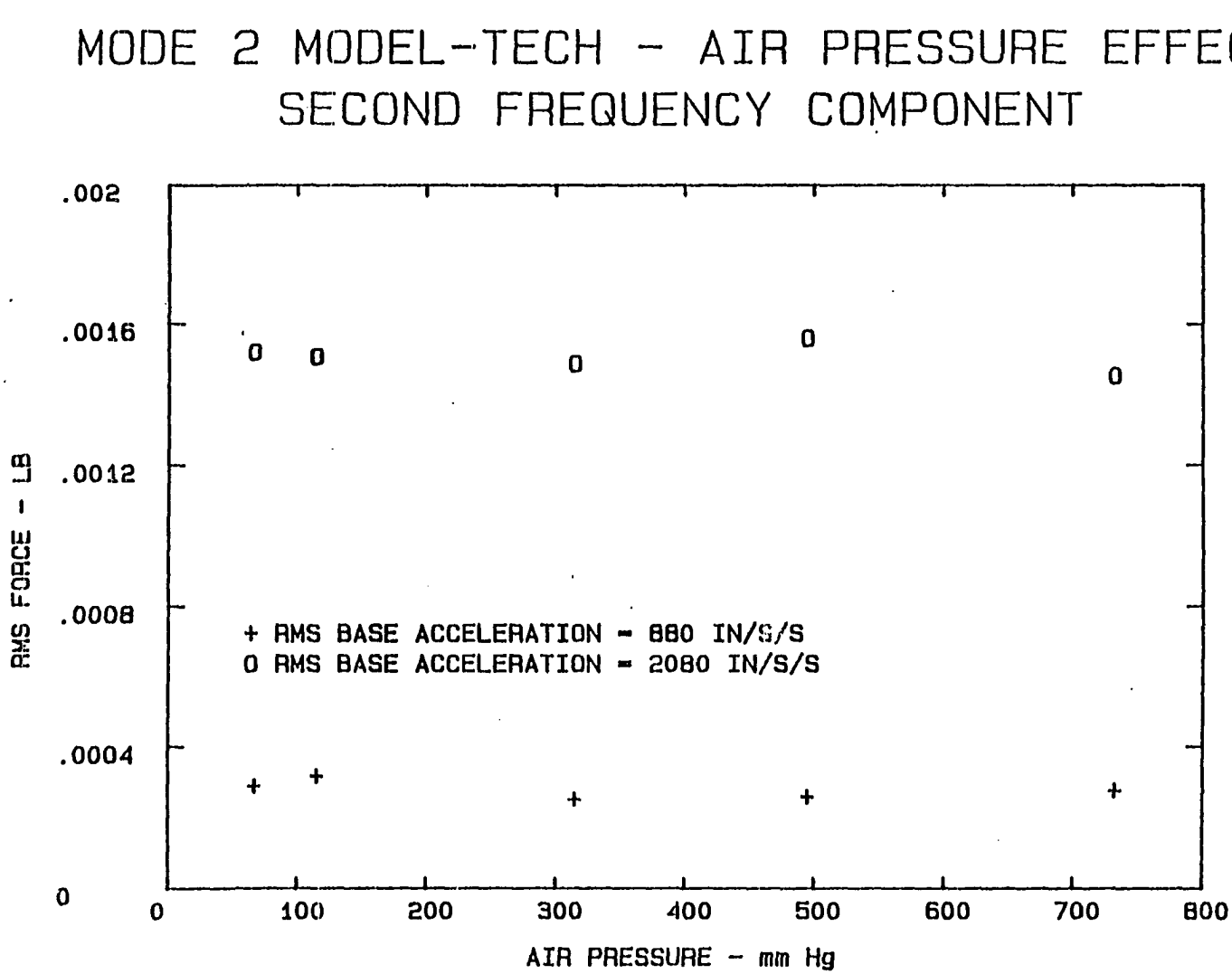

Fig. B-34. Force vs air pressure, mode 2, Model-Tech, second frequency component

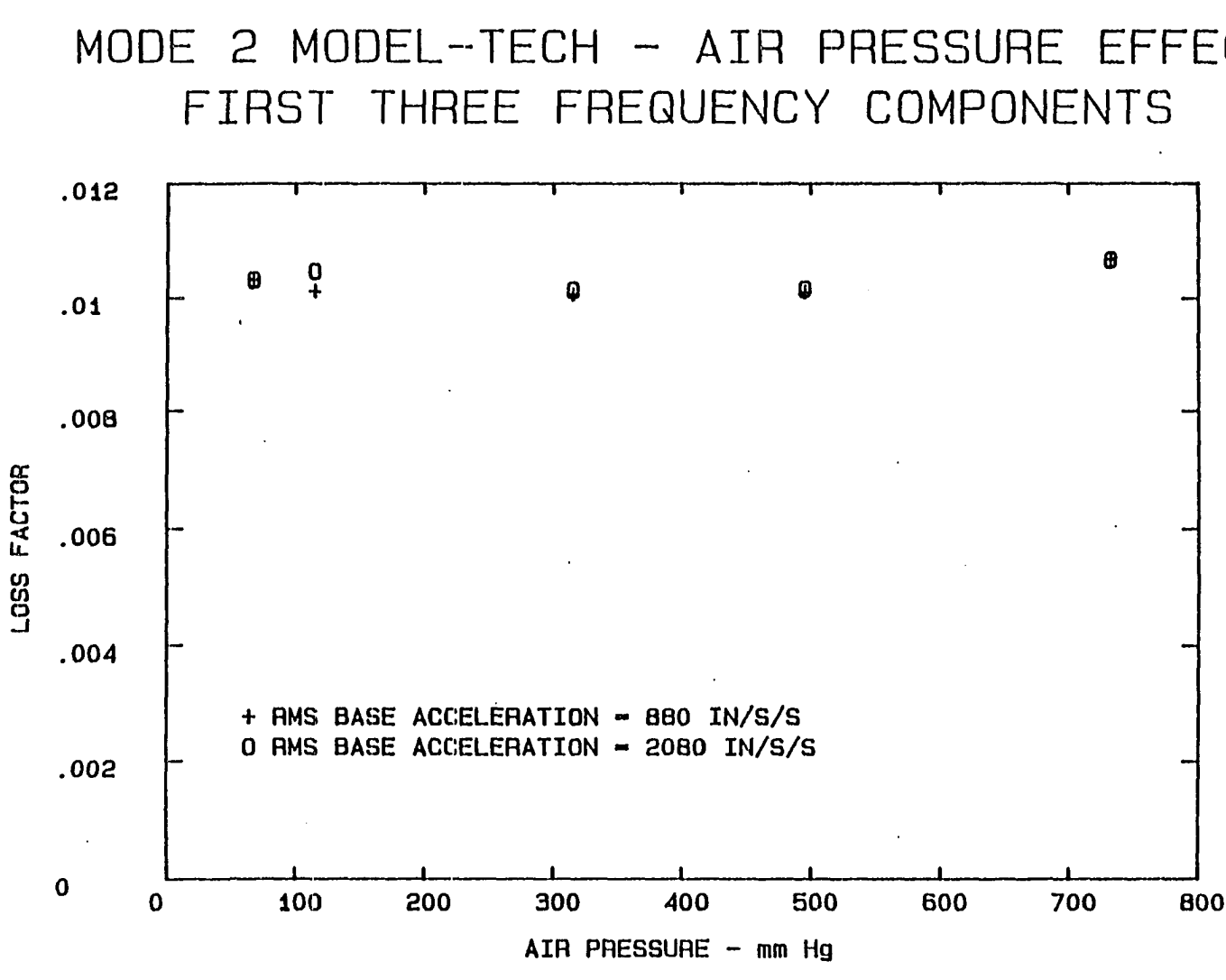

Fig. B-35. Loss factor vs air pressure, mode 2, Model-Tech, first three frequency components

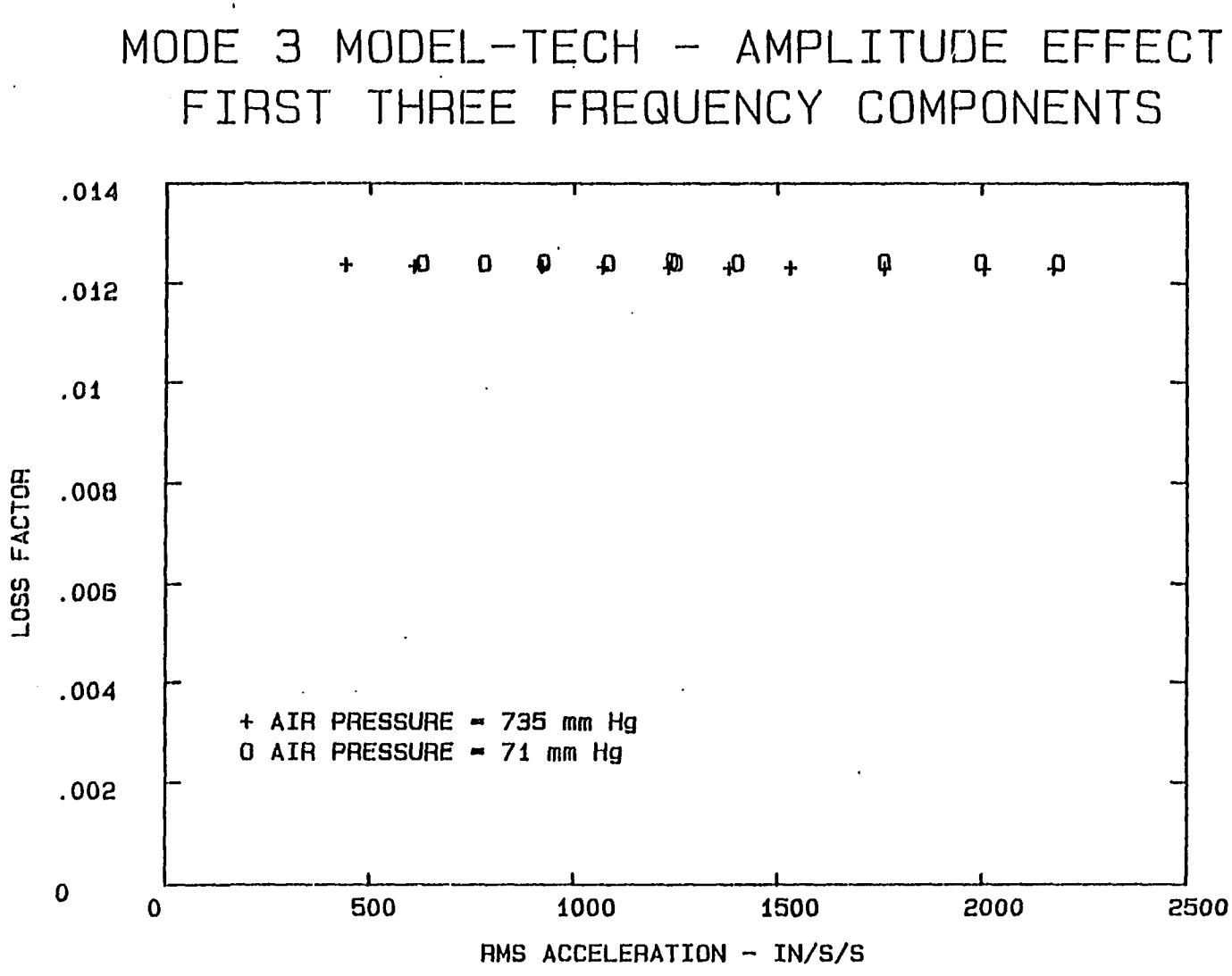

Fig. B-36. Loss factor vs acceleration amplitude, mode 3, Model-Tech, first three frequency components

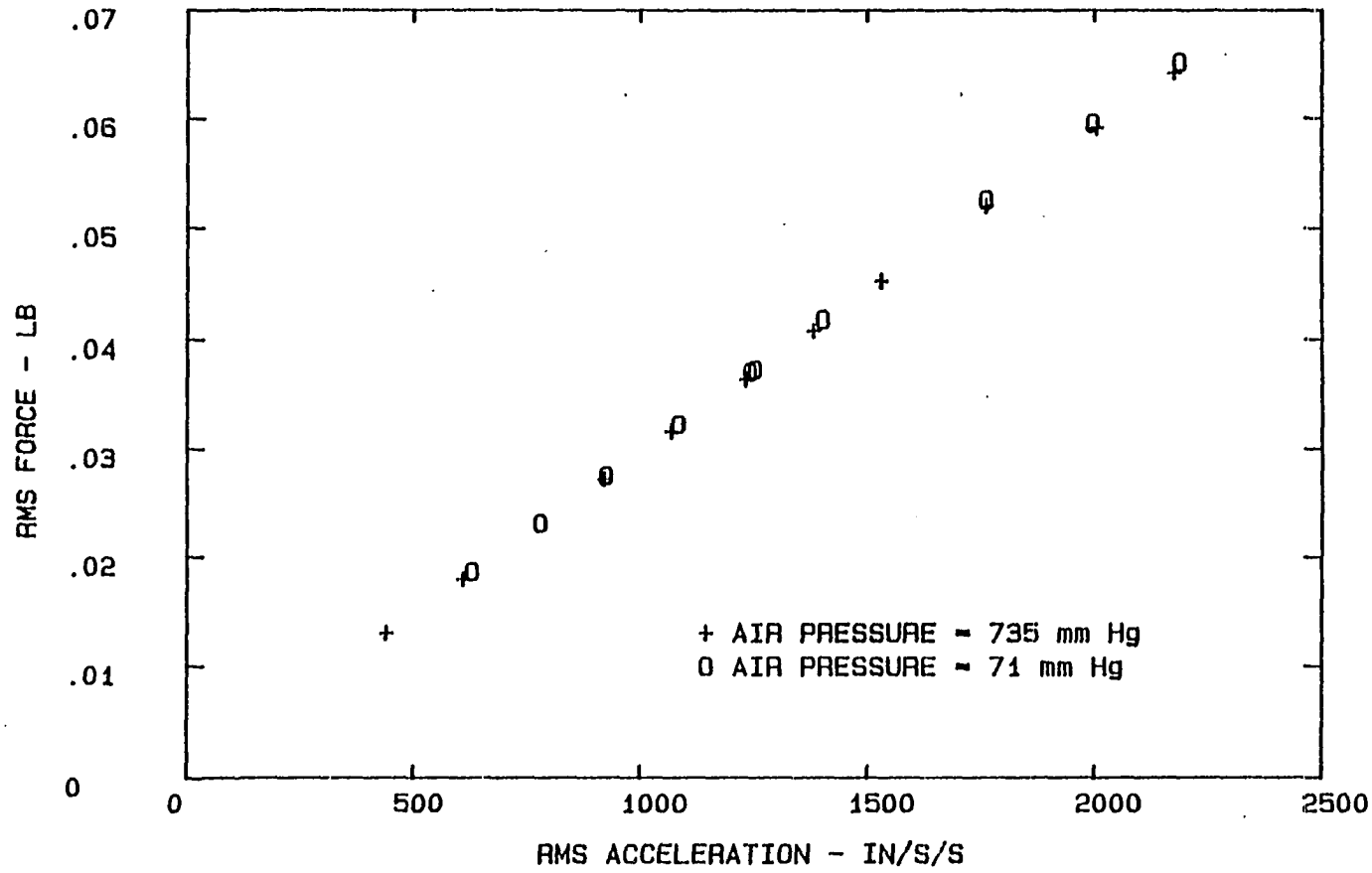

Fig. B-37. Force vs acceleration amplitude, mode 3, Model-Tech, first frequency component

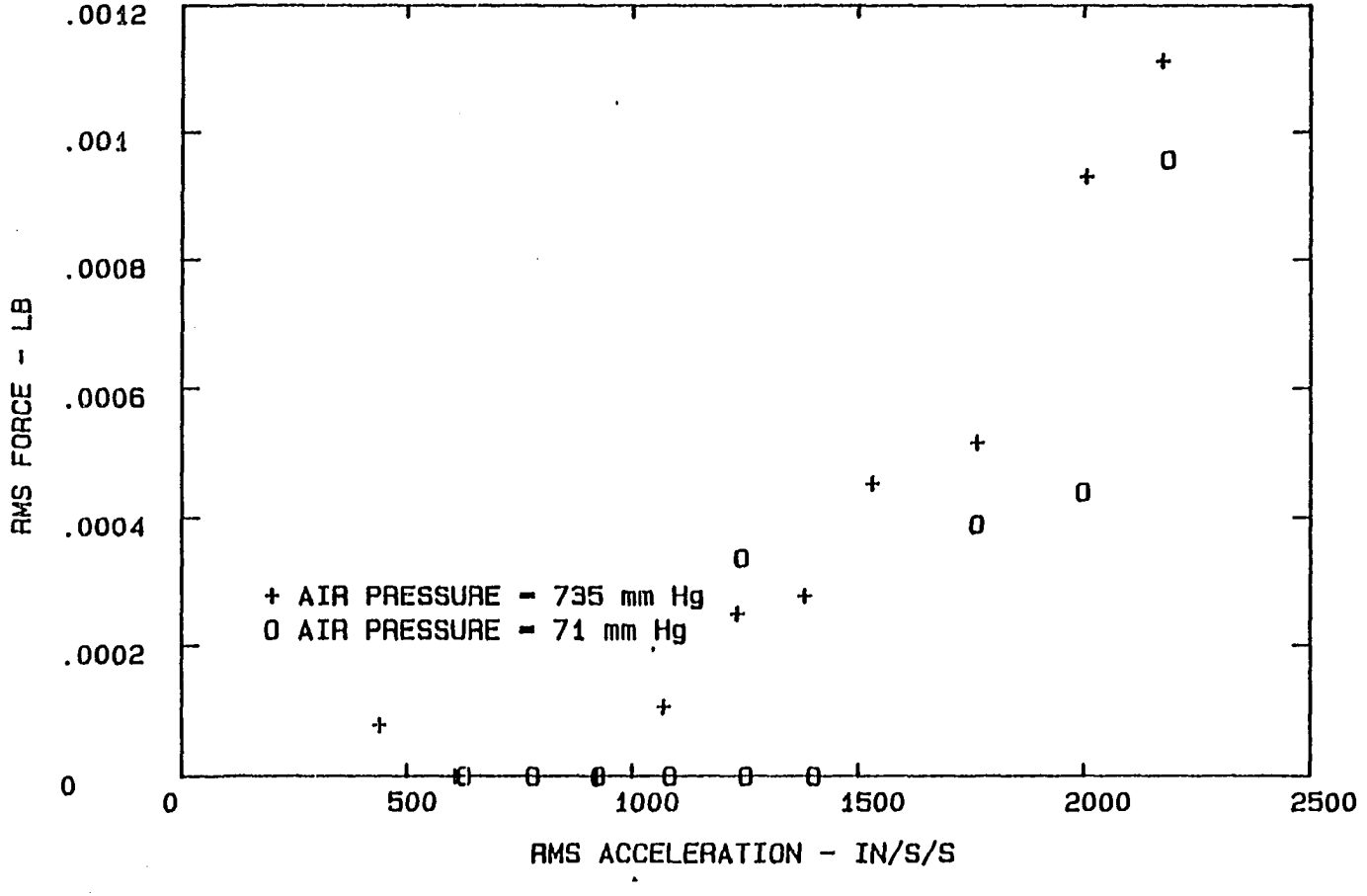

Fig. B-38. Force vs acceleration amplitude, mode 3, Model-Tech, second frequency component

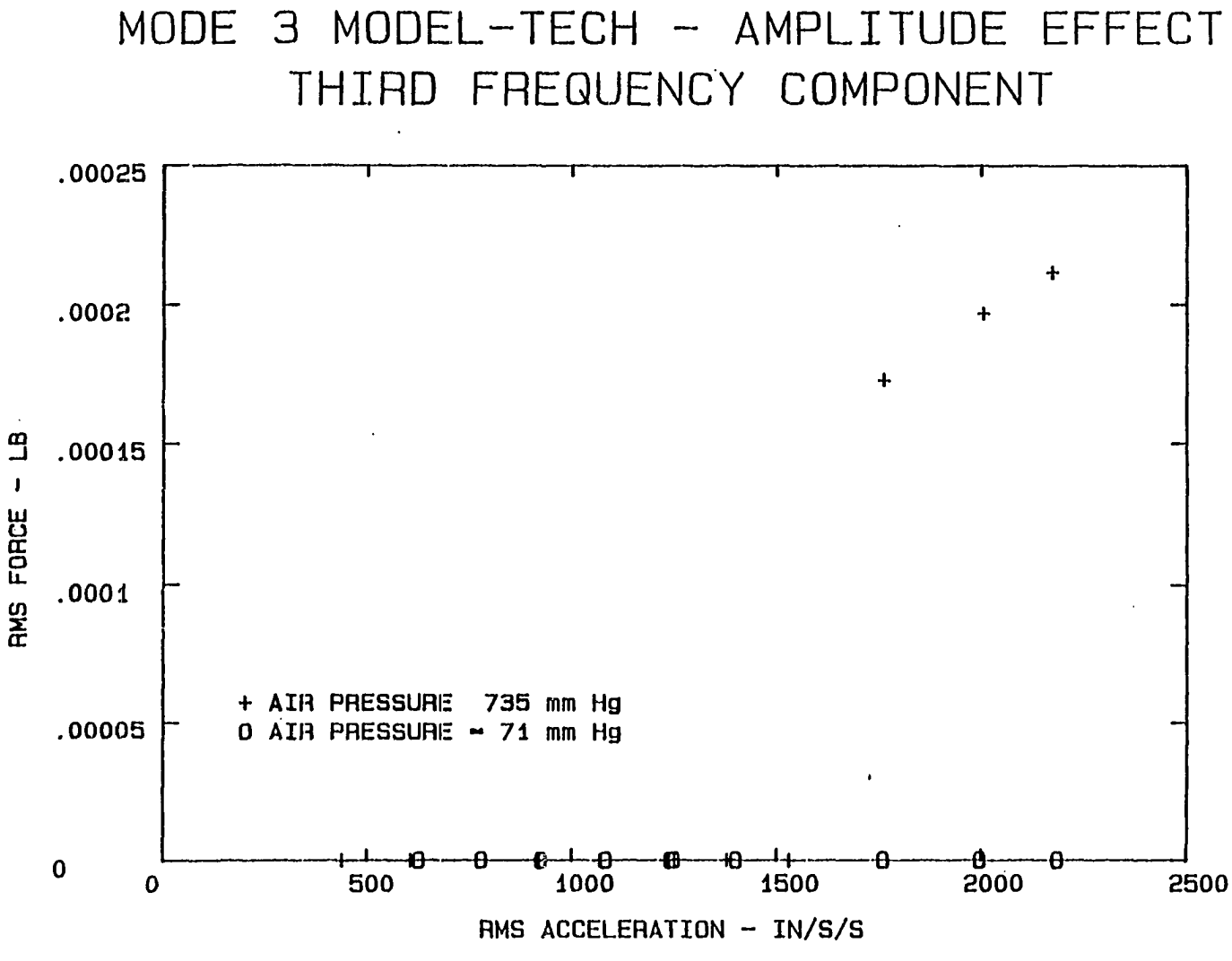

Fig. B-39. Force vs acceleration amplitude, mode 3, Model-Tech, third frequency component

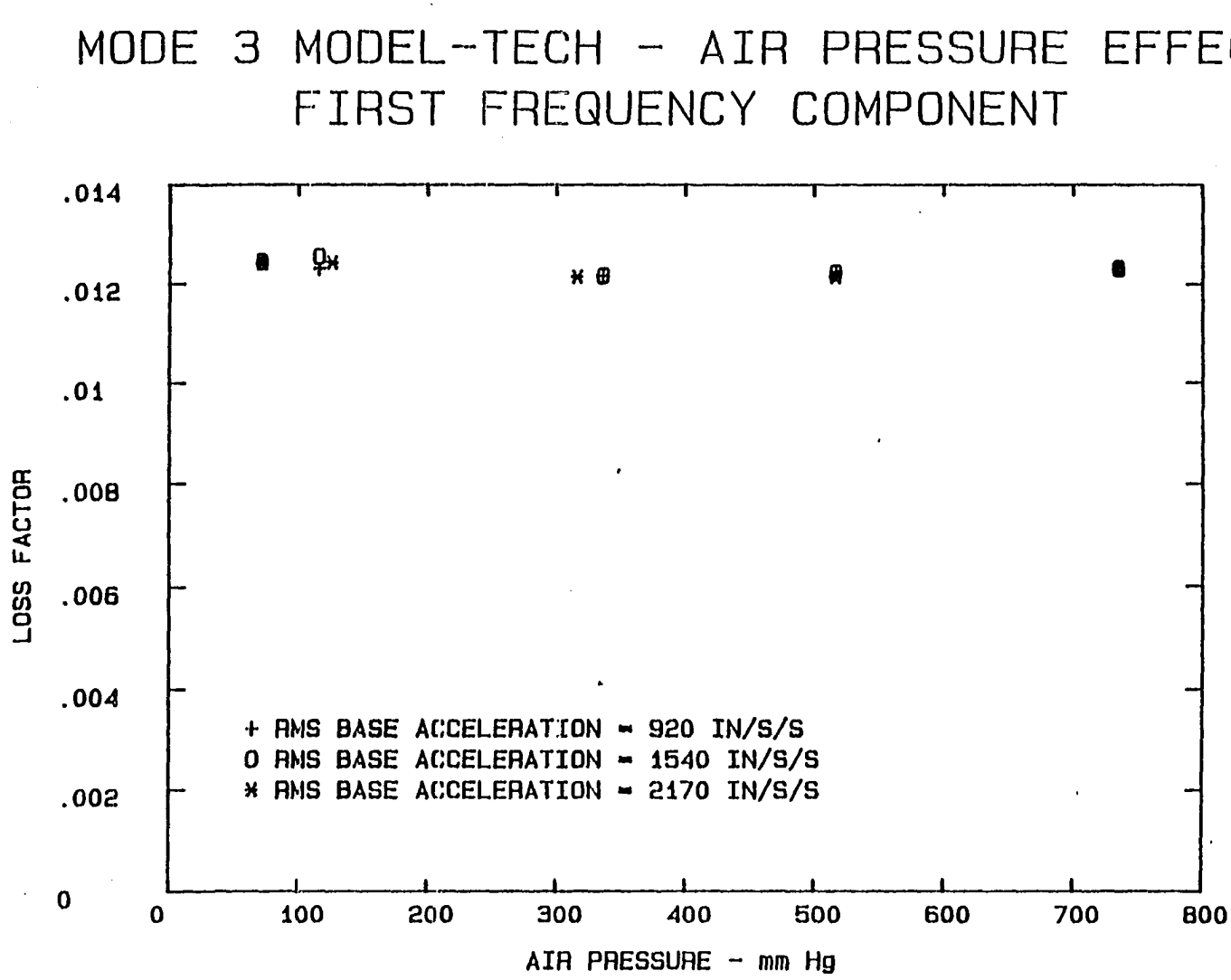

Fig. B-40. Loss factor vs air pressure, mode 3, Model-Tech, first frequency component

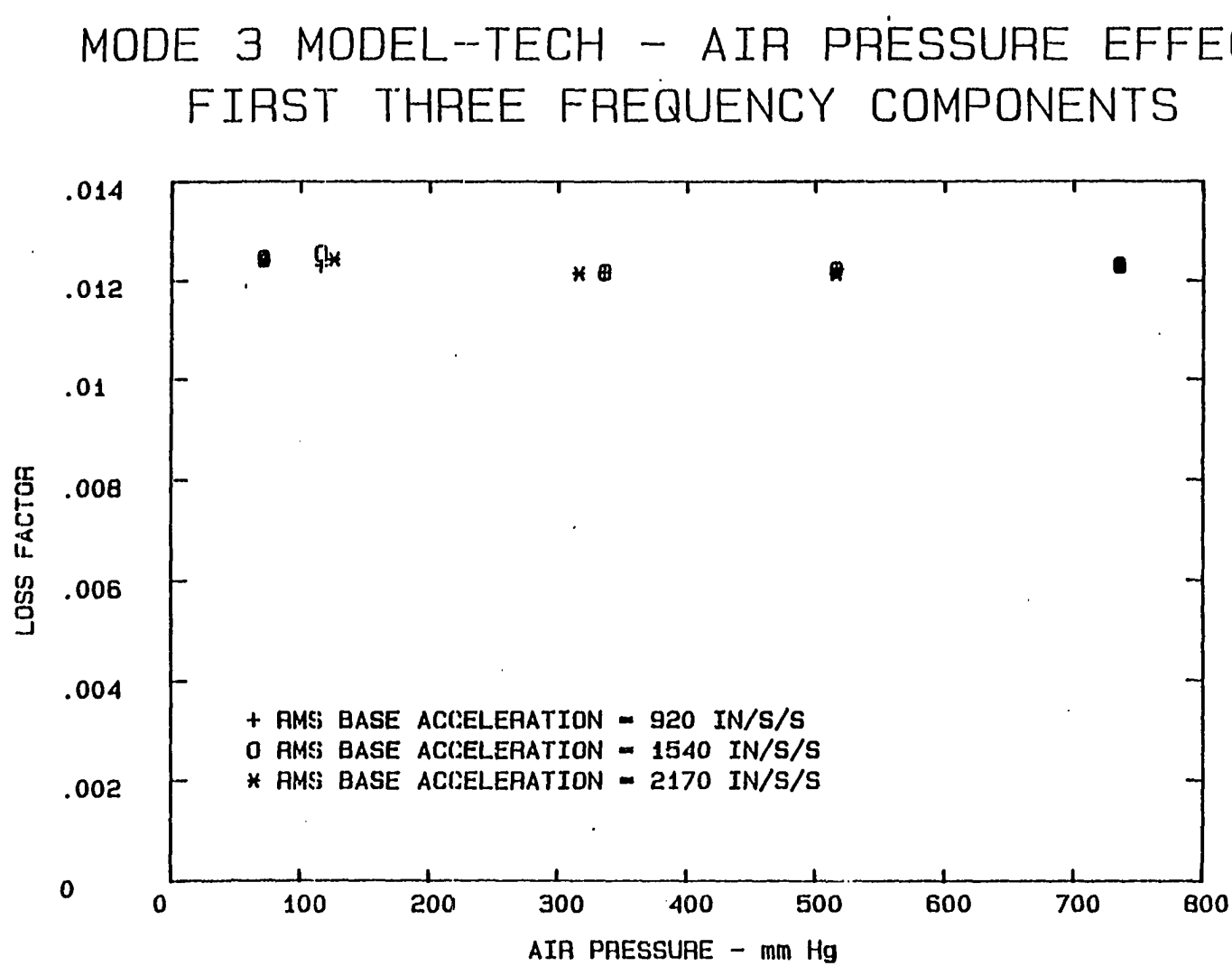

Fig. B-41. Loss factor vs air pressure, mode 3, Model-Tech, first three frequency components